INAUGURAL-DISSERTATION

ZUR

ERLANGUNG DER DOKTORWÜRDE

DER

NATURWISSENSCHAFTLICH-MATHEMATISCHEN
GESAMTFAKULTÄT

DER

RUPRECHT-KARLS-UNIVERSITÄT
HEIDELBERG

VORGELEGT VON
Dipl. Phys. Carola Ruth Richter
AUS HEIDELBERG

Tag der mündlichen Prüfung: 18. Oktober 2000

Entwicklung von Mikrostruktur-Gasdetektoren für Hochraten-Experimente

Gutachter: Priv. Doz. Dr. Bernhard Schmidt

        Prof. Dr. Johanna Stachel

Dissertation
submitted to the
Combined Faculties for the Natural Sciences and for Mathematics
of the Rupertus Carola University of
Heidelberg, Germany
for the degree of Doctor of Natural Sciences

Development of
Micro Pattern Gas Detectors
for High Rate Experiments

presented by
Diplom-Physicist Carola Richter
born in Heidelberg, Germany

Heidelberg, 18th of October 2000

Entwicklung von Mikrostruktur Gasdetektoren für Hochratenexperimente

Mikrostruktur-Gasdetektoren (MPGD), wie etwa die Gas-Mikrostreifen-Kammer (MSGC), bieten eine exzellente räumliche Auflösung und verfügen über gute Hochrateneigenschaften. Ein Langzeitbetrieb in einem Hadronenstrahl ist für MSGCs jedoch aufgrund von induzierten Überschlägen, die die feine Elektrodenstruktur innerhalb kurzer Zeit zerstören, nur begrenzt möglich. Erst durch eine Kombination mit einem *Gas-Electron-Multiplier (GEM)* als Vorverstärker ist ein sicherer Betrieb möglich. Die Gesamt-Gasverstärkung wird dabei in zwei räumlich getrennte – und damit ungefährlichere Schritte – aufgeteilt (Kapitel 5).

Im ersten Teil dieser Arbeit werden die Prinzipien des *Elektronen Transfers* im GEM-Detektor in Abhängigkeit einer Vielzahl von Parametern geschildert (Kapitel 2 und 3). Nach einer kurzen Einführung in die technischen Anforderungen des Hera-B Experimentes (Kapitel 4) werden im zweiten Teil die Untersuchungen zum Betriebsverhalten einer GEM-MSGC Kombination vorgestellt. Besonders die benötigte Strahlenhärte der Detektoren stellt hierbei hohe Anforderungen. Im Vordergrund der Messungen standen Untersuchungen, wie *Entladungen* zwischen Anoden und Kathoden oder GEM-induzierte propagierende Entladungen zu vermeiden sind (Kapitel 5). Ferner wurden verschiedene *Alterungsprozesse* (i. e. Gas- und Diamantalterung) studiert, um Schäden während eines Langzeitbetriebes auf ein Minimum reduzieren zu können (Kapitel 6). Im abschließenden Kapitel 7 werden die Ergebnisse des finalen Strahltests präsentiert, in dem die Hera-B Detektoren unter "realistischen" Bedingungen erfolgreich getestet wurden.

Development of Micro Pattern Gas Detectors for High Rate Experiments

Since the introduction of the *Micro Strip Gaseous Chambers (MSGC)* in the early 90s, a large family of different *Micro Pattern Gaseous Detectors (MPGD)* has grown, offering a high rate capability and an excellent position accuracy. However, a long-term operation of MSGCs in the critical conditions of hadronic beams is excluded due to induced discharges, inevitably leading to severe destructions of the fragile electrode structure. By using a *Gas Electron Multiplier (GEM)* as a preamplifying structure, the amplification can be divided into two separate stages, thus putting the MSGC operation back into a regime of safe operation (chapter 5).

In the first part of this thesis, the principles of the *electron transfer* in the GEM was studied as a function of a multitude of parameters (chapter 2 and 3). In the second part, following a survey of the technical requirements of the Hera-B experiment (chapter 4), the reliability of a GEM-MSGC combination during operation in a high rate hadronic beam was studied. In the focus of our interest was the investigation, how to avoid *discharges* between anodes and cathodes as well as GEM-induced propagating discharges (chapter 5). In addition, different kinds of *ageing processes* (i. e. gas ageing and diamond ageing), strongly influencing the gas amplification, were studied in order to allow for a stable long-term operation in a high rate beam (chapter 6). In the last chapter (chapter 7), results from the final beam test are presented, where the performance of the Hera-B detectors in "real" operation conditions was studied.

Contents

Chapter 1

Introduction

The operation of all gas detectors relies on the principle, that gas molecules in the active detector volume are being ionized by incoming particles. However, for the detection of the released charge, a wide variety of techniques are being used.

The *Geiger-Müller Counter*, first described in 1928 [1], can be considered the basis of gas detectors. The detection of the released charge relies on the process of avalanche electron multiplication induced by high electric fields next to a thin anode wire. A different concept is represented by the Ionization Chamber, another very early device. It consists of a parallel plate capacitor filled with dielectric gas or liquid. The released charge is drifted towards the electrodes and the resulting displacement current of the moving charge (electrons and ions) provides the detection signal.

For particle tracking in the early days of high energy physics, the *Bubble Chamber* was developed in the 1950s. For the following experiments, other types of detection instruments like the *Streamer* or the *Spark Chamber* were developed and later refined. These detectors in similarity to the Geiger-Müller Counter are operating at the high end of the gas multiplication process, near or even at the breakdown limit.

A different mode is the *proportional* gas amplification, in which the avalanche size is proportional to the primary charge. This type of detector is represented by the *Multi Wire Chamber (MWPC)* [2, 3], consisting of a plane of parallel anode wires between parallel cathode planes. It provides good spatial resolution and rate capability for particle tracking. The current signals, induced by the electron avalanches, are detected at the anodes or segmented cathodes by conventional charge amplifiers. Some of the useful offsprings of this technology are *Drift* and *Time Projection Chambers*.

The concept of micro-pattern structures used for electron multiplication is the most recent important step forward in the field of tracking detectors [4]. It was conceived in order to obtain a further improved detector granularity and possibility to achieve very high gains and excellent high rate stability at the same time. The Micro Strip Gas Chamber (MSGC) [5] was the first of this fast growing family of Micro Pattern Gas Detectors (MPGD). Like the MWPC-principle, these detectors operate in the proportional mode. Etched metallic electrode patterns, such as strips, grooves or dots — sometimes arranged in 3 dimensions — are used instead of thin wires. These patterns are constructed on an insulating or semiconducting substrate, mostly by photolithographic techniques. Due to a reduced gap-width between anodes and cathodes and a fast ion collection in high electric fields, MPGDs allow for a very fast signal formation.

1.1 Physics of gas detectors[1]

1.1.1 The signal formation

Incoming particles (such as charged particles or X-rays) release electrons by gas ionization, creating both ionized and excited gas molecules along their path. The energy for creating an electron-ion pair depends on the gas type, a typical value is 25–35 eV per electron-ion pair. The charges, produced in the ionizing process, quickly loose their energy due to collisions with the gas molecules. The total number of released electrons is strongly influenced by secondary effects, such as further ionization through primary electrons with a large kinetic energy or energy transfer of metastable states (*Penning effect*). The final number of released electrons, n_0, is proportional to the energy of the incoming particle. The so-called Fano factor, F, (having a typical value between 0.05 and 0.3) describes its fluctuation, σ_n:

$$\sigma_n^2 = F \cdot n_0 \tag{1.1}$$

To prevent the primary electrons from recombination, attachment to molecules having electron affinity or absorption in the walls, gases with a low probability of attachment have to be chosen, mainly noble gases or hydrogen. For detection of the released charge, an electric field is applied to drift the electrons towards the direction of the readout electrodes. The primary electrons are transferred through the drift gap, amplified in a high field region and detected by the readout. The details depend on the geometry of the specific detector, but of course the processes rely on the same physical principle for the drift and multiplication of charged particles in gases. Essential for all concepts is a high field sufficient for gas amplification. The field geometry in the vicinity of the anodes may vary from purely radial (MWPC) to parallel (parallel plate counter).

When the electron kinetic energy, acquired between two collisions with the gas molecules, is in the range of the first ionization potential of the gas molecule, the impact allows for creation of a new electron-ion pair. Both, the newly-released electron and the primary electron are further accelerated by the high electric fields and the process of ionization and multiplication continues along their path towards the anode, resulting in a large electron avalanche. In case of a radial field geometry, the first electron multiplication starts a few micron away from the anodes, where the field is in the order of ≈ 10 kV/cm. In parallel plate counters, the amplification takes place along the hole gap, the gain strongly depending on its length.

The *first Townsend coefficient*, α, is the relevant parameter for quantitative estimation of the number of electrons in the avalanche, for a given gas and field geometry. It is defined as the number of electron-ion pairs produced per unit length of drift. Its inverse is the mean free path for ionization, representing the average distance between two ionizing collisions. The electron number increase in a uniform field is given by:

$$n_{e^-}(x) = n_0 \, e^{\alpha x} \tag{1.2}$$

where n_{e^-} is the number of electrons after a distance x and n_0 is the number of primary electrons at $x = 0$. In a non-uniform field, as is the case in most gas detectors, it has to be modified to:

$$n_{e^-}(x) = n_0 \, e^{\int_0^x \alpha(x') \, dx'} \tag{1.3}$$

---

[1]This section is meant as a very brief survey only, an excellent and much more complete representation can be found in [6]

The total number of released electrons per primary electron after the total drift distance d is called the *detector gain* G, given by:

$$G = \mathrm{e}^{\int_0^d \alpha(x')\,dx'} = \frac{n_{e^-}}{n_0} \qquad (1.4)$$

Taking into account that α strongly depends on the field, the gain increases considerably at high fields. The majority of gas detectors are operated in this *proportional regime*, where the collected charge is proportional to the number of primary electrons.

The signal formation and development for e. g. a minimal ionizing particle (MIP) is as follows: For each primary ionization electron the number of electrons in the final avalanche follows a Polya distribution. Since the primary electrons arrive at the high field region at slightly different times, the signal of the MIP is given by a superposition of single clusters. The total charge created in the gas avalanche process by the incoming particle is collected at the read out electrode. As a result of signal propagation along the metal strip, the signal is often already smoothed when arriving at the first electronic amplification step. It is further smoothed due to the integration in the readout electronics. The final signal output following the electronic amplification step(s) is a convolution of the input signal and the response function of the specific amplifier(s). Due to large statistical fluctuations in the number of primary electrons, the spectrum of MIPs is typically Landau distributed, characterized by a wide and asymmetric shape.

1.1.2   Gas transport parameters for electrons and ions

The *electron diffusion* is an important parameter for all gas detectors, as the transverse diffusion (perpendicular to the drift field $\vec{E}_{\mathrm{drift}}$) strongly influences the detector resolution and the longitudinal one (parallel to the drift field $\vec{E}_{\mathrm{drift}}$) affects the time resolution and the signal length. As a function of the drift distance from the origin d, the diffusional width of the electron cloud σ increases according to

$$\sigma^2 = \frac{2\epsilon d}{|\vec{E}_{\mathrm{drift}}|} \qquad (1.5)$$

with ϵ being the mean thermal energy of the electrons.

The *drift velocity* $\vec{v}_{\mathrm{e}}$ of electrons in gases is relevant for the rise time of the signal. The motion of electrons in gases is given by the random thermal velocity v_{T} and by the electron drift induced by the external electric field $\vec{E}_{\mathrm{drift}}$:

$$\vec{v}_{\mathrm{e}} = \frac{e\vec{E}_{\mathrm{drift}}}{m_{\mathrm{e}}}\tau = \frac{e\vec{E}_{\mathrm{drift}}}{m_{\mathrm{e}}}\frac{\gamma}{v_{\mathrm{T}}} \quad \text{with} \quad v_{\mathrm{T}} = \sqrt{\frac{8kT}{\pi m_{\mathrm{e}}}} \qquad (1.6)$$

where τ is the average time between two collisions and γ the mean free path for the electron collision.

The same equations hold for the motion of ions. Due to their huge mass, the drift velocity is reduced by orders of magnitude. Also the diffusion plays a minor role for ions. Furthermore, in normal conditions ions cannot gain enough energy from the field to initiate gas multiplication.

However, the motion of ions plays an important role in the signal development. The signals are characterized by a fast rise time, induced by the arriving electrons, and a slower

rise, caused by the slowly back drifting ions. For all applications, where a fast signal is required, the parameters of the amplifier are chosen to differentiate the signal, thus using the electron component only. The effect of loosing a fraction of the signal is called the *ballistic deficit* in the total detector gain.

1.1.3   Limitations of gas detectors as tracking devices

The requirements for tracking devices in most high energy experiments are fast signal timing, a high detection efficiency and an excellent position accuracy. However, the performance of gas detectors is limited for principle reasons. Due to the low gas density, only about 100 electron-ion pairs are released per centimeter by a MIP in typical noble gas mixtures; however, a thin conversion gap, of only a few millimeters, is mandatory for fast signals. Therefore the primary statistics is dominating both, the detector efficiency and the position accuracy.

Some counting gases, such as iso-butane, dimethyl-ether (DME) or heavy freons, are known to improve the number of primary electrons, but they often imply inconveniently high operation voltages. They may be mixed with noble gases, such as Argon, which reduces the high voltage, but also the number of primary electrons. The choice of the right counting gas is always a very difficult task and the options for most detector types are clearly limited. One additional problem is that the phenomenon of *gas ageing* may lead to a decay of the gain during irradiation, thus excluding some of these gases for some applications. (More details concerning this issue are given in section 6.1.)

From simple statistical considerations it follows that the energy resolution R of gas detectors in general varies as $R \sim \sqrt{E}$. For a given number of primary electrons, the energy resolution is strongly influenced by the drift field. Very low fields provoke electron attachment, significantly reducing the energy resolution.

The strip multiplicity of a detector is defined as the average number of anode strips participating in the charge collection process per particle. This parameter depends on the type, the energy and angle of the incoming particle. Besides the ionization characteristics, it is strongly influenced by the diffusion parameters of the counting gas and of course by some geometrical parameters, e.g. the granularity of the detector. A common technique for increasing the intrinsic spatial resolution is by center-of-mass measurement of the charge density. Therefore, in most applications a strip multiplicity larger than "one" is strongly requested. However, in high rate beams the strip multiplicity has to be in the order of a few strips only, for keeping the detector occupancy (i.e. the fraction of channels being active simultaneously) sufficiently low.

1.2   A short survey of different gas detectors

The research efforts devoted to gas detectors are remarkable and a multitude of innovative devices have been developed over the last years. A short survey of some very interesting and original concepts is given in this introductory chapter. Since the main issues within the work presented here arose in the quest of a development of GEM-MSGCs for the inner tracking system of the Hera-B experiment, emphasis is put on the concepts of the MSGC and the GEM detector.

However, it will be shown, that the principles of gas detectors — and in particular those of the micro pattern detectors — are similar. The detectors have promising performances,

but in the hostile radiation conditions which prevail in the upcoming high energy physics experiments, the margin of safe operation is limited. The problem of discharging, as observed in the case of MSGC and GEM-MSGC combinations, reflects intrinsic problems of all micro pattern detectors. The physical concepts and a detailed experimental study on this important topic are presented in chapter 5.

1.2.1 Micro Strip Gas-Chamber

The Micro Strip Gas Chamber (MSGC) was introduced by A. Oed in 1988 [5] for detecting neutrons. The underlying principle has attracted a lot of interest during the last decade and — particularly in the field of particle physics — many more applications have been found. The expected rate capability as well as its position accuracy seemed to exactly meet the requirements of the new generation of high luminosity colliders. But although the original concept has been perfected in many points (e. g. with regard to a reliable longterm operation in a high rate X-ray beam), there are still problems left, clearly limiting their operation stability.

Geometry

The ionizing volume of a MSGC is defined by the glass substrate on the bottom side, a drift lit on top and frames with the gas inlets on the other four sides. The typical height is of the order
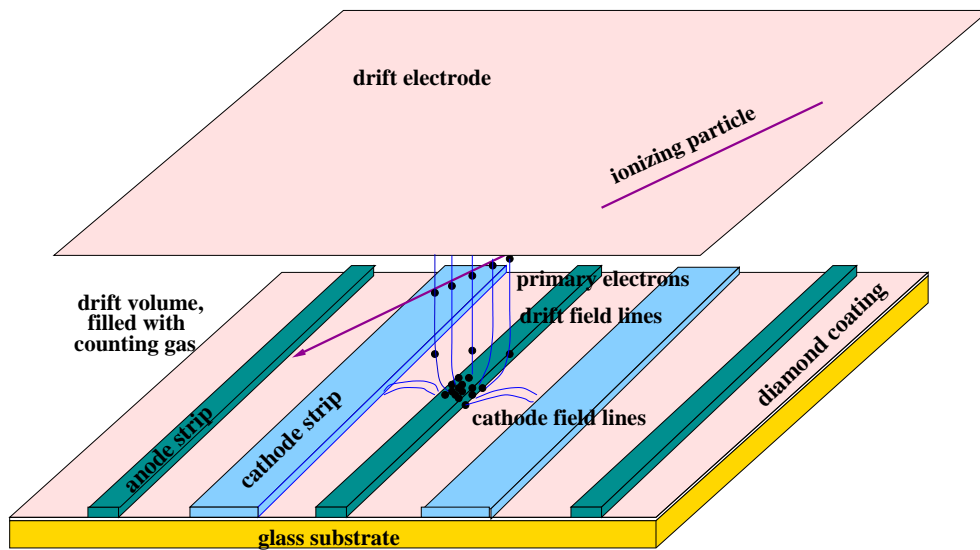

Figure 1.1: A schematic drawing of a MSGC. The insulating glass substrate (0.2–0.5 mm) is covered by a thin diamond layer with a defined resistivity of the order of $10^{15}\Omega/\square$. The microstructure, consisting of alternating anode (2–15 µm) and cathode strips (80–200 µm), is added by a lithographic technique. The drift electrode is on top, the detector height is typically a few millimeters.

of a few millimeters whereas the size of the active area can be as much as 30 cm × 30 cm, as e. g in the detector for the Hera-B experiment, the largest system ever built of MSGCs. The detector volume is usually filled with a mixture of a noble gas (argon, neon) and an organic quencher (such as CO_2, dimethyl-ether (DME) or i-butane). A homogeneous drift field of the

order of 2–10 kV/cm is required for drifting the released primary electrons towards the micro electrode structure. The required field strength depends on the requested readout time as well as on the gas type and on the detector geometry. The avalanche process is initiated in the vicinity of the anodes. The micro structure consists of thin alternating anode (2–15 μm) and cathode (80–200 μm) strips with a small gap in between. The electrode pitch is typically 200–300 μm.

Features

In high-rate experiments, such as Hera-B or the LHC-experiments, the detectors have to withstand particle rates of up to 10^5 Hz/mm^2, providing a stable gain of up to 10^4 at the same time.

By introducing an insulating glass substrate into the multiplication region, charging-up effects close to the anodes arose for high intensity irradiation rates. Thereby the electron amplification decreased, resulting in complete loss of signals after some time of irradiation [7, 8]. The detector performance was improved either by using a low resistivity glass or by adding an extra layer of low resistivity coating ("diamond coating", as depicted in figure 1.1) with a surface resistivity of typically $10^{15}\Omega/\square$. Measurements proved that gains of up to 10^4 can be reached without any operation instabilities during very long X-ray irradiation periods and for rates superior to 1 MHz/mm^2.

Not only charging-up effects, but also intrinsic discharge problems in hadronic beams entailed new concepts and developments. Those discharges between anodes and cathodes are known to destroy the fragile metal strips within hours and they prevent a reliable use of the MSGC concept in high rate hadronic beams. The way out was found with the introduction of the Gas-Electron-Multiplier (GEM) (see 1.2.5), which was coupled to the MSGC as a preamplification device for electrons. By splitting the electron multiplication of the detector in two spatially separated steps (GEM on the one hand and MSGC on the other hand), the discharge probability of combined detectors could be decreased by orders of magnitude, even in hadronic beams (see chapter 5 for the details).

1.2.2   The Micromegas

The MICROMEsh GASeous detector (micromegas) was introduced in 1996 by Y. Giomataris et al. (CEA/Sacley) in collaboration with G. Charpack (ESPCI/Paris) [9]. Different to the MSGC concept, it operates as a narrow-gap parallel counter.

Geometry

As depicted in figure 1.2, the basic component of the micromegas is a micro-mesh with a pitch of typically 50 μm, square holes of 40 × 40 μm^2 and a thickness of 3 μm). The metal grid is strained above a readout electrode at a small distance of 50–100 μm and stabilized by regularly spaced insulators (omitted in figure 1.2). The gas volume of the detector is separated into a conversion and an amplification region. A high optical transparency and a large field of $\approx$ 60 kV/cm in the amplification region allow for an efficient transfer of electrons through the mesh. Here, the entering electrons experience a very strong and — due to the broad anode strips — an almost uniform field, sufficient for gas amplification in parallel plate mode.
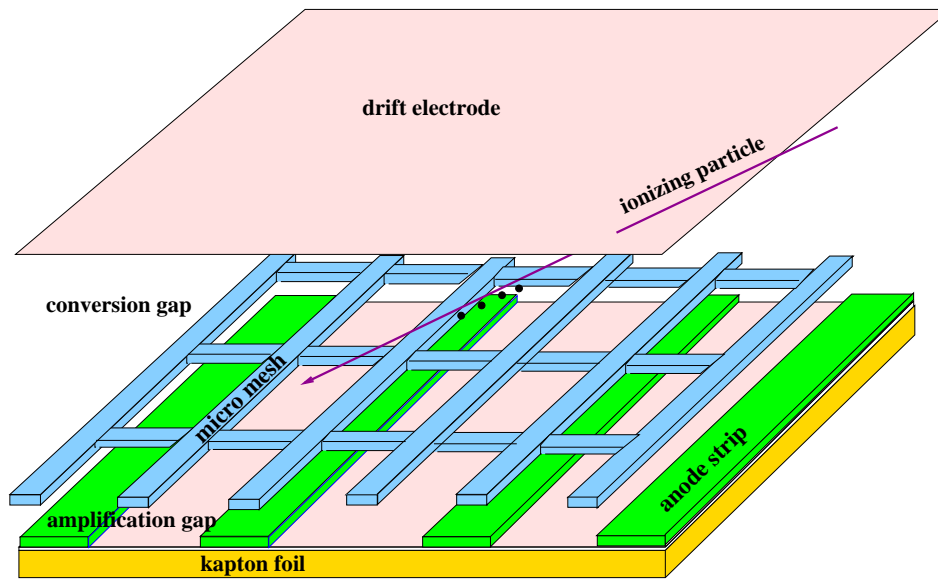
Figure 1.2: A schematic drawing of a MICROMEGAS detector. The primary electrons are transferred through a micro-mesh. The amplification starts in the lower gap of only $\approx 100~\mu m$ thickness. The anode strips are etched in a copper cladded kapton foil. The spacers for the mesh are not depicted here.

Features

The electron avalanche is collected on the readout structure (strips or pads), while most of the ions are collected on the mesh. Due to the small distances between the anodes (readout pattern) and the cathode (micro-mesh) and due to the high inductions field, the micromegas concept allows for fast signals in the order of only ≈ 100 ns. A good rate capability and energy resolution based on the principle of parallel plate amplification was demonstrated.

    In contrast to many other micro pattern detectors, the concept of MICROMEGAS is very robust with regard to destructions from discharges. But since the gas amplification is done in one step only and streamers tend to develop much easier in uniform fields, the discharge rate in hadronic beams is extremely high and still subject of intensive studies (as described in e. g. [10]). A good choice of the counting gases and a very robust electronics are mandatory in order to guarantee a long-term operation in high rate hadronic beams.

1.2.3   The Micro Wire Detector (μWD)

The Micro Wire Detector was introduced by B. Adeva et al. [11] in 1999. Similar to a GEM, this detector is produced by a wet etching technique.

Geometry

The thin anode strips (15–25 μm) are separated from the mesh-like cathode (with a pitch of typically 300 μm) by a gap of 50–125 μm of insulating Kapton [12], as shown in figure 1.3. On application of high voltage, an almost radial amplification field around the anodes is created for gas amplification.
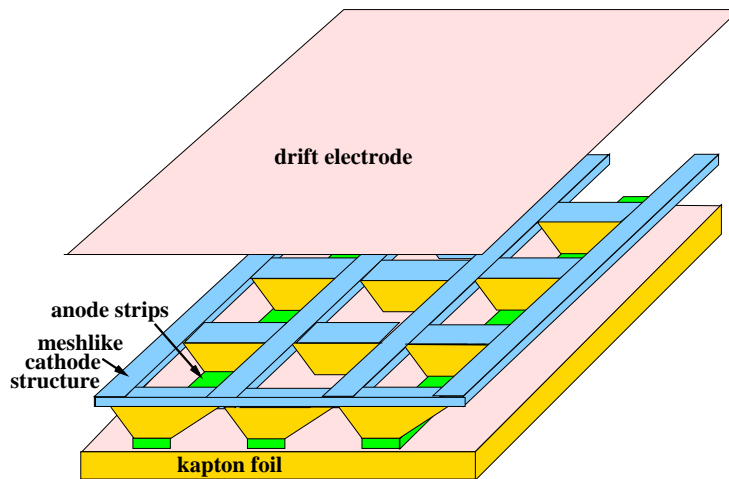
Figure 1.3: A schematic drawing of a Micro Wire Detector. The primary electrons are drifted towards a 3-dimensional microstructure at the bottom side of the detector. The mesh-like cathode and the thin anode strips of only 15–25 μm are manufactured by a wet etching technique.

Features

Similar to the conditions in a standard multi wire detector, the amplification takes place in a focused rather than a parallel field, thus combining a strong confinement of the avalanche to the strip vicinity with a high amplification factor. But in contrast to a simple wire chamber, the majority of the back-drifting ions are collected very quickly on the cathode, thus providing a fast full-charge integration (≈ 100 ns). Another advantage of the focused field is, that the large field gradient strongly supports the self-quenching of streamers. (This will be discussed in chapter 5.) Last but not least the amount of material is reduced to a minimum and thus the detector has a large radiation length.

1.2.4   The Micro Groove Detector

The Micro Groove Detector, introduced in 1998 by R. Bellazzini [13], can be considered another step forward: By using two arrays of micro-strips in different layers and with a different orientation, these detectors provide an excellent spatial resolution in 2 dimensions.

Geometry

As depicted in figure 1.4, the cathode layer on top of an insulating kapton layer is perforated by closely spaced micro-grooves with a pitch of a few hundred microns. When applying high voltage, a strong field sufficient for amplification is created inside the micro-grooves. The multiplied electrons are collected on the micro strip anode structure at the lower side. The signal can be detected on the anode and — due to induction — also on the adjacent cathode strips, thus providing a 2D positional information.

In concept very similar to the Micro-Groove Detector is the Well Detector (introduced by R. Bellazzini in 1999 [14]), also fabricated by printed circuit board techniques. Instead of micro-grooves, charge amplifying micro-wells are etched into the copper cladded kapton layer. The anode electrode is designed as an array of micro-strips.
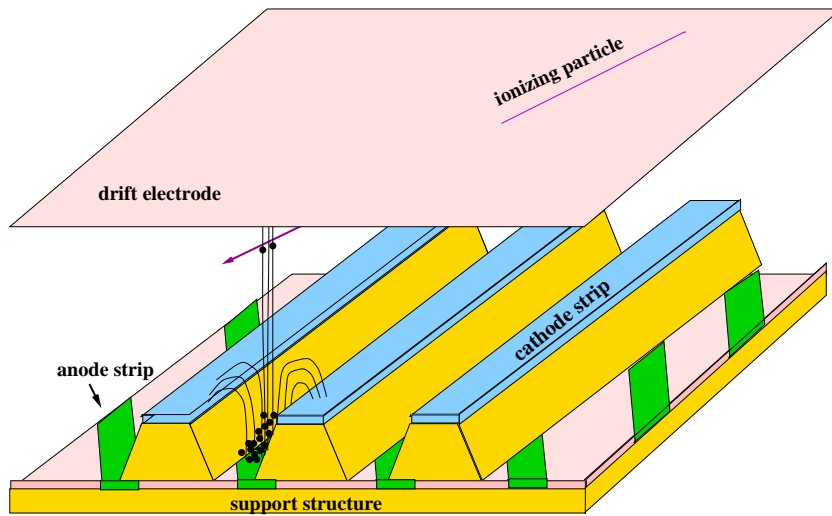
Figure 1.4: A schematic drawing of a Micro Groove Detector. The primary electrons are drifted towards a 3D microstructure at the bottom side of the detector. Application of a potential difference across anodes and cathodes creates a high electric field within the micro-grooves, allowing for gas amplification. The resulting signal is shared between anodes and cathodes, providing a 2D readout signal.

Features

As reported e. g. in [13], a gas gain of 15,000, a rate capability in the order of 10^6 Hz/mm^2 and an energy resolution of 22 % at 5.4 keV can be obtained with the Micro-Groove Detector. Furthermore, no significant charging-up or ageing effects up to 5 mC/cm were found and a full primary charge collection even at high fields can be guaranteed.

Nevertheless, a test in a hadronic beam has to prove, whether these detectors can operate in a high-rate hadronic beam without discharging. Due to an almost uniform field (similar to the conditions in the Micromegas Detector), a comparatively high discharge rate has to be expected. Similar to the MSGC, also here the introduction of a GEM as a preamplifying structure can significantly reduce the discharge probability. As reported for the Micro Groove Detector [15], very high maximal gains have been achieved ($\approx 3 \times 10^5$) and when exposed to heavily ionizing particles (which are known for inducing discharges) the detector was found to be spark free up to gains of 10^4. As it will be shown in chapter 5.4, a gap of sufficiently low fields between the two amplifying structures is mandatory for an operation free of sparks.

It was studied in the Heidelberg group, whether the concept of the Micro Groove Detector may serve as one possible option for the inner tracker of the LHCb experiment. As described in detail in [13], the detector was successfully manufactured using printed circuit technology. But due to technical limitations of the wet etching process, the angle for the grooves is fixed to values of approximately 45°, clearly limiting the variety of geometries and especially the height of the amplification region. It was investigated (see also [16]), if laser techniques can be applied for the manufacturing process of micro-grooves, hopefully allowing for any desired geometry. By means of simulations, a geometry providing a small inter-strip capacitance was developed. This point is very important in order to keep the detector induced noise level on a tolerable level. Another important boundary condition is a low charging-up tendency, mainly

dominated by the geometry of the insulating kapton layer. A summary of the simulation results of this pre-study can be found in [17].

1.2.5   The Gas-Electron-Multiplier

The Gas-Electron-Multiplier (GEM) was introduced by F. Sauli as a "gas preamplifier" for electrons in combination with MSGCs for the tracking of particles in high energy experiments [18, 19, 20] in 1997. Different from the other detectors, the GEM device does not allow for spatial particle resolution and thus it has to be operated in combination with a readout pattern or a second amplifying step.

After many improvements in the manufacturing process and the geometry [21],[22], detectors could be realized, where the GEM serves as the only amplification step. However, in order to provide higher gains, GEMs are often cascaded to multiple layer devices.
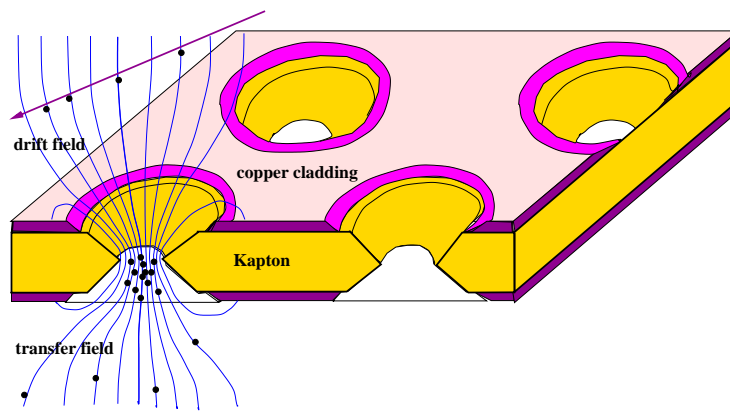

Figure 1.5: A schematic drawing of a Gas-Electron-Multiplier (GEM). A kapton foil, copper cladded on both sides, is perforated with an array of small holes. By applying a potential difference between the upper and lower side of the GEM, high electric fields — sufficient for gas amplification — are created in the apertures. The multiplied electrons are extracted from the lower exit and transferred towards a second amplification step.

A multitude of applications for GEMs have come up in many different fields in the last years:

- **cascaded GEMs**
  A double GEM combination [23] has been successfully tested and built for the compass experiment and a triple-GEM-combination [24] is forseen for the inner tracking system of the LHCB-experiment. It was proven recently [25] that these devices can be reliably operated in high rate hadronic beams with gains up to 10^5.

- **GEM-MPGD combinations**
  Due to their ability of separating the multiplication and the readout functions, GEMs have become a very common device as a preamplifying element in combination with Micro Pattern Gas Detectors of all kind.

- **other applications**
  GEMs are used as amplifying structures in time projection chambers (TPC) [26],[27] and, in view of non-high-energy-physics applications, multiple structures optimized for

large amplification factors are being developed for ultra-soft X-ray spectroscopy [28] and nanodosimetry [29], e.g. in detectors for single-electron counting.

Geometry

The GEM-foil consists of two thin copper layers separated by an insulating dielectric (mostly Kapton) with a high density of chemically pierced holes, as shown in figure 1.6. Typical values
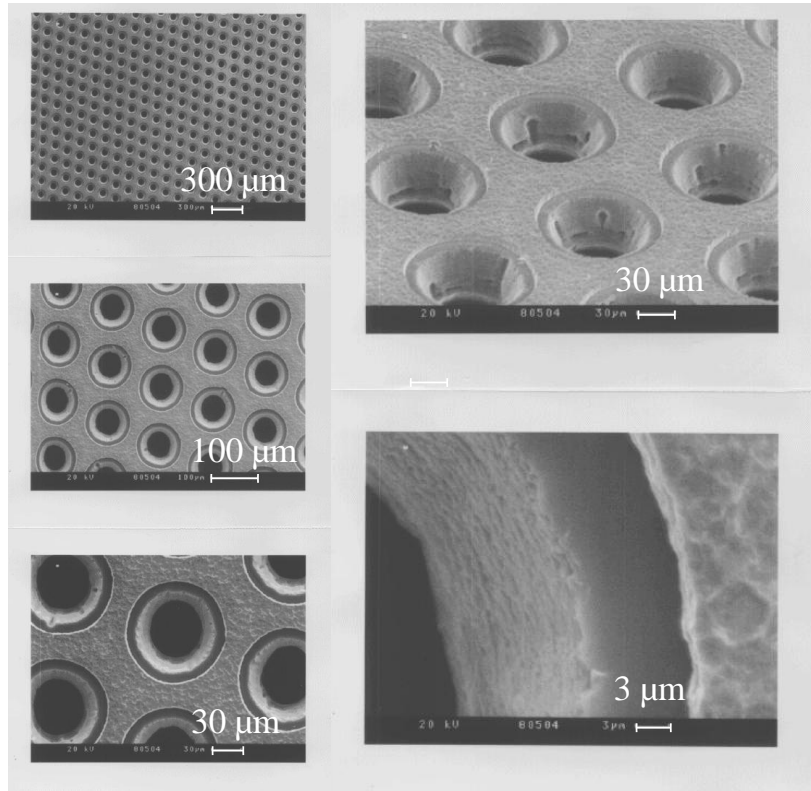

Figure 1.6: Microscope shots of a GEM-foil from a top (left side) and an oblique view (right side) [30]

for the thickness of the Kapton foil and the copper are 50 μm and 5 μm respectively. The hole diameter is usually chosen in a range between 40 μm to 140 μm, while the pitch varies between 90 μm and 200 μm. The so-called "standard GEM" is characterized by a diameter of 70 μm for the copper, respectively 55 μm for the kapton hole. The pitch between to adjacent holes is 140 μm.

Manufacturing

The readout device for multi-GEM combinations can be manufactured using a reasonably cheap and robust standard printed circuit technology. The most common technique for manufacturing the GEM itself is a wet etching process [31]:
 In the first step, the pattern of holes is engraved on the metal by conventional photolithography of both sides. Next, the GEM holes are etched, using the pattern itself as mask. Due
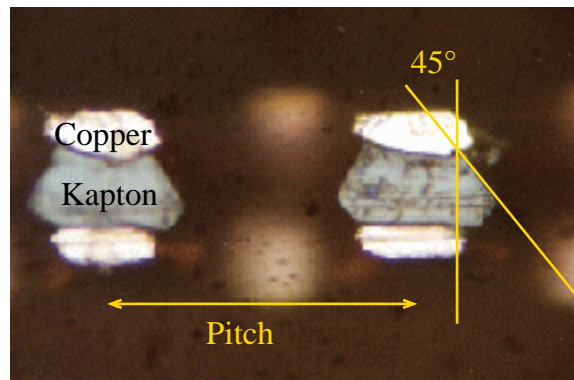
Figure 1.7: Cut through a GEM. In the side view the different layers (kapton and copper) are clearly visible. The sidewalls have an angle of about 45°; the copper layer is 15 micron thick, the double etching technique was not applied here.

to this technique of etching, the kapton aperture is extremely close to the edge of the copper hole. In case of a non-perfect etching process, metal tips may loom in the GEM aperture, thus significantly reducing the high voltage stability between both electrodes. In order to overcome this problem, the GEM-foil is etched another time ("double copper etching"). This process increases the diameter of the copper aperture, thus reducing the discharge probability in the GEM. As a side effect, the copper layer thickness is reduced from originally 15 micron down to about 7 micron.

The isotropic behavior of the etching process results in a double-conical shape of the aperture and sloping side-walls with an angle of about 45° (see figure 1.7). As a result, incoming electrons as well as back-drifting ions tend to hit the exposed insulator edge in the GEM aperture, resulting in field distortions and operation instabilities. First attempts to produce GEMs with laser techniques were successfully done [32]. Apart from higher gains, this technique provides two other advantages: (i) a larger thickness of the insulator between the electrodes would reduce the GEM capacitance, being very helpful in case of GEM discharges (details see section 5.4) and (ii) cylindrical (instead of double-conical) holes can significantly reduce charging-up effects in the insulating layer.

Multiplication process

In order to operate a GEM as a multiplying element (see also 1.5), a voltage of a few hundred volts (depending on gas type and pressure) is applied between the upper and the lower side of the GEM-foil, creating a strong dipole field. The incoming primary electrons are guided into the aperture and — if the field in the GEM aperture is sufficiently high — accelerated to energies above the ionization potential of the specific gas, thus initiating the avalanching process. The electron cloud develops in the hole until it reaches the point where the field drops below the multiplication threshold, usually a few micron behind the exit of the GEM channel.

External electrodes are required in order to generate a drift and a transfer field for the transport of the primary and amplifyied electrons (before and after GEM multiplication).

According to equation 1.4 for the electron amplification in gas detectors, there are different parameters for tuning the gas amplification factor in a GEM:

- **Applied Voltages**
  The electrical fields in the holes are given by a superposition of (i) the applied GEM-voltages between the upper and the lower side of the GEM and (ii) the drift field, the field lines of which mainly grip through the holes and continue in the transfer region. The drift fields, however, only minimally affect the multiplication process in the GEM channel.

- **Hole Geometry and Pitch**
  The electric field in the GEM channels is strongly influenced by the hole geometry. For a given GEM-voltage and inter-hole distance, small holes provide higher gains. However, it should be noted that small holes significantly reduce the fraction of primary electrons being able to enter the GEM aperture (see also "electron transfer efficiency of a GEM" in chapter 2.3). Depending on the specific application ("high gain" or "high single electron detection efficiency"), the GEM geometry must be optimized appropriately.

- **Thickness of the GEM-Foil**
  Another approach to increase the GEM-gain is to increase the path, where gas amplification can take place. Increasing the thickness of GEMs would therefore result in larger gains. The standard GEM has a thickness of 50 micron for the insulating Kapton layer. As long as GEMs are produced of Kapton with conventional wet etching techniques, the thickness is limited, due to the fact, that the holes cannot be etched vertically. This may be different, as soon as large scale GEMs can be manufactured by laser techniques in a good quality [32].

Features

The particular properties of these preamplifiers are gains up to several 10^3 and an effective ion-feedback reduction, as most of the ions hit the lower side of the GEMs instead of being transferred through the aperture. The signal response is very fast, since the comparatively slow ion back-drift is shielded by the GEM foil itself.

Furthermore, GEMs are mechanically very robust and the production techniques are comparatively cheap. Large detector can be realized (e. g. for Hera-B with an active size of 30 cm × 30 cm), helping to reduce expenses and readout channels.

However, the GEM device cannot be compared to other MPGDs, as it always needs an additional readout structure to provide a spatial resolution for particle tracking. As a consequence, the primary electrons not only have to be multiplied in the GEM, but they also have to be transferred through the GEM apertures and — after the multiplication — towards the readout structure without losing the initial signal. A good understanding of the physical process is required for an optimization of the promising features of GEMs. This issue will be the main topic of chapter 2.

Although GEMs are rather robust devices, it cannot be excluded, that GEMs are damaged as a consequence of discharges between the two electrodes. During the development and the beam operation of the Hera-B GEM-MSGCs, several detectors were lost due to electric shorts. Different from damages in the MSGC, where only a few channels are affected, the whole detector cannot be operated any more.

Apart from the minor problem of charging-up effects (see also chapter 7) it has to be noted that the standard GEM-foils cannot be properly operated when using the often favored DME as one component of the counting gas. Large amounts of DME where found to diffuse into the kapton material, causing a loss of mechanical tension and gain homogeneity of the GEM [33]. This problem is relevant for all detectors, in which a large kapton surface can interact with the counting gas.

Part I

Efficiency of the Gas Electron Multiplier

Chapter 2

The Electron Transfer[1]

2.1 Introduction

In this chapter, the results of an extended study of the electron transfer through Gas Electron
Multipliers (GEM) are given. In applications where a relatively large number of primary electrons are deposited within the gas volume preceding the GEM, e.g. resulting from charged
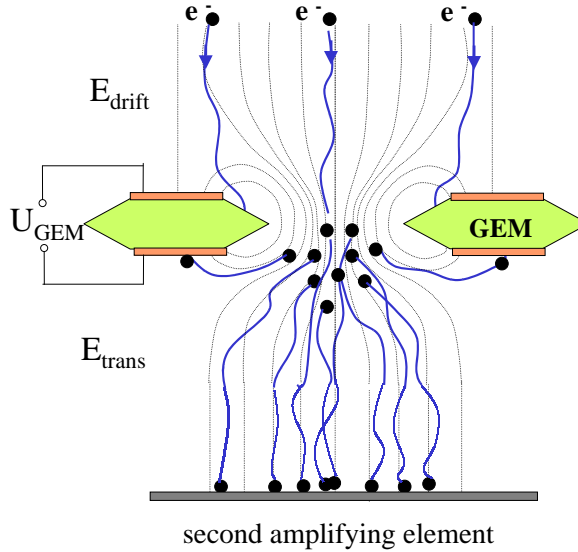particles or X-rays, the transfer efficiency would affect mainly the pulse-height resolution. In

*Figure 2.1: An illustration of the multiplication process in a GEM, showing the drift region
preceeding the GEM-aperture and the transfer region for the transfer of multiplied electrons
towards a readout structure or a second amplifying element.*

contrast, in detectors sensitive to single or a few electrons, e.g. detectors based on photoemission or secondary-electron emission from a solid converter [36] or on gas-deposited single
electron counting techniques [37], poor transfer and a loss of one electron would result in a
serious deterioration of the detected parameters and often in a complete loss of the event.

---

[1]Main parts of this and the next chapter are extracted from our published paper [34, 35]

This is the case in gas avalanche imaging photomultipliers for UV and visible light [38], based on a photocathode coupled to GEM. The GEM, or a cascade of GEMs [39], could be a multiplier of choice, even when operating in noble gas mixtures [40], due to its natural screening of avalanche-induced secondary photons. However, it is essential to ensure full detection efficiency for events originating from single electrons.

Conditions will be presented in this chapter, where a single or a few electrons deposited within the sensitive detector volume can be efficiently collected and multiplied within the GEM apertures and further extracted to a consecutive multiplier or readout element. The *transfer efficiency*, which is the efficiency at which an electron can be focused into one of the GEM apertures, rather than being trapped by the metal entrance electrode, depends on three issues: on the geometry of the GEM apertures (diameter, spacing), on the electric field configuration within and on both sides of the GEM element and on the process of electron transport within the gas volume preceding the GEM. The last, of which the most important parameter here is the transverse electron diffusion, is a function of the gas type and pressure and of the electric field strength across the drift volume.

It has been demonstrated that good transfer conditions were obtained while keeping low electric drift fields at the entrance of the GEM and high fields at its exit [41]. This operation condition should be adequate for most applications in which charges are deposited and collected in gas.

Establishing experimentally the transfer efficiency of single electrons through GEM apertures in an absolute way is a very difficult task. So far, only relative measurements of charge transfer were made, by recording X-ray-induced currents on the GEM and its surrounding electrodes [41]. Such measurements do not permit for a direct measurement of the transfer efficiency, but rather of the product of the efficiency and the GEM gain. Counting pulses resulting from the GEM multiplication of single electrons has the potential of providing absolute transfer efficiency. However, measurements carried out in a pulse counting mode, with single electrons photo-produced on a photocathode preceding the GEM [54, 43], provided so far only relative data, due to the lack of a reliable counting rate normalization.

When proper normalization of the event counting rate is provided, the single electron counting technique can establish the absolute single electron transfer efficiency of the GEM. The method consists in measuring the ratio between the number of GEM-multiplied pulses and that of the originally deposited single electrons within the gas volume preceding the GEM. The results of such systematic studies, made in various gases, in the pressure range of 1 mbar to 1 bar are presented in this study. The measurements, accompanied by Monte Carlo simulations, were made as function of the electric fields within the GEM and at the gas gap on its both sides.

In this chapter only the case of *single* primary electrons deposited in the gap preceding the GEM is treated. It is important to distinguish between measurements based on recording currents (current mode) and measurements based on recording pulses (pulse mode). In the latter, the information of both, the pulse height and the pulse counting rates, can be extracted.

2.2   Simulations on the electron transport

Before presenting quantitative experimental results, an overview of the general principle of electron transport through the GEM is given using monte-carlo simulations. In these calculations, fundamentally basing on the previous work of G. Garty [44], a 3D-model was created

by the MAXWELL 3D field simulator [45]. The intrinsic symmetry of GEMs in x- and y-
direction was used to simplify the structure and thus a 3-dimensional elementary cell, as
shown in figure 2.2, served as a model for the simulations. For large area calculations the
GEM-foil was continued in x- and y-direction by selecting symmetric mirror boundaries. The
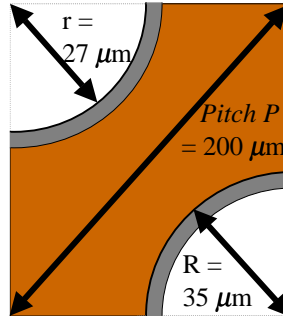

*Figure 2.2: Elementary cell for GEM simulation, symmetric boundary conditions in x- and
y-direction.*

electric field conditions above the GEM in the so-called *drift region* and also below the GEM
in the *transfer region* (c. f. figure 2.1) were taken into account. In the model, a distance of 1
mm was chosen for both regions. This comparatively large distance corresponds to the actual
geometry of typical GEM applications.

Field geometry

In figure 2.3, a simulation of the field conditions inside the GEM-aperture is given for two
different values of the field below the GEM, the transfer field E_{trans}, clearly reflecting the
dipole-field conditions.

Electron drift

Since the electron diffusion depends on the characteristics of the gas and its pressure, a
specific gas type had to be selected for electron-drift simulations. In the examples described
here, i-butane at 50 mbar was chosen, representing one of the conditions of the experimental
part of this study.

Depending on the variation of the field E_{drift}, three different characters of electron drift
can be distinguished. For a very low field, the diffusion is extremely large and the position
information of the electron is significantly reduced. In addition, a large number of electrons
do not succeed in reaching the GEM due to electron-ion recombination. For an intermediate
drift field, the electrons are drifted to the closest GEM aperture, thus keeping the position
information, and the transfer efficiency through the aperture is satisfactory. For very high
fields, the electron transfer efficiency is poor due to unfavorable field conditions (for details
c. f. section 2.5).

In figure 2.4, the simulation of the drift and transfer of 25 electrons (arranged in an array
of 5 × 5 equally spaced points) through a GEM hole is depicted. For drift conditions with a
very high diffusion (equivalent to very low fields) a large fraction of electrons diffuse towards
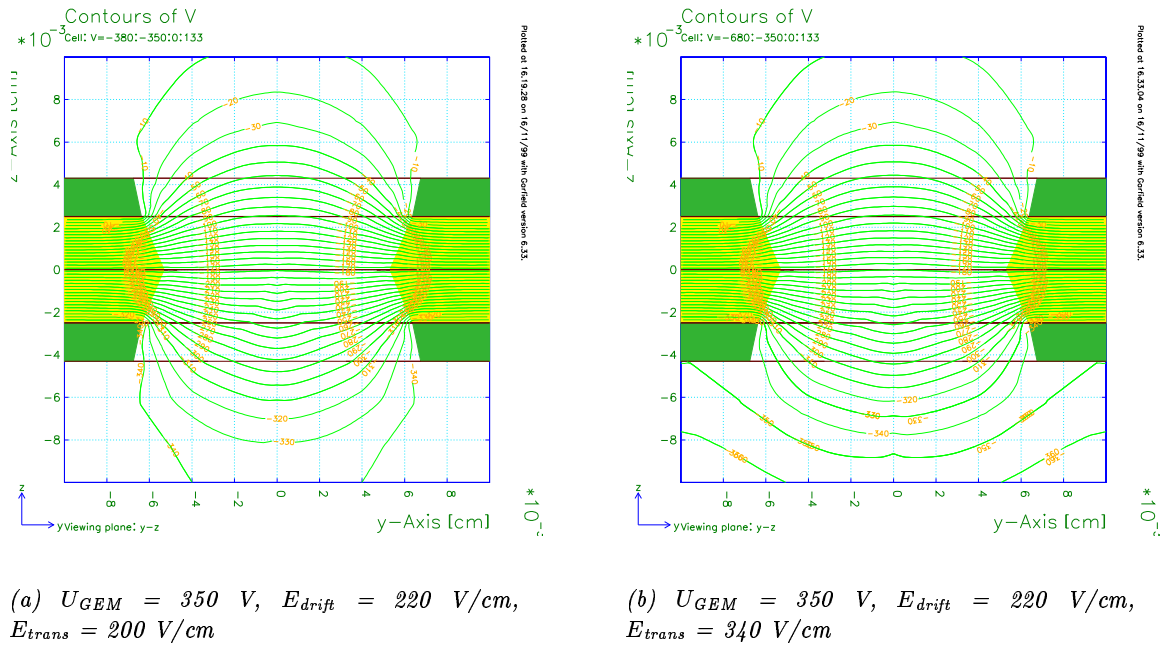the neighboring cells, as depicted in figure 2.4.a. For increased E_{drift} and thus a reduced

(a) U_{GEM} = 350 V, E_{drift} = 220 V/cm, E_{trans} = 200 V/cm

(b) U_{GEM} = 350 V, E_{drift} = 220 V/cm, E_{trans} = 340 V/cm

Figure 2.3: Simulation of equipotential-lines inside a GEM-hole

(a) Very low field with large electron diffusion. A fraction of the electrons diffuse towards neighboring GEM cells.

(b) Small electron diffusion. Electrons mostly drift towards the nearest GEM holes.
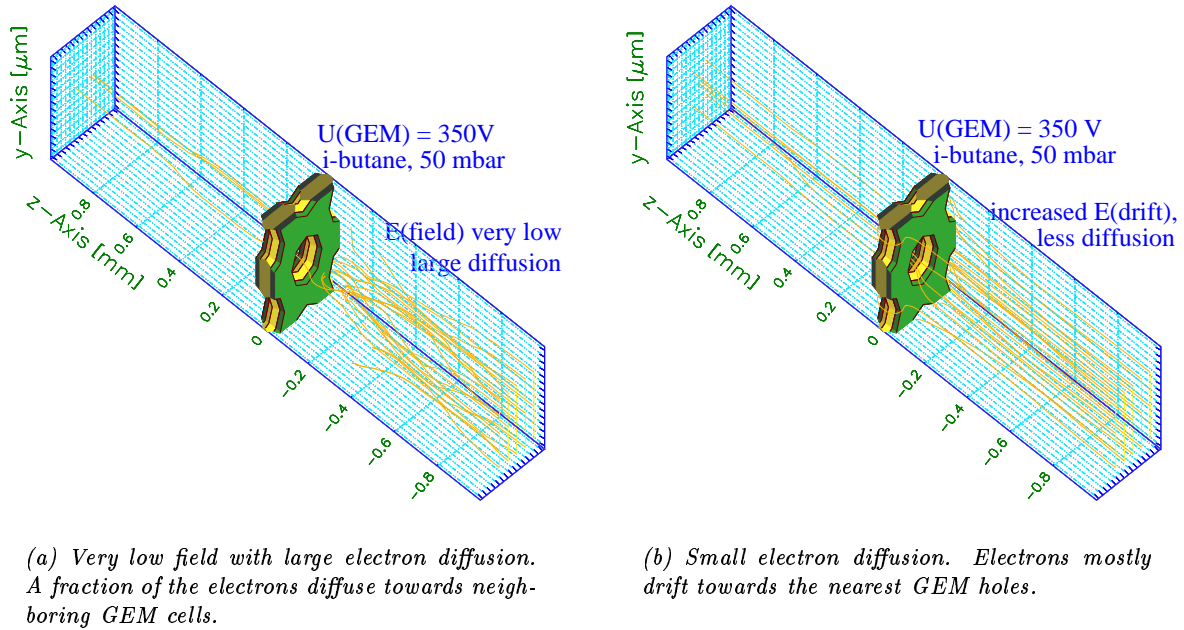
Figure 2.4: Simulation of the electron drift (including diffusion) towards and through the GEM-apertures in different field conditions. (Starting grid: 5 × 5 array of electrons.)

electron diffusion (figure 2.4.b), most electrons drift towards the nearest GEM hole. After being transferred through the GEM channels, they continue drifting towards the read-out structure.

(a) Very low field E_{drift} with poor electron trans-fer.

(b) Low field E_{drift} with improved electron trans-fer.
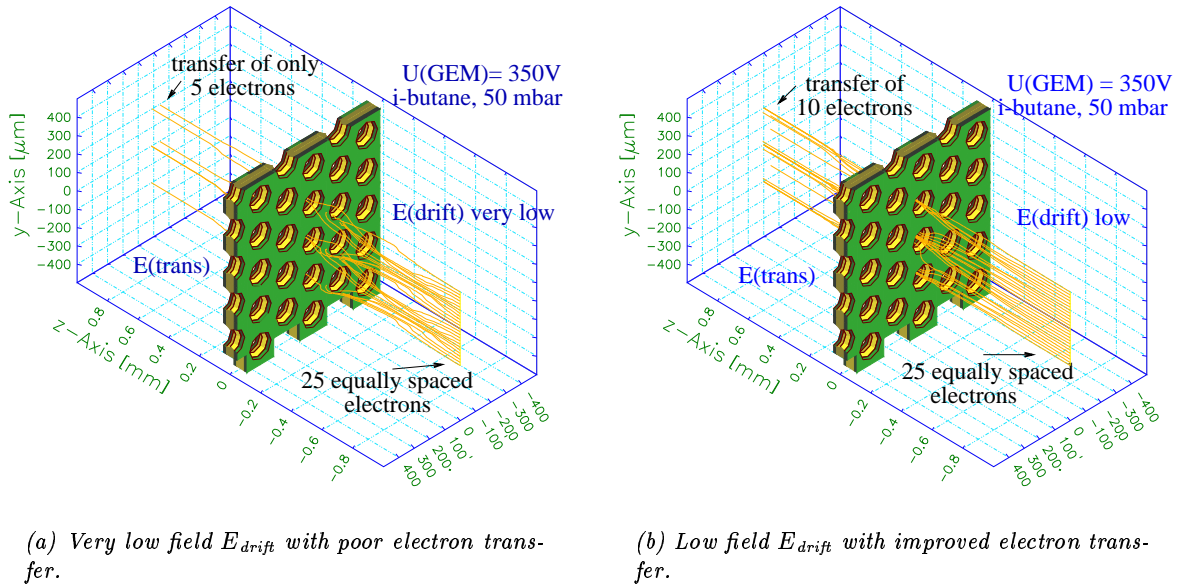
Figure 2.5: Simulation of the electron drift with diffusion, 25 electrons equally spaced on one line on top of a larger GEM array. (View from the upper side.)

In figure 2.5, the drift of 25 electrons, equally spaced on one line, is shown for an enlarged area of the GEM-detector, visualizing the full drift path of the electrons. It has to be emphasized here, that the multiplication process in the GEM was not taken into account here for these simulations.

Quantitative simulations

In parallel to the measurements in the lab, more extensive Monte Carlo simulations with the specific geometry of the "standard GEM" were performed at CERN [46], providing quantitative results. A similar 3D-model of the GEM was designed with the simulation package MAXWELL [45], as described in detail in [47]. The transparency has been computed by randomly generating an electron in the drift volume, at a given distance above the GEM; its path is followed as it drifts and diffuses down the GEM channel, using the Monte Carlo version of gaseous electron transport (MAGBOLTZ [48]) in GARFIELD [49]. For a reliable determination of the transfer efficiency of the primary electron it was taken into account that (i) some of the electrons may be lost (e. g. on the top or lower surface of the GEM) and that (ii) electrons experience ionizing collisions, when they encounter the high field in the holes. This results in an avalanche of electrons, whose size mainly depend on the dipole field within the GEM holes. The process is repeated several times (500), in order to estimate the transparency of the GEM for single electrons with a good statistics. The outcome of the simulations is presented in section 2.5 and also in chapter 3, where these results are compared to the experimental results.

2.3   On the efficient electron transfer

The gas amplification mechanism can be divided into three consecutive steps, as shown in figure 2.1: (i) the *collection* of electrons from the drift volume preceding the GEM, under an electric field E_{drift}, and their *transfer* and focusing into the GEM apertures; (ii) the *multiplication* of electrons within the high electric field created by the potential U_{GEM} across the GEM apertures; and (iii) the *extraction* of the multiplied electron swarm from the GEM exit face, under an electric field E_{trans} into a consecutive gas avalanche multiplier of any type, to create a detectable signal at the read-out circuit.
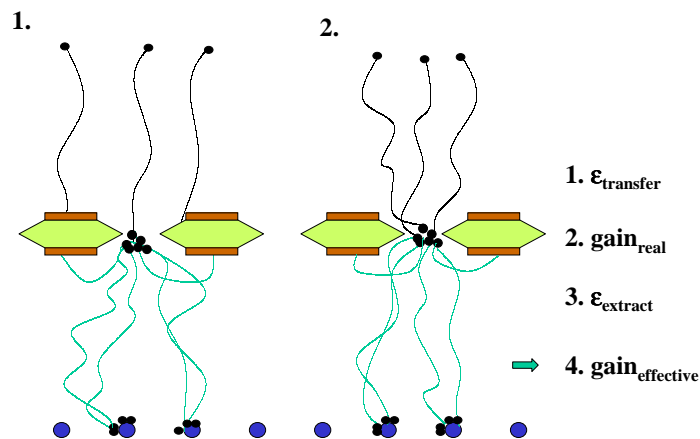
Figure 2.6: Illustration of the "gain" of a GEM. In both examples, the effective gain is "4/3". However, in example (1.), the real gain is "6" and the transfer efficiency is "1/3", whereas in example (2.) it is "1" with a real gain of only "2". In all single electron applications, 2 out of 3 events cannot be detected in example (1.).

To specify the process, we define the following variables (c. f. figure 2.6):

- The *real GEM gain* G_{real} is the average number of multiplied electrons in the GEM per number of entering electrons.

- The electron *transfer efficiency* $\varepsilon_{\text{trans}}$ is the fraction of electrons deposited in the gap above the GEM which are entering into the GEM holes and experience multiplication.

- The electron *extraction efficiency* $\varepsilon_{\text{extract}}$ is the fraction of GEM-multiplied electrons that are extracted from the GEM to the subsequent element.

  Both efficiencies depend on the electron diffusion and — for a given field condition — are functions of the gas type and pressure.

- The *effective GEM gain* G_{eff} in current mode is the ratio between the current arriving on the readout electrode or the second amplifying element below the GEM (figure 2.1) and the current injected into the gap above the GEM. It is the product of the real GEM gain G_{real} and the transfer and extraction efficiencies:

  $$G_{\text{eff}} = \varepsilon_{\text{trans}} \cdot G_{\text{real}} \cdot \varepsilon_{\text{extract}} \tag{2.1}$$

In current mode, the real GEM gain, G_{real}, is not directly measurable, because it appears as the product of three parameters (equation 2.1). If all current is collected on the exit GEM face (by reversing the direction of the field E_{trans}), the equation for the effective gain reads

$$G_{\text{eff}} = G_{\text{real}} \cdot \varepsilon_{\text{trans}},$$

since the extraction efficiency is not relevant then.

The extraction efficiency, $\varepsilon_{\text{extract}}$, is measurable in current mode, from the ratio of the current arriving at the readout electrode to the current collected on the exit GEM face, with a reversed direction of the field E_{trans}.

However, the *absolute* value of the transfer efficiency, $\varepsilon_{\text{trans}}$, cannot be separated from the real gain, G_{real}, in a simple current measurement, since all currents are a superposition of the negative electron current and the positive current of the backdrifting ions.

2.4   The experimental concept

In our new method of pulse counting, i. e. recording the absolute *rate* of single-electron pulses and not only the pulse-height and/or the detector currents, the electron transfer efficiency is directly derived from the ratio between the rate of counted pulses after GEM multiplication to the rate of deposited single electrons above the GEM.

2.4.1   The experimental set-up

Figure 2.7 presents schematically the method for measuring the absolute GEM transfer efficiency, as defined above. This method is based on a precise evaluation of the counting rate of single-electron events, counted with a MWPC.

The experimental set-up consists of two different electron multipliers, which by lateral displacement can be coupled to the same semi-transparent CsI photocathode. The latter was illuminated through a Quartz window by a continuous-illumination UV-light source, emitting single photoelectrons into the gas.

A MWPC detector (figure 2.7, right) is used for normalization of the photoelectron counting rate, namely for counting the rate of pulses induced by single electrons arriving at the drift gap (between identical meshes M_1 and M_2). The second, the GEM-MWPC detector (figure 2.7, left), is used for counting the rate of pulses induced by single electrons arriving at the *same* drift gap (between the mesh M_1 and the GEM) and being further transferred into the GEM.

It is assumed, that any electron transferred into the GEM aperture will initiate an avalanche, of which a fraction of the electrons is extracted and further multiplied by the MWPC. This entails that the signal will not get lost once the electron has reached a GEM-hole. Hence, the ratio between these two counting rates provides the *absolute transfer efficiency of the GEM.*

It is important to note that neither full efficiency for detecting every single electron released from the photocathode nor the knowledge of the absolute value of this efficiency are required, because the losses due to recombination or at the mesh M_1 are identical in both detectors and do not appear in their ratio. Only for the MWPC of the normalization detector, a detection efficiency for electrons reaching the mesh M_2 of roughly 100 % is fundamental for a reliable measurement. This could be guaranteed for high gas amplification in the MWPC [56].
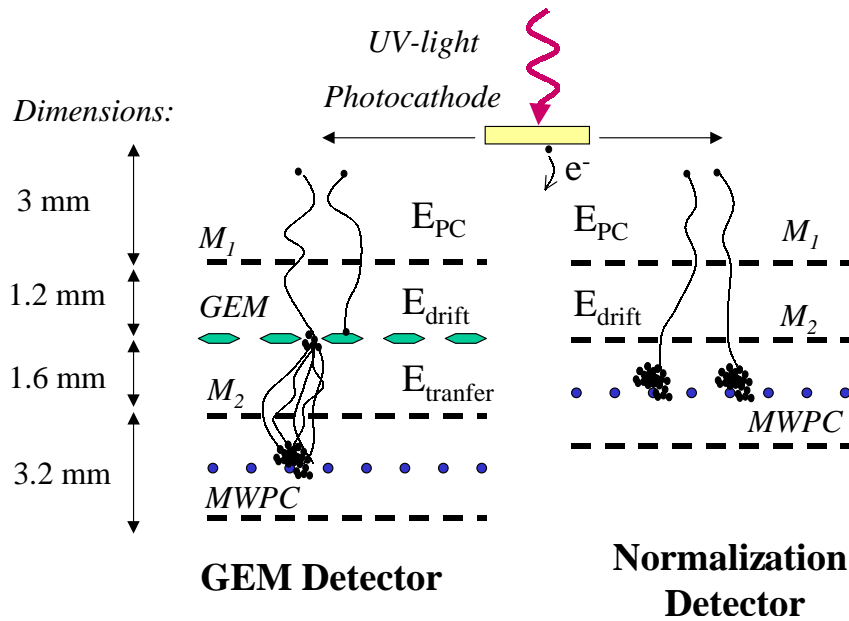
Figure 2.7: A schematic view of the experimental set-up. By lateral movement, the two different detectors are coupled to the same photocathode and UV-lamp. The meshes M_1 and M_2 allow for applying identical fields in the corresponding regions of the two detectors.

In the experimental arrangement, the GEM gain can be varied over a large range, provided that the total GEM-MWPC detector's gain is maintained constant and sufficiently high for efficient detection of single electrons, even with a low GEM gain. Particular care is taken to properly choose the electric fields at the photocathode gap, and in the drift gaps preceding the MWPC and the GEM, in order not to affect the transfer efficiency measurements. This will be discussed below.

For all measurements, a 30 mm by 30 mm CERN-made GEM was used, with a hexagonal aperture array of 140 micron pitch and 55/70 (inner/outer) micron hole diameter, in a 50 micron thick copper-cladded Kapton. The mesh electrodes above the GEM and the MWPC as well as the MWPC cathodes are made of 50 micron in diameter crossed stainless steel wires, 500-micron apart (81% optical transparency). The MWPC anodes are made of 10 micron in diameter wires, 1 mm apart.

The two detectors and the photocathode are placed within a vacuum vessel connected to a turbo-molecular pump. The vessel is evacuated to 10^{-5} mbar prior to gas filling. The system is operated in a gas flow mode, using mass-flow meters, differential pumping and a regulated pressure control. The detectors are displaced within the vessel with a vacuum-compatible linear manipulator.

For the measurements, we chose three different gas-mixtures. For the low pressure measurements (1–50 mbar), i-butane was the gas of choice due to its excellent quenching properties. For high pressure measurements (0.5–1 bar), the operation voltages are found to be inconveniently high and thus two other "common" counting gases were chosen: Ar/CO_2 (70:30), which will be used for the GEM application in the Hera-B experiment, and Ar/CH_4 (95:5), which is a very promising counting gas for GEM applications in the field of "gas avalanche photomultipliers" [39].

2.4.2 Detailed methods of measurements

For each set of measurements (gas, pressure), several variables have to be studied prior to recording the pulse counting rate: electron extraction from the photocathode, electron transfer efficiency through the meshes M_1 and M_2, amplification curves of the GEM and single-electron pulse-height spectra of the MWPC and of the GEM-MWPC detectors.

Electron extraction from the photocathode

The electron extraction from the photocathode was studied in "current mode" for each gas and pressure, namely by recording the photocurrent on mesh M_1 as function of the applied electric field, E_{PC}. This is shown in figure 2.8 for i-butane at 50 mbar and 200 mbar. The photocurrent evolution strongly depends on the gas type, but in general, after a steep increase at very low fields, it saturates (e. g. in i-butane for $E_{PC}/p > 7.5$ V/cm mbar). It was assumed that by applying identical E_{PC} values to both detectors, the number of electrons entering both of them is identical for a given photocathode illumination rate. In order to reduce systematic errors caused by small deviations in the applied fields preferably E_{PC} values in the "slanted plateau" were chosen. The *absolute* photoelectron rate is *not* relevant for the determination of the absolute GEM transfer efficiency.
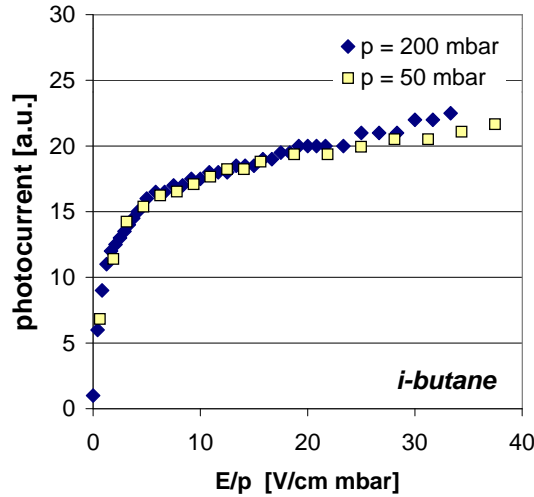
Figure 2.8: Extraction efficiency of photoelectrons from the photocathode. The photocurrent was measured on M_1, with a reversed E_{drift}, as function of E_{PC}, in i-butane at 50 mbar and 200 mbar.

Origin of the photoelectrons

A crucial point in our method is the origin of the photoelectrons. For a correct normalization of the counting rate it has to be ensured that all counted pulses in both detectors originate from electrons created at the semi-transparent CsI photocathode and not, for example, at the GEM-copper plane, which is also illuminated by the incident UV light. Copper-emitted photoelectrons would falsely enhance the counting rate of the GEM-MWPC detector. This

point was checked by reversing the field E_{PC} (but not E_{drift}, c. f. figure 2.7) and thus excluding the drift of any electrons from the photocathode towards the GEM-MWPC detector. A reduction of the counting rate by two orders of magnitude for identical illumination conditions was found. Thus the maximum systematic error due to photoemission from the GEM face is in the order of 1%.

Electron transmission through the meshes

Once extracted from the photocathode, the electrons are transmitted into the drift region of each detector. The transmission efficiency (also called "mesh transparency") through the mesh M_1 (see figure 2.7) depends on the ratio of the electric fields E_{drift}/E_{PC}.

For sufficiently homogenious fields E_{drift} and E_{PC}, a mesh is transparent, if the following condition is fulfilled ("Frisch-Gitter" [50]):

$$\frac{E_{drift}}{E_{PC}} > \frac{1 + \frac{2\pi r}{d}}{1 - \frac{2\pi r}{d}} \tag{2.2}$$

with r being the wire radius and d the inter-wire distance. In our geometry, with r=25 μm and d=500 μm, this leads to the condition $E_{drift}/E_{PC} > 2$.
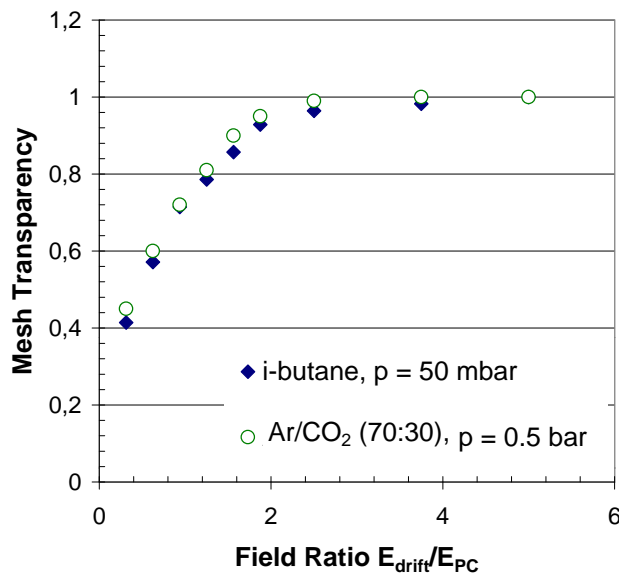
Figure 2.9: Transparency of the mesh M_1 in two gas-pressures. The photocurrent was measured on M_2, keeping E_{PC} constant ($E_{PC}/p = 3.75$ V/cm mbar in i-butane and $E_{PC}/p = 0.8$ V/cm mbar in Ar/CO_2) and varying E_{drift}.

The transparency was measured by recording the current of the transferred electrons as a function of the field ratio. In figure 2.9, the mesh transparency in i-butane (50 mbar) and Ar/CO_2 (0.5 bar) is plotted as function of the fields ratio, demonstrating a full transparency plateau for $E_{drift}/E_{PC} > 2$ in our mesh geometry, well confirming the theoretical value. The mesh transparency was found to be similar for all gas mixtures and pressures investigated here. Again, identical field conditions have to be chosen for *both* detectors, thus ensuring identical rates of primary electrons deposited in the drift gap above the MWPC and the GEM. Up to

this point, both detectors are absolutely identical, and by providing the same electric fields the electron rates are assumed to be equal. In order to reduce systematic errors caused by small voltage deviations, field ratios in the *transparency plateau* were chosen, whenever possible.

Normalization of the counting rate

For a 100% detection efficiency of the non-amplified single electrons and thus a correct normalization of the primary electron rate in the pulse counting method, a full transmission through the MWPC cathode mesh, M_2, in the normalization detector has to be guaranteed. Therefore, for each experimental condition one has to assure that $E_{MWPC}/E_{drift} > 2$, E_{MWPC} being the electric field below the MWPC cathode. However, this is not always possible to fulfill, for two reasons: (i) E_{drift} varies over a wide range for assessing the GEM transfer efficiency and (ii) E_{MWPC} is not decoupled from the MWPC gain. Such a situation, of low transmission through M_2, is reflected by a decrease in the counting rate of the normalization detector, shown in figure 2.10 for both gases at the higher E_{drift} values.

(a) i-butane, p = 50 mbar   (b) Ar/CO₂, p = 1 bar
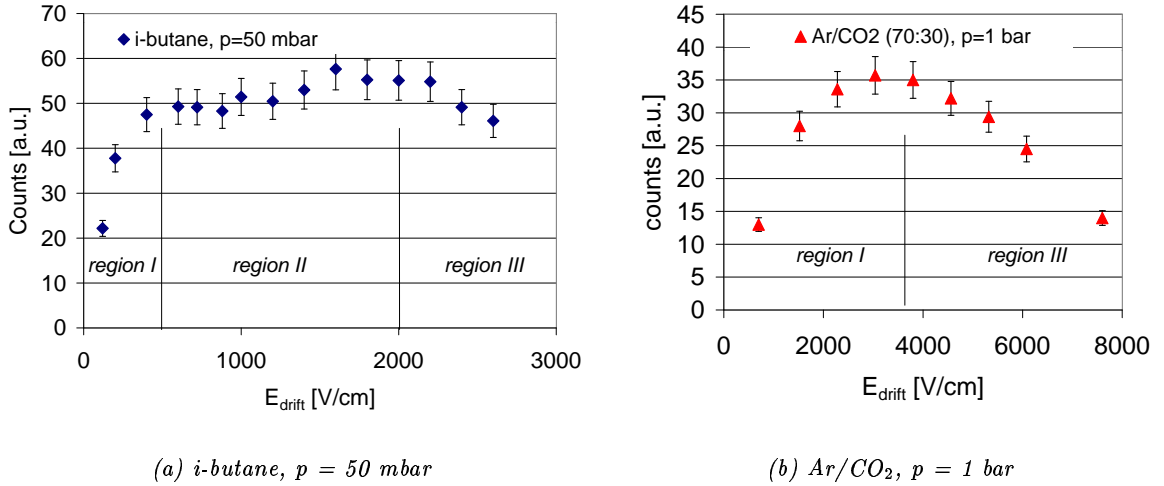
Figure 2.10: Examples of the variation of the normalization-detector counting rate as function of E_{drift}.

In this measurement, the ratio E_{drift}/E_{PC} was kept constant in order to maintain constant transparency through the mesh M_1. The initial rise (region I) in counting rate is due to the fact that at low E_{drift} values also a low E_{PC} is required, in order to keep the ratio E_{drift}/E_{PC} constant; it reflects the increase in extraction efficiency from the photocathode with increasing E_{PC} (figure 2.8). In region II a the slanted plateau occurs, reflecting the photoelectron rate as a function of E_{PC} as well. This general behavior corresponds in the GEM *and* the reference detector and therefore no special care is needed to correct for it.

However, the *decrease* of counting rate at high E_{drift} (region III), seen in i-butane as well as in Ar/CO₂, is due to loss of transparency through M_2. For Ar/CO₂ at higher pressure (0.5–1 bar) the plateau region cannot be reached (see 2.10.b) and the decrease is found to appear at rather low field values. This effect of a decrease in counting rate is restricted to the normalization detector only. For the GEM detector an intransparency in M_2 is minor important, as exclusively *preamplified* and not *single electrons* have to be transferred into the

MWPC-detector for detection. Therefore a loss of some electrons doesn't necessarily mean a loss of the whole signal there. However, for the normalization detector, this is a crucial point.

In i-butane, the data could be corrected, using the mesh transmission data (figure 2.9). In some of the measurements at atmospheric pressure, as shown in figure 2.10 for Ar/CO_2, the data at high E_{drift} values could not be corrected for loss of transmission through M_2, because the drop in counting rate occurred very early, before the onset of the photocurrent extraction plateau (namely the extraction from the photocathode is varying). In addition, the field below the mesh, E_{MWPC}, cannot be increased to improve the transparency, since this field is coupled to the MWPC-gain, which cannot be chosen freely. In such cases, the experimental data was normalized to the monte carlo results and the data is not presented as an "absolute" measurement, as e.g. in figure 2.14.b.

Nevertheless, the data can be normalized experimentally [51] by adding a parallel-gap preamplification element in front of the MWPC of the normalization detector; operating this element at *high* electric field allowed for full electron transmission through M_2, as described in detail in our paper [34]. However, this method was not applied here.

Effective GEM gain

As explained above, the real GEM gain is not directly measurable. However, the effective gain in current mode, as defined in section 2.3, can be easily measured by recording the current on the lower GEM side versus U_{GEM}, with a reversed E_{trans}. By reversing the field, all amplified electrons are collected at the GEM lower side. This current is normalized to the current without GEM amplification, recorded from the GEM electrode having both faces interconnected.
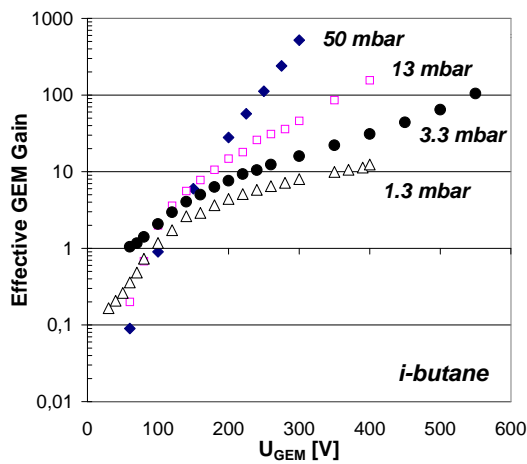
(a) i-butane at low pressure. Even at p = 3.3 mbar an effective GEM gain of 100 was reached. At 1.3 mbar the small number of ionizing collisions in the dilute gas significantly limits the maximal gain.
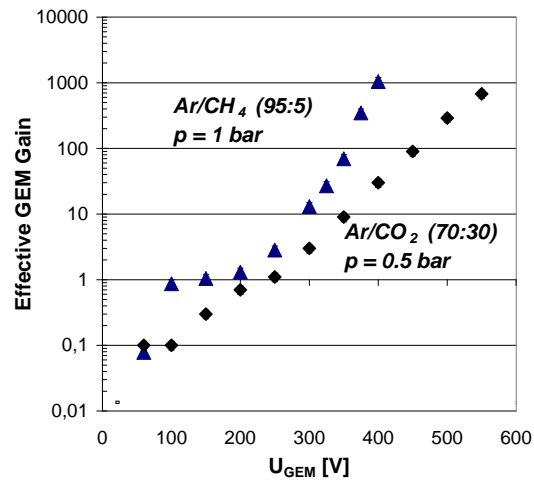
(b) Ar/CO_2 and Ar/CH_4 at atmospheric pressure. The curve for Ar/CO_2 was taken under less optimized electron transfer conditions than for Ar/CH_4, resulting in an effective gain below 1.

Figure 2.11: Effective GEM gain vs. GEM voltage U_{GEM} measured in current mode.

As shown in figure 2.11, the effective gain increases exponentially with the potential across the GEM. A detailed discussion of the GEM gain in general and its determining variables can be found in [52] and in [44] and in the references therein. In the focus of interest for this study is the phenomenon that for very low GEM voltages, the effect of the rather low transfer efficiency dominates the effective gain, resulting in values smaller than 1. It will be shown below, that after measuring the GEM transfer efficiency by the pulse counting method the effective gain can be corrected for the transfer efficiency and the real GEM gain can be extracted even for low GEM voltages.

Extraction of electrons from the GEM

Following multiplication, the electron swarm has to be extracted from the lower GEM side, for its transfer into the MWPC. The value of the electric field E_{trans} has to be sufficiently large to allow for good extraction of electrons from the GEM; however, as discussed above, it should be lower than the field at the entrance to the MWPC, to assure good electron transmission through the mesh. It should be stressed, though, that neither a value of 1 for the extraction efficiency nor a *full* transparency for the mesh M_2 is required in the GEM-detector, since the primary single electrons are already being amplified in the GEM. Even when assuming very improbable conditions, a single remaining electron arriving at the MWPC for multiplication is sufficient for detecting the original signal. Therefore the choice of E_{trans} in the measurements is not critical, as it will be shown in section 2.5.2.

MWPC and MWPC-GEM total gain

The single-electron-induced signals in the GEM- and the reference detector have to be detected with sufficiently large gas gain, to assure high detection efficiency. MWPCs provide large gas gain over a broad pressure range, of typically 10^6 or more. This and an excellent single electron detection efficiency were the reason for choosing a MWPC as a normalization detector or as the detector following the GEM.

Nevertheless, at the actual operation conditions (total gain below 10^5) the single-electron spectra have an unpeaked exponential tail [53] (figure 2.13), with its slope representing the gas gain. This tail in the pulse-height spectrum can be approximated as follows:

$$N(q) \sim N_0 e^{-\frac{q}{gain}} \tag{2.3}$$

In this equation, N_0 is proportional to the total number of detected electrons and q is the amount of charge in the electron cloud after multiplication. The *gain* is the total gain, which is given by

$$G_{\text{tot}} = G_{\text{GEMeff}} \times G_{\text{MWPC}} \quad \text{for the GEM detector.} \tag{2.4}$$

$$G_{\text{tot}} = G_{\text{MWPC}} \quad\quad\quad\quad \text{for the reference detector.} \tag{2.5}$$

In principle, the transfer efficiency is given by the number of counts in the GEM-detector divided by the number of counts from the reference detector, for *any* given total gain. However, the total number of counts is clearly dominated by the electronic noise, when integrating over the full range. Therefore a threshold to cut the external noise is strongly required for counting the "real" events only. But since the overwhelming number of counts in the pulse-height spectrum are located at rather low values of q, a large fraction of counts is inevitably lost by this cut.

A more precise technique was applied in this work, consisting in comparing only a fraction of the pulse-height distribution of the normalization and the GEM-based detectors, as depicted in figure 2.12. The total gains of the two detectors were adjusted to be identical, which means
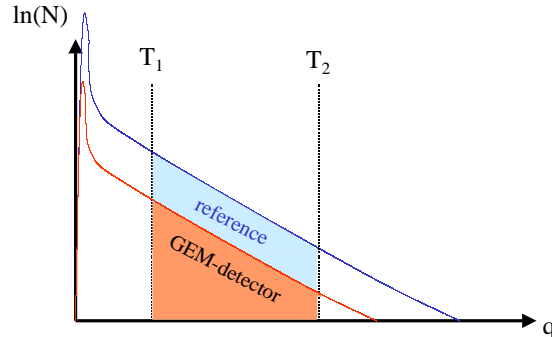

Figure 2.12: Scheme for the normalization of the counting rate. The fraction-of-counts (shaded areas) for a given total gain represents the ratio of the total number of counts, assuming a pure exponential tail in the pulse-height spectrum.

that both spectra are supposed to have the same slope. Relying on the exponential approximation of the shape of the pulse height distribution, the ratio of counts $N_{\mathrm{GEM}}(q_0)/N_{\mathrm{ref}}(q_0)$ at *any* position q_0 exactly represents the ratio of the *total* number of counts (c. f. equation 2.3) . This position can be chosen far away from the electronic noise.

In order to improve the statistics, a larger number of positions were taken into account. By defining the limits T_1 and T_2 and integrating within this limits in both detectors (shaded areas), the variation of the counting rates was compared.

For the measurements of the transfer efficiency, the total gain was set to a fixed value of 70,000, a number being large enough to provide high detection efficiencies and small enough for a stable operation for a large set of experimental conditions.

Ion-feedback limitations

Some of the measurements at lower gas pressures (e. g. Ar/CO_2 and Ar/CH_4 at high GEM gain) were hindered by the onset of strong ion feedback, which typically occurs in two-stage gas-detectors consisting of at least one GEM [54]. Depending on the gas type, pressure and GEM gain, the maximal total gain is strongly limited due to the effect of back-drifting ions, accelerated within the GEM aperture and inducing secondary electron emission at the GEM copper electrodes. This process is self-sustained, since newly created electrons are drifted towards the MWPC and induce consecutive signals with delays in the microsecond range (depending on the transfer field E_{trans}). This effect is more significant at low gas pressures. For the same values of E, the drifting ions reach higher energies between collisions, which results in a higher feedback strongly limiting the total detector gain. This effect was observed to be very strong at very low pressures of i-butane (1–2 mbar) and in some ten mbar of both Ar/CH_4 and Ar/CO_2. In conditions close to atmospheric pressure the ion-feedback effect was not observed in this setup.

(a) Spectrum in 50 mbar i-butane (E_{drift} = 200 V/cm, U_{GEM} = 180 V, E_{trans} = 800 V/cm).

(b) Spectrum in 1 atmosphere Ar/CH$_4$ conditions (E_{drift} = 2.3 kV/cm, U_{GEM} = 350 V, E_{trans} = 1.8 kV/cm).
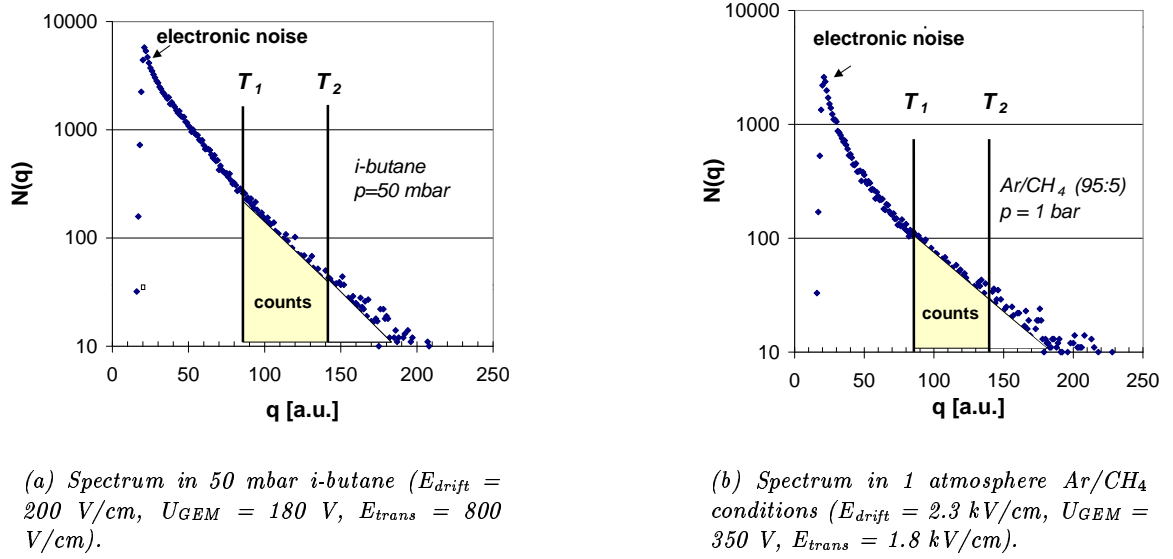
Figure 2.13: Typical single-electron spectra, recorded by a charge preamplifier

Measurements protocol

Taking into account all requirements for a reliable measurement of the GEM transfer efficiency, the concise measurement protocol for each series of data given here may help to clarify the course of the measurement:

For each gas conditions, the light intensity is set for sufficient and stable electron rates during data acquisition. Field conditions for the GEM detector and corresponding conditions for the reference detector are set. In order to provide identical total gain, chosen to be of 70,000, the MWPC voltages are adjusted in both detectors. After an accumulation of about 10,000–100,000 events, the *absolute transfer efficiency* is evaluated by a division of both counting rates, derived from the integration of the chosen part of respective pulse-height spectra.

Estimation of experimental errors

As described in section 2.4.2, an upper limit of 1% on the error due to electrons not originating from the photocathode was estimated. This and additional errors due to fluctuations in the lamp intensity, gas quality and counting rate statistics are minor important. Only in cases of very low counting rate, namely low transfer efficiency, the statistical fluctuations have a significant contribution.

The main source of error is the uncertainty in the counting rate of both detectors, of which the most important contributions are: (i) the adjustment of the total gain, which was very sensitive to small voltage deviations; (ii) the uncertainties due to deviation, in some cases, of the pulse-height spectrum from pure exponential shape. The errors were determined by varying the detector gain in a range, where the slope could not be definitely distinguished from the pure exponential slope of a "reference" graph for the given gain. These variations lead to deviations in the order of ±6%. Taking into account the error propagation law for the GEM- and the reference detector counting rate, we end up with a total error of ±8%.

2.5 Experimental Results

Though the transfer of electrons from the drift region into the GEM apertures is a process preceding the GEM multiplication, we expect the transfer efficiency to be affected by all electric fields at the vicinity of the apertures, namely E_{drift}, U_{GEM} and E_{trans}. In the following sections, the effect of each electric field will be presented and discussed separately. The measurements will also demonstrate that apart from the applied fields, the transverse electron diffusion in the gas plays a dominant role in this transfer process.

In order to accentuate the influence of the transverse diffusion, the measurements were done in i-butane at 50 mbar, being characterized by a maximum lateral spread of the electron cloud of about 600 μm per centimeter drift (for our geometry and drift fields). In contrast, the spread in Ar/CO_2 (70:30) at 0.5 bar is only 350 μm per centimeter drift (for details see section 3.2).

2.5.1 The role of E_{drift}

In figure 2.14, the absolute GEM-transfer efficiency, $\varepsilon_{\mathrm{trans}}$, as a function of the drift field, E_{drift}, is given for i-butane at 50 mbar and for Ar/CO_2 (70:30) at 0.5 bar. The ratio of $E_{\mathrm{drift}}/E_{\mathrm{PC}}$ is maintained constant in every set of measurements. The transfer efficiency shows a maximum, for all gases and GEM voltages at rather low E_{drift} values.
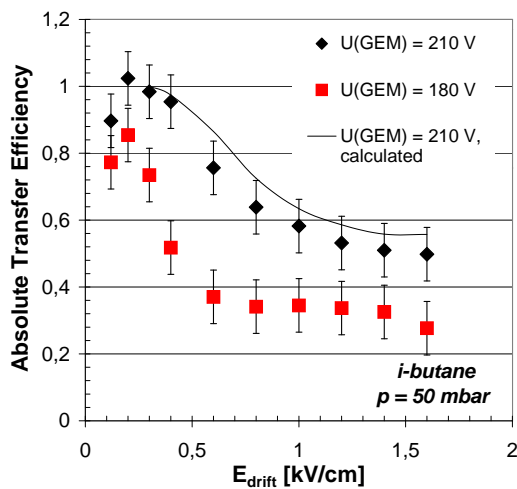
(a) Absolute measurement in 50 mbar i-butane for $U_{GEM} = 180$ V/ 210 V (gain 20/ 50).
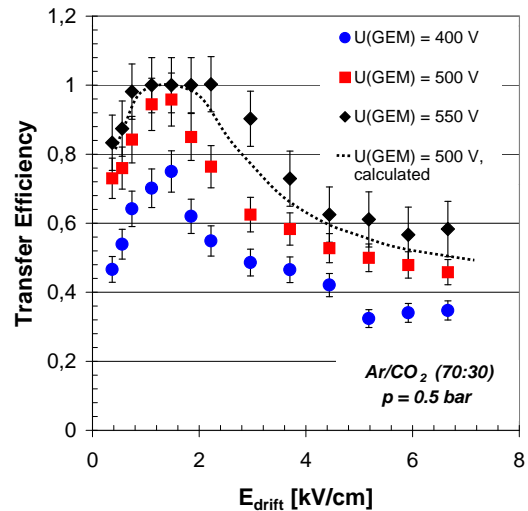
(b) Relative measurement in 0.5 bar Ar/CO_2 (70:30) for $U_{GEM} = 400$ V/ 500 V/ 550 V (gain 25/ 200 /600).

Figure 2.14: Single electron transfer efficiency vs. E_{drift}. The maxima are located at different values for E_{drift} due to a different pressure and gas type, leading to different diffusion.

It should be noted that the peak value of the transfer efficiency is not necessarily equal to 1. In both gases it turned out that even for an optimized drift field value, a full transfer efficiency is not reached if the GEM voltage is too small; this is the case for $U_{\mathrm{GEM}} < 180$ V

in i-butane and $U_{GEM} < 400$ V in Ar/CO_2 (70:30), both corresponding to GEM gain ~ 20. Below these voltages, clearly the GEM field is not sufficient to effectively focus the field lines into the apertures. The Monte Carlo simulation results shown in figure 2.14 for one set of data per each gas reproduce very well the experimental results.

In all these measurements a maximum is observed, but not necessarily for the same drift field values. This result is due to the fact that the transfer efficiency is dominated by two competing effects, (i) the electrostatic field line focusing and (ii) the electron transport parameters.
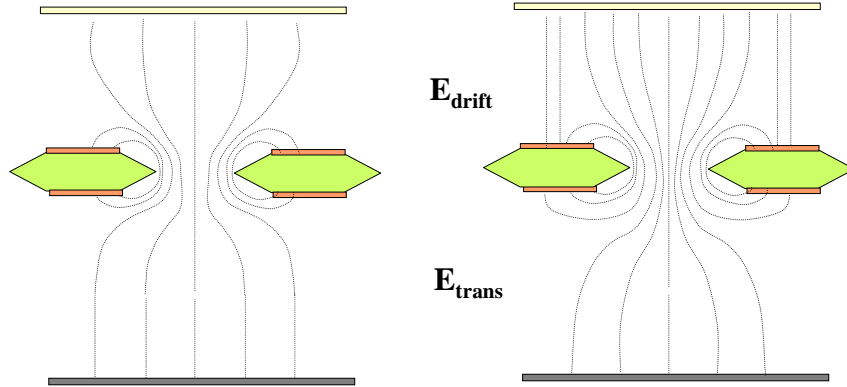
Figure 2.15: Schematic Sketch of the electric field conditions for low and high E_{drift}. Field defocusing reduces significantly the transfer efficiency for high E_{drift}.

As illustrated in figure 2.15, from a pure electrostatic point of view (assuming no diffusion and no electron-ion recombination) the transfer efficency value is high for low fields E_{drift}, however deteriorating for higher fields. The effect of field line defocusing as a function of the electric field E_{drift} is determined by the GEM voltage and the GEM geometry only. In fact, as shown in [52], the transfer efficiency can be assumed as a function of the ratio E_{drift}/E_{GEM} for a given GEM geometry.

However, another important ingredient for the actual transfer efficiency is the electron transport, mainly given by the gas type, pressure and — of course — by the electric field E_{drift}. For extremely low drift field values, the electron transport conditions are generally poor. The "ability" for electrons to follow the "perfectly focused" field lines is significantly reduced for small values of E_{drift}, thus resulting in a significantly reduced value for the transfer efficiency compared to the pure electrostatic considerations.

However, for the high field regions the transfer efficiency might be even *increased* for large diffusion gases, since electrons could be focused into the GEM aperture "accidentally", although the field lines are not.

2.5.2 The role of E_{trans}

The electric field E_{trans}, has generally a negligible influence on the GEM transfer efficiency, as demonstrated in figure 2.16, both at 50 mbar i-butane and 0.5 bar Ar/CO_2 (70:30). Over a broad range of E_{trans} values, the transfer efficiency remains almost constant.
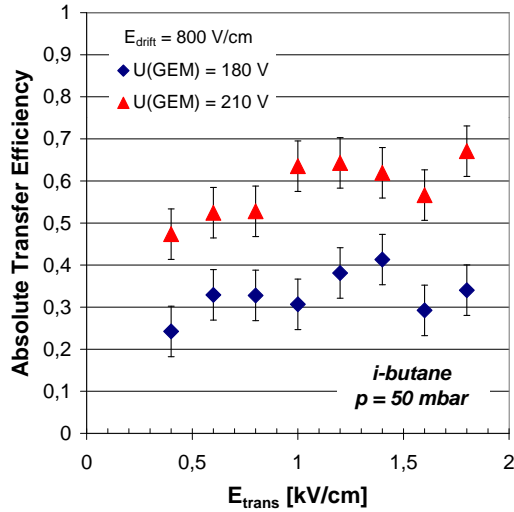
(a) Absolute measurement in 50 mbar i-butane at $E_{drift} = 800$ V/cm, for $U_{GEM} = 180$ V / 210 V (gain 20/50).
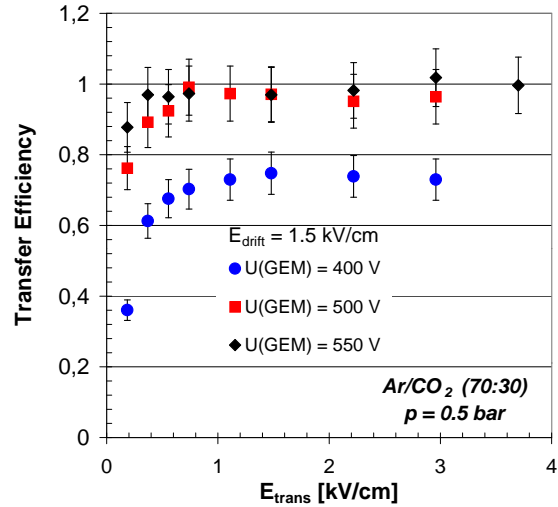
(b) Relative measurement in 0.5 bar Ar/CO_2 (70:30) at $E_{drift} = 1.5$ kV/cm, for $U_{GEM} = 400$ V /500 V / 550 V (gain 25 / 200 / 600).

Figure 2.16: Single electron transfer efficiency vs. E_{trans}. For $E_{trans} > 0.5$ kV/cm, this corresponds directly to the transfer efficiency, see text.
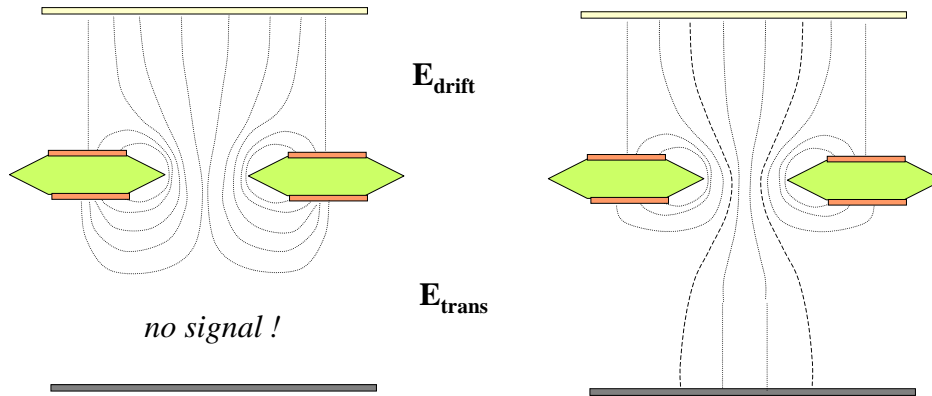

Figure 2.17: Schematic sketch of the field conditions at very low E_{trans}, where the signal cannot propagate towards the MWPC, compared to "normal conditions". Please note, that as long as at least 1 electron can be transferred to the MWPC, the method is reliable.

Only at very low E_{trans} field values (i. e. $E_{trans} < 0.5$ kV/cm in Ar/CO_2 (70:30)) the measured counting rate drops significantly, due to the collection of all multiplied electrons on the lower GEM electrode, rather than their transport into the MWPC, which affects the counting rate in the GEM-MWPC detector, as visualized in the schematic sketch in figure 2.17. This means that the assumption, that once the electron is multiplied in the GEM, the signal is

actually detected, doesn't hold for low values of E_{trans}. Therefore, in this regime, the counting rate does not directly reflect the transfer efficiency.
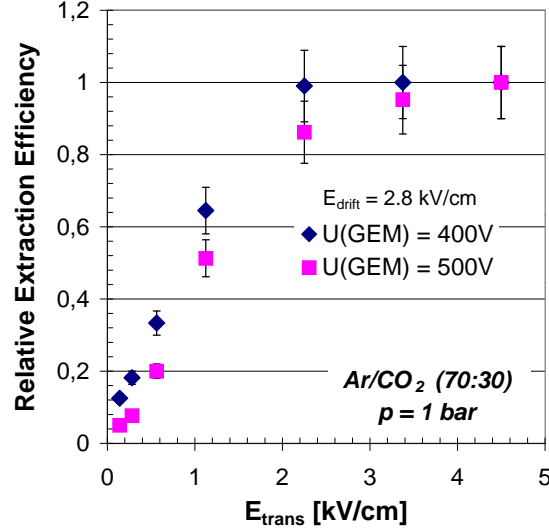
Figure 2.18: Relative electron extraction efficiency vs. E_{trans}. Results are shown for two GEM gains in 1 bar Ar/CO_2 (70:30) at $E_{drift} = 2.8 \; kV/cm$

In contrast to the transfer efficiency $\epsilon_{\text{transfer}}$ (i.e. the fraction of the electrons transfered *to* the GEM aperture for multiplication), the extraction efficiency, $\epsilon_{\text{extract}}$ (i.e. the fraction of GEM-amplified electrons that are transferred *from* the GEM to the MWPC) cannot be directly measured by our method, but it can be derived in an indirect way: Due to the fact that the total gain is kept constant during the measurement while varying E_{trans}, a loss in the extraction efficiency results in a drop of pulse height, which in turn is reflected by a need for an increase in the MWPC voltage. From the gain increase required to reestablish the original total gain, one can deduce the fraction of lost electrons, as shown in figure 2.18. This method only provides a relative estimate; the plateau shown in figure 2.18, for Ar/CO_2 (70:30) at atmospheric pressure, for $E_{\text{trans}} > 2$ kV/cm (for $U_{\text{GEM}} = 400$ V) and for $E_{\text{trans}} > 4$ kV/cm (for $U_{\text{GEM}} = 500$ V) does not necessarily indicate a condition of a full extraction.

2.5.3 The role of U_{GEM}

A large effect on the single-electron *transfer efficiency* is that of the GEM voltage. The dependence of the transfer efficiency on the GEM voltage is shown for i-butane at 50 mbar and for Ar/CO_2 (70:30) at 0.5 bar in figure 2.19.

This dependence is understood from purely electrostatic considerations, as it is visualized in figure 2.20. At very low U_{GEM} values most of the field lines in the drift region end at the upper GEM electrode. This results in a very small probability of electrons focusing into the apertures and therefore in very low transfer efficiency. When increasing the GEM voltage, a steep increase in transfer efficiency was observed. A saturation (not necessarily being at 100% efficiency) was observed at GEM gain values in the order of 100 for both gas conditions; however, this saturation has to be considered a preliminary result, since measurements for higher GEM gains were excluded due to high voltage problems. The general behavior is due
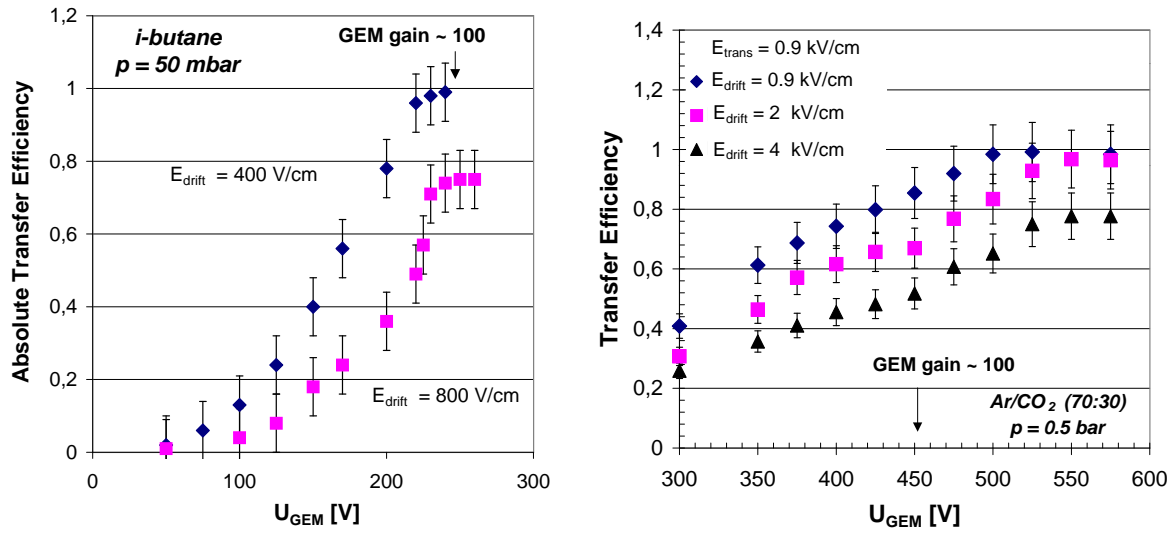
(a) Absolute measurement for two different sets
of drift field values, in 50 mbar i-butane. The
maximal transfer efficiency is obtained at about
GEM gain ≈ 100.

(b) Relative measurement at E_{trans} = 0.9 kV/cm
and 3 different values of E_{drift} (0.5 bar Ar/CO_2).
The maximal ϵ_{trans} is at GEM gain > 100. The
data lacks absolute normalization counting rate,
and is normalized according to the simulation.
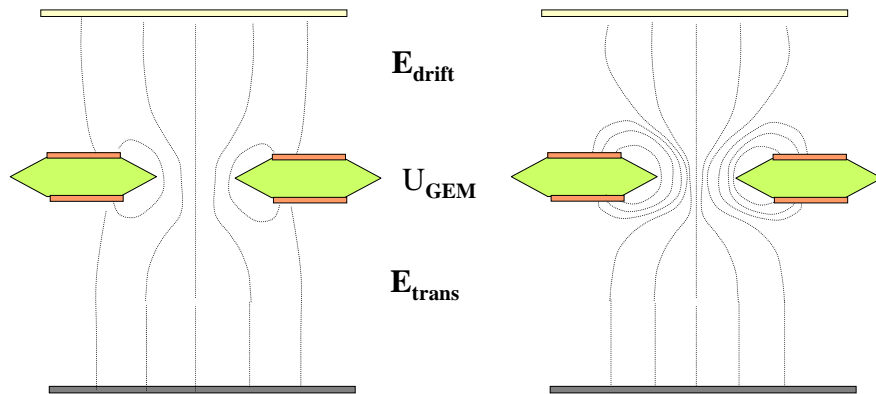
Figure 2.19: Single electron transfer efficiency vs. U_{GEM}

Figure 2.20: Sketch of the electric field conditions for low and high U_{GEM}, illustrating that the
transfer efficiency strongly increases with the applied voltage.

to improved field-lines focusing with increasing GEM field: the maximum transfer efficiency
value is dictated by the geometry of the GEM (aperture diameter and spacing) and by the
transverse electron diffusion.

As explained in section 2.4.2, by knowing the transfer efficiency for a given E_{drift}, as a function of U_{GEM}, the real GEM gain can be separated from the effective gain in current mode ($G_{\text{real}} = G_{\text{eff}}/\varepsilon_{\text{extract}}$). This procedure was followed for the GEM gain results in i-butane at 13 mbar (figure 2.21). In the range of 0–20 V for $p = 13$ mbar, there is no amplification in the GEM and the real gain is about 1. The gain increases purely exponentially at higher potentials.

(a) Transfer efficiency   (b) Effective and real GEM gain
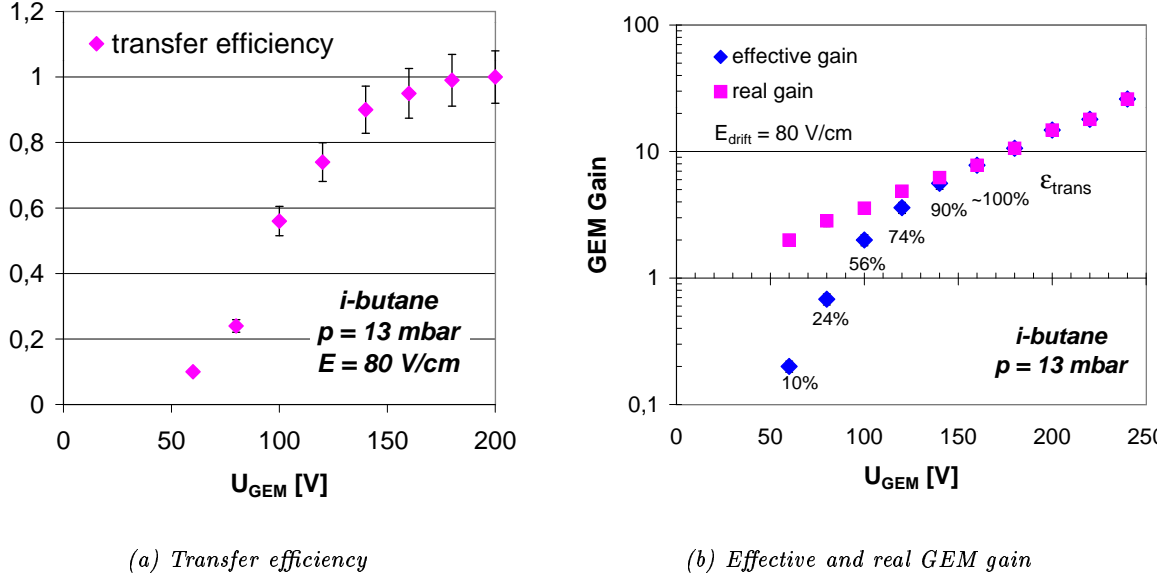
Figure 2.21: The transfer efficiency and the effective/ real GEM gain as a function of U_{GEM}. The effective GEM gain as measured in current mode (figure 2.11) was corrected by the measured absolute transfer efficiency (at the same E_{drift}) to provide the real GEM gain.

2.6   Summary

The three parameters involved in the GEM multiplication process (the *transfer efficiency*, the *real gain* and the *transfer efficiency*) mainly depend on the surrounding fields, as depicted in figure 2.22.

For the first time, the absolute efficiency of single electron transfer through GEM was measured, namely the probability for a single electron, deposited in the gas-volume preceding the GEM, to be multiplied in the GEM aperture. It was shown that the transfer efficiency is defined not only by the geometrical parameters of the GEM electrode, but it depends in a rather critical way on the transport of electrons in the gas gap preceding the GEM and on the field-line focusing into the GEM apertures. The different processes involved are sometimes competing, leading to a large variability of the transfer efficiency. Consequently the measurements of the present study were carried out as function of all electric fields and under a range of gas types and pressures. This has lead to a complete understanding of the role played by each variable, which will enable to optimize the design of GEM-based devices in terms of their detection efficiency.
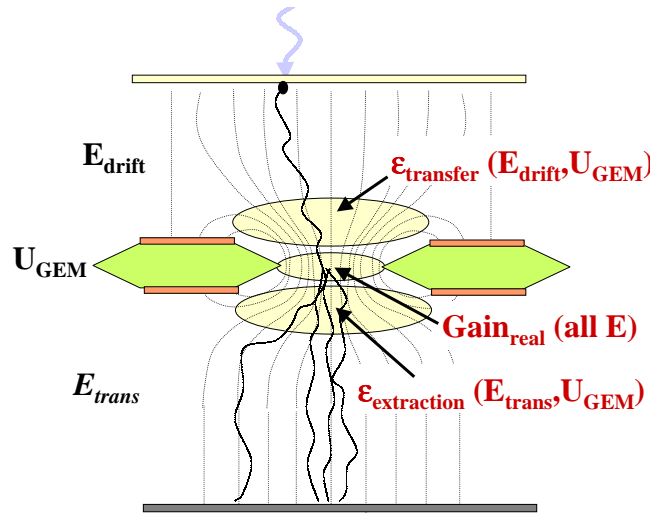
Figure 2.22: Sketch of the GEM multiplication process as a function of the electric fields

The results can be summarized as follows:

- The transfer efficiency is strongly affected by the transverse diffusion of the electrons, drifting under the focusing field towards the GEM aperture. As depicted in figure 2.14, especially in the very low field regions ($E_{\text{drift}} < 1.5$ kV/cm) the transfer efficiency is significantly reduced due to electron diffusion.

- In the case of a slightly increased field E_{drift}, by tuning the ratio of $E_{\text{drift}}/U_{\text{GEM}}$ to be high enough, conditions can be found for any gas pressure and type, where the electrons are well focused into the GEM apertures and the transfer efficiency has a maximum. This maximum, however, is not necessarily equal to 100%, its value depends on the GEM geometry and gain.

- Increasing E_{drift} invariably leads to a loss of efficiency due to loss of focusing, as shown in figure 2.14 and 2.16.

- The role of U_{GEM} is well demonstrated in figure 2.19, showing that the transfer efficiency increases roughly exponentially in a wide regime of U_{GEM}. This result accentuates the importance of field-line focusing, but also the fact that the maximal transfer efficiency, even if exhibiting a — mostly very narrow — plateau region, maybe smaller than 100%.

- The field E_{trans}, in the gap following the GEM, has a minor influence on the measured transfer efficiency. However, in the regime of very low field ($E_{\text{trans}} < 0.5$ kV/cm) the measurement of the transfer efficiency was restricted for principle reasons.

Regarding the above summary of results it should be noted that all data were measured with a single GEM geometry, which was not necessarily optimized. Therefore, while the results are qualitatively valid, and the general trends are reliable, the specific numerical values may not be general.

It is obvious, that in applications, where only a few or even single electrons are created, the transfer efficiency of the GEM strongly influences the detector efficiency. Nevertheless,

also in applications where e. g. minimum ionizing particles (MIPs) are detected and in the order of 10 primary electrons are created, an optimization of the transfer efficiency is strongly requested for two reasons: (i) to keep the detection efficiency of the GEM device close to 100 % and (ii) to optimize the required operation voltages. Especially in high rate hadron beams, optimized operation conditions are required for an effective reduction of the discharge probability (as described in detail in chapter 5.4).

Chapter 3

Efficiency with electron preamplification

In some GEM applications high electric fields in the gap preceeding the GEM-device are strongly required. One example is the gas avalanche photomultiplier [38], where high fields near the photocathode are requested to prevent photoelectron backscattering from the gas molecules into the photocathode. As a consequence, the transfer efficiency is poor for large fields E_{drift}, due to the defocusing of field lines, as demonstrated in the last chapter.

However, when further increasing the field E_{drift}, parallel plate amplification in the gap preceding the GEM can be initialized. Of particular interest is the confirmation of the hypothesis that a full *collection efficiency* is attainable when moderately amplifying the initially deposited single electrons, prior to their collection and multiplication by the GEM.

3.1   The electron collection efficiency

Allowing for a moderate electron preamplification should provide large fields near the photocathode and it should lead to a dramatic enhancement of the detection efficiency of single electrons [54]. It will be shown that conditions can be found, in which at least one of the preamplification-induced secondary electrons reaches a GEM aperture, leading to a detectable event. This was demonstrated experimentally, though in a *relative* way [54] and by Monte Carlo simulations, indicating the possibility of reaching conditions for full single-electron detection efficiency [42].

We define the *collection efficiency*, ϵ_{coll}, as the fraction of electrons deposited in the gap above the GEM, for which, after preamplification, at least one secondary electron is transferred and multiplied in the GEM, when the electron diffusion is sufficiently high (see figure 3.1). This parameter equals the *detection efficiency*, provided that no signal is lost after the GEM amplification.

Experimental results of this parameter in several gases and field conditions are presented first. These are well confirmed by Monte Carlo simulations, performed at CERN [46]. After the experimental part, a model is presented for the collection efficiency, explaining the experimental results.

Transmission of at least 1 electron:
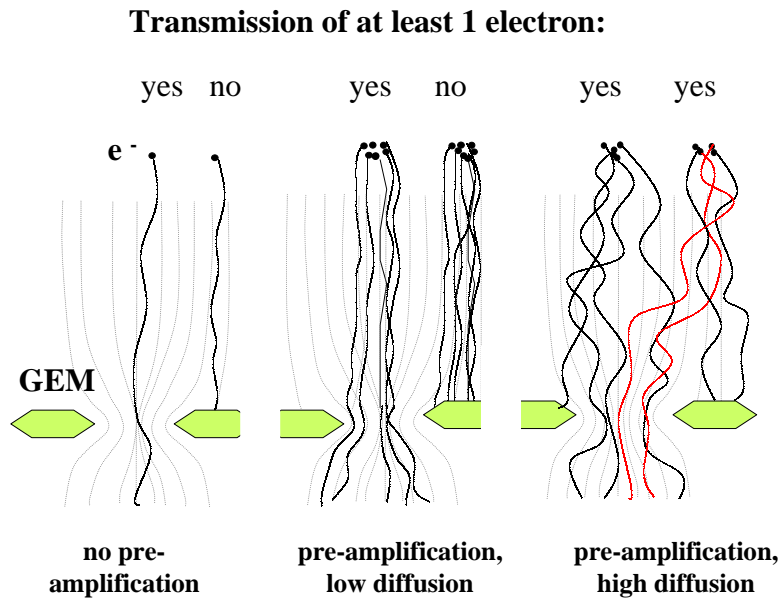
Figure 3.1: *Schematic picture of single-electron transport in the drift gap preceding the GEM, at low (no preamplification) and high (preamplification) drift field values. The last case is depicted for low and high electron diffusion. The GEM amplification of the electrons is not depicted here.*

3.2   The experimental setup

The experimental setup for the measurement of the absolute value of the collection efficiency is identical to the concept described in detail in section 2.4. The number of counts (at a fixed total gain) in the GEM-detector for a given irradiation rate is normalized to the counting rate of the reference detector, operated at corresponding conditions. The normalization remains correct since the preamplification of the electrons has intrinsically no influence on the counting rate.

In the following, the results obtained for the absolute GEM collection efficiency, in the preamplification mode, are presented. Due to the fact, that the transport parameters, namely the electron diffusion and drift, scale as a function of E/p (the "reduced electric field"), the x-axis was chosen accordingly in the following plots. In addition, also the first Townsend coefficient, α, being an important ingredient for the parallel-plate amplification, can be approximated as function of E/p (and E) [55, 6].

The electron diffusion

The data is arranged according to the size of the transverse electron diffusion, since the lateral spread of the electron cloud after some drift was supposed to play a decisive role for the collection efficiency. The order parameter "large", "intermediate" and "small" depends on the actual detector geometry and will be specified, when presenting a "simple model" in section 3.4.1 and when discussing the experimental results.

The spread of the electron cloud $\sigma_{\text{transverse}}(d)$ (in μm) after a drift length d is given by the

following equation:

$$\sigma_{\mathrm{transverse}}(d,E,p) = \sigma_0(E) \cdot (d/p)^{1/2} \qquad (3.1)$$

The *specific transverse diffusion* $\sigma_0(E/p)$ at atmospheric pressure was calculated [46] for the three gases used in this study and the results are plotted in figure 3.2.
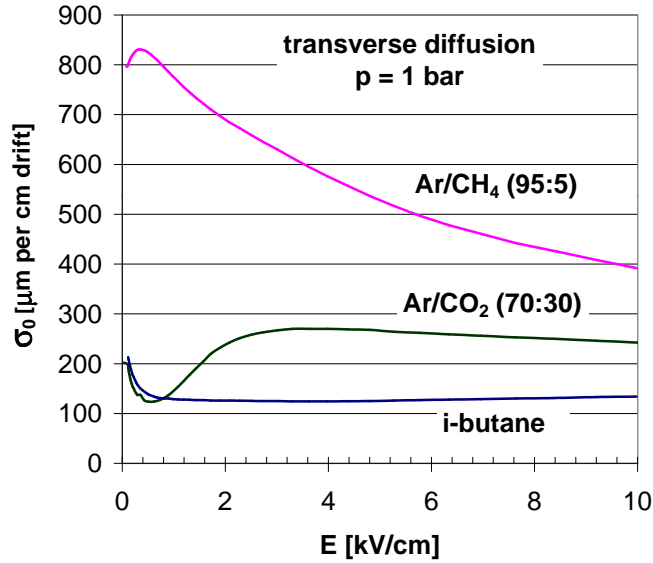
Figure 3.2: The transverse diffusion coefficient σ_0 vs. the drift field E at atmospheric pressure for the gases studied in this work. This value has to be corrected for the actual pressure according to equation 3.1

According to equation 3.1, conditions with very high electron diffusions can be easily obtained for *low* gas pressure. We have chosen i-butane, known for its stable low-pressure operation [54] for the high diffusion measurements. Adequate operation conditions for the GEM at 3.3, 13 and 50 mbar could be guaranteed. A measurement for very low pressure ($\approx$ 1 mbar) was excluded due to the small number of ionizing collisions in the quite *dilute* gas volume of the GEM aperture, thus limiting the effective GEM gain to values below 10. Furthermore, this measurement was seriously affected by ion-feedback, falsely increasing the number of counts due to self-sustained signal feedback.

At atmospheric pressure, the electron diffusion is considerably reduced, thus excluding high values for the transverse diffusion. For this study, the range of intermediate and low diffusion was covered with Ar/CH$_4$ (95:5) and Ar/C0$_2$ (70:30) respectively (c. f. figure 3.2). Although pure i-butane provides an even smaller transverse diffusion value at atmospheric pressure, this gas is only suited for low pressure measurements due to the comparatively high operation voltages, required for high gain operation.

3.3   The experimental results

3.3.1   Preamplification

As an independent measurement, the preamplification gain in all gases was studied in "current mode", namely by recording the electron current on mesh M_2 (as depicted in figure 2.7) as a function of the applied electric field E_{drift} and normalizing it to the current without preamplification. The results are plotted in figure 3.3 for i-butane for different pressures and in figure 3.4 for Ar/CH_4 and Ar/CO_2.   For a given gas, the onset of amplification starts for

(a) Low fields   *(b) High fields*
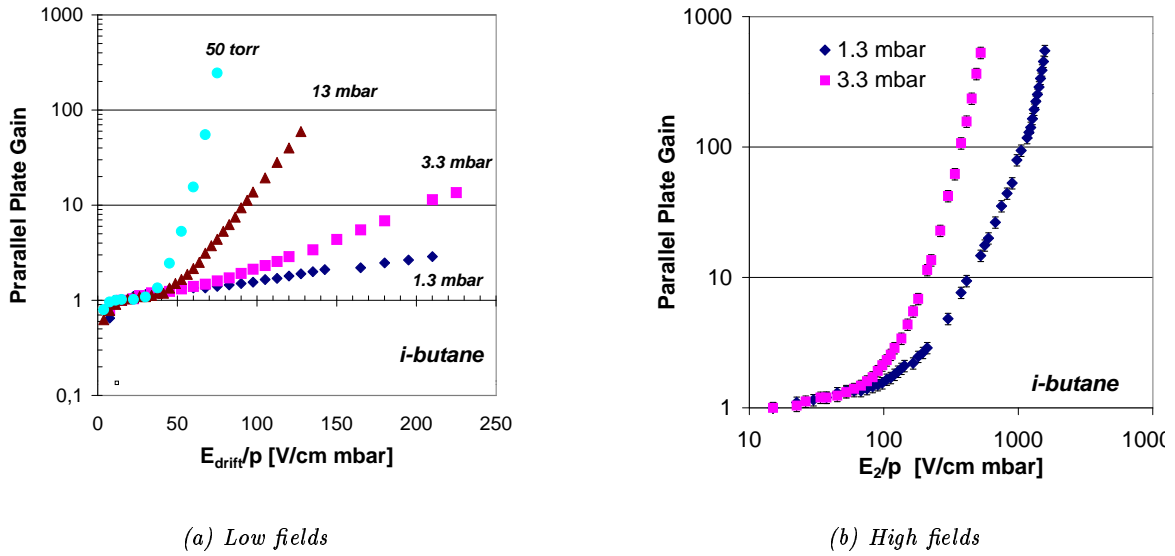
Figure 3.3: Preamplification gain vs. field, measured in current mode in i-butane.
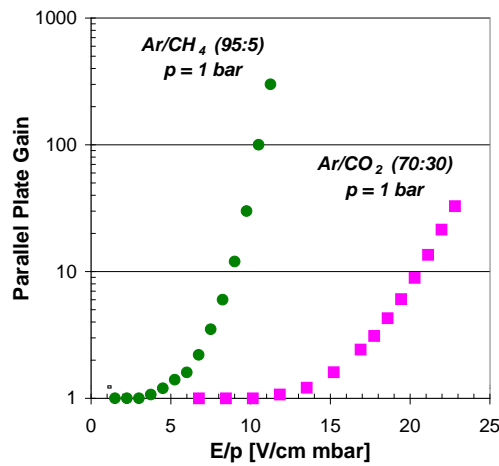
Figure 3.4: Preamplification gain vs. field, measured in current mode in Ar/CH_4 (95:5) and Ar/CO_2 (70:30) at atmospheric pressure.

corresponding E/p-values. However, the slope is not identical since for low pressure conditions the gas is diluted, thus significantly reducing the probability for ionizing processes as described in detail e. g. in [56].

3.3.2 Collection efficiency

Gases with high transverse diffusion

In figure 3.5, the experimental data of the electron collection efficiency in 50 mbar i-butane are plotted as a function of E_{drift}. The x-axis is divided into two segments, the "drift" region where the field is too low for preamplification, and the "preamplification" region, where electron multiplication in the parallel plate mode takes place. On the top axis the preamplification values are noted, indicating that a *full collection* is typically obtained at preamplification > 20. In these conditions the effect of field line defocusing is found to be more than compensated by the avalanche statistics.
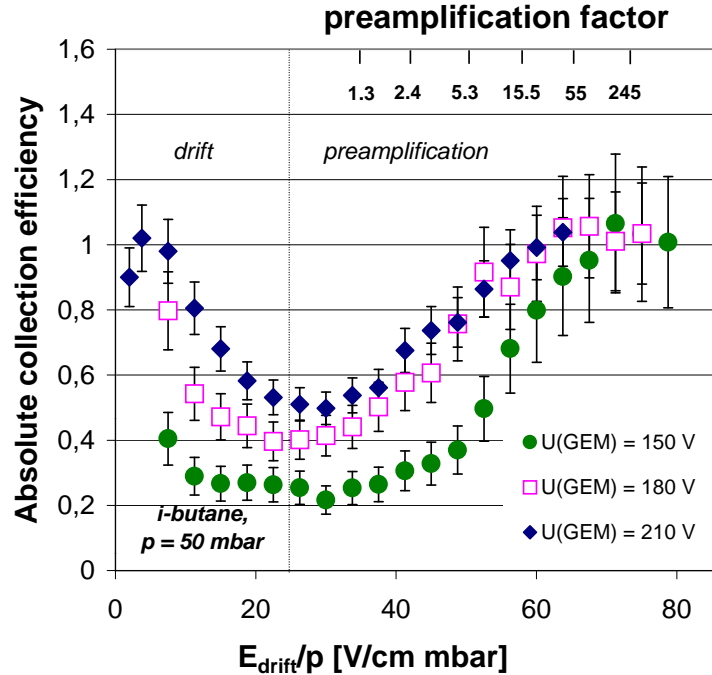
Figure 3.5: Absolute electron collection efficiency vs. E_{drift}, extended to high E_{drift} values, in the preamplification regime. The results, measured in 50 mbar i-butane, are shown for U_{GEM} =150 V/ 180 V/ 210 V (GEM gain: 8/20/50) at E_{trans} = 800 V/cm.

Similar measurements were done for p = 3.3 and 13 mbar. Figure 3.6 shows the results, indicating rather large differences of the E/p-values, at which full collection efficiency is reached: from about 60 V/cm mbar at 50 mbar, to 110 and 225 V/cm mbar at the respective pressures of 13 and 3.3 mbar. These results are well confirmed by the Monte-Carlo simulations (c. f. section 2.2).
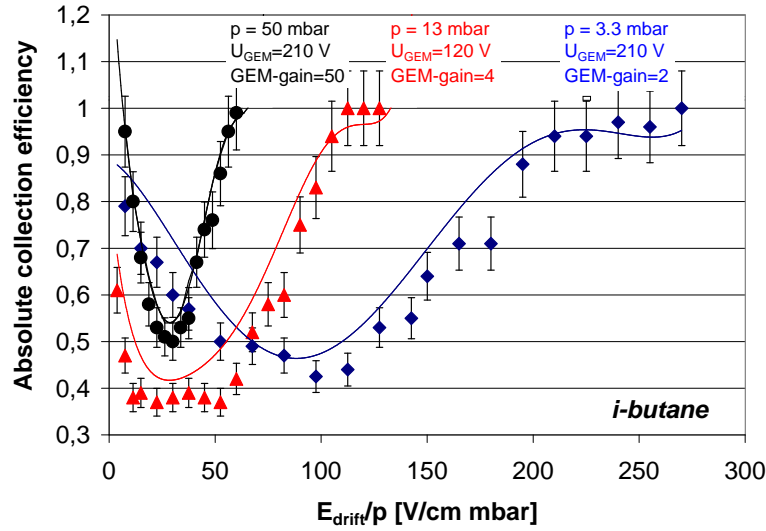
Figure 3.6: Absolute electron collection efficiency vs. E_{drift}, extended to the high E_{drift} values (preamplification regime) for i-butane at 3.3, 13 and 50 mbar. The lines represent the results of the monte-carlo simulations [46]

Gases with intermediate transverse diffusion

The experimental results of the GEM collection efficiency in Ar/CH_4 (95:5) are presented in figure 3.7 for three different GEM voltages.
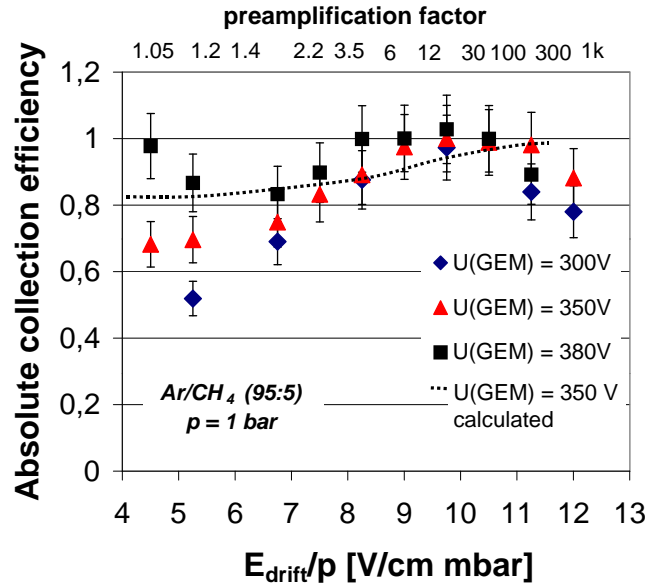
Figure 3.7: Absolute collection efficiency in 1 bar Ar/CH_4 (95:5) for $U_{GEM} = 300$ V/ 350 V/ 380 V (GEM gain 12/80/500) vs. E_{drift} in the preamplification regime together with the simulation results.

The full collection plateau is typically obtained at preamplification > 15. Compared with the previous data for low-pressure i-butane, measured at about the same GEM gain of ~ 100, the collection efficiency does not drop below 50%. This is due the fact that gas preamplification at one atmosphere Ar/CH$_4$ (95:5) is initiated at rather low values of E/p in comparison with the gases previously investigated.

Please note that in contrary to i-butane at low pressure, the collection efficiency *deteriorates* when further increasing the preamplification above ~ 30. This effect, which results from the change in electron diffusion with increasing drift field (figure 3.2), will be explained with a simple model, presented in section 3.4.1.

Gases with low transverse diffusion

In figure 3.8 it is shown that in Ar/CO$_2$ (70:30) at atmospheric pressure (low diffusion gas) the GEM collection efficiency remains very low even at very high E_{drift}/p values, corresponding to a preamplification factor of up to 60. It means that for this gas the preamplification is not sufficient to compensate for electron losses, as depicted schematically in figure 3.1. The model in section 3.4.1 will further explain this point.
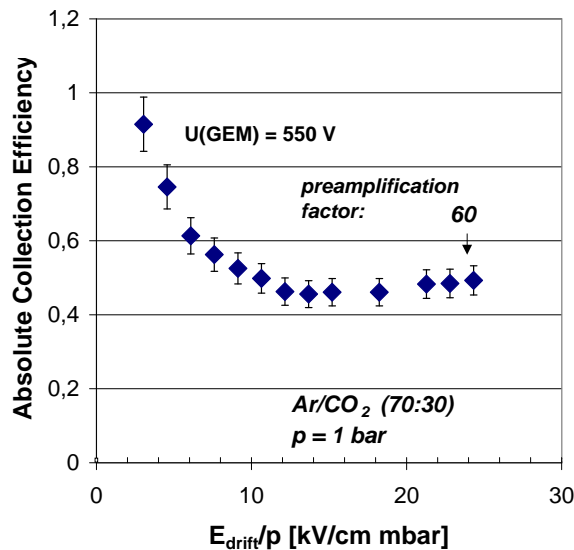
Figure 3.8: Absolute collection efficiency vs. E_{drift} in the preamplification regime in Ar/CO$_2$ (70:30). The results are shown for U_{GEM}=550 V (300 gain) and E_{trans} = 1.5 kV/cm.

It should be noted here, that it was not possible to further exceed the preamplification factor in the drift gap, since three times the GEM was destroyed when preamplification factors larger than ≈ 100 were obtained. As a consequence of the poor transfer efficiency, the potential of the GEM upper side became very negative. Discharges in the GEM were induced, sometimes even propagating towards the mesh M$_1$. This breakdown caused a complete destruction of the GEM[1].

---

[1]see also "multiple electrode sparks" in chapter 5.4

Summarizing the experimental results obtained in different gases, it was demonstrated that conditions can be found for reaching 100% collection efficiency, provided the transverse diffusion is "high". For intermediate diffusion values, high collection efficiency could be reached; however, it deteriorated at further high values of E_{drift}/p and at higher GEM amplification factors. For gases with low diffusion, the collection efficiency remained low, even at high preamplification factors.

3.4   Modeling the GEM electron collection efficiency

3.4.1   The model

The experimental results can be well explained by a simple model, based on statistical arguments. If the transverse diffusion and the preamplification gap are large enough, it can be assumed that the secondary electrons, created in the preamplified cluster, are equidistributed in the gas volume preceeding the GEM (or at least within one elementary cell). In this conditions, it can also be assumed that the single electron transfer efficiency $\varepsilon_{\mathrm{trans}}$, measured for a given U_{GEM} in collection mode, is valid for the conditions of preamplification as well. Then, with a preamplification factor PA, the collection efficiency $\varepsilon_{\mathrm{collect}}$ is given by the following equation:

$$1 - \varepsilon_{\mathrm{collect}} = (1 - \varepsilon_{\mathrm{trans}})^{PA} \tag{3.2}$$

However, even for high-diffusion gases, the collection efficiency is overestimated in equation
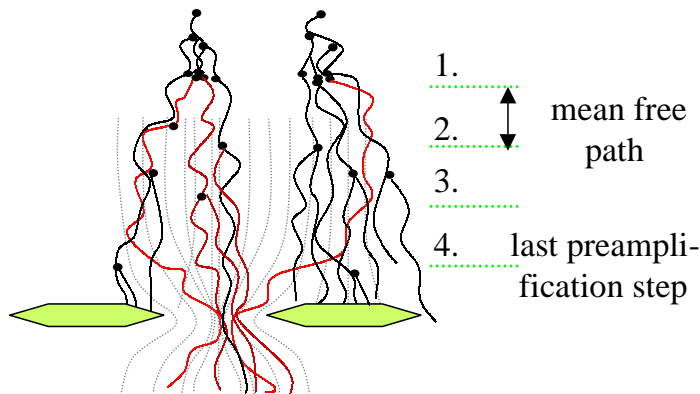
Figure 3.9: Sketch of the avalanching process in the parallel-plate mode preceeding the GEM amplification. The mean free path gives the average distance between two ionizing collisions. Electrons, created in the last steps, experience only a small spread, in contrast to those electrons created in the first steps.

3.2, since the secondary electrons are created along the drift gap and thus travel different distances, experiencing a different spread in the lateral dimension (as visualized in figure 3.9).

Particularly, secondary electrons created in the last few preamplification steps, close to the GEM aperture, do not have a sufficient drift length to exhibit a significant diffusion. For

a better approximation for equation 3.2 the replacement of PA by $PA/2^N$ is proposed:

$$1 - \varepsilon_{\text{collect}} = (1 - \varepsilon_{\text{trans}})^{PA/2^N} \tag{3.3}$$

The parameter N may be considered as a "fit parameter" for the experimental data, representing the number of amplification steps that have to be neglected.

In case of no diffusion, the preamplification will not increase the collection efficiency, as all secondary electrons have similar drift paths and therefore the same "destiny" as the primary electron. In this extreme condition, $2^N = PA$ and equation 3.2 can be replaced by

$$\varepsilon_{\text{collect}} = \varepsilon_{\text{trans}} \tag{3.4}$$

3.4.2   Quantification of the diffusion for the given geometry

Based upon the considerations above, we can specify the criterion for "high" and "low" diffusion: To benefit from the preamplification the maximum spread of the electron cloud, $w = \sigma_{\text{transverse}}(d)$, has to be of the order of the GEM pitch, g, as it is visualized in figure 3.10. The drift distance d is an important input parameter for the calculation. In our geometry, w should be typically $> 200\mu$m in order to increase collection efficiency by preamplification.
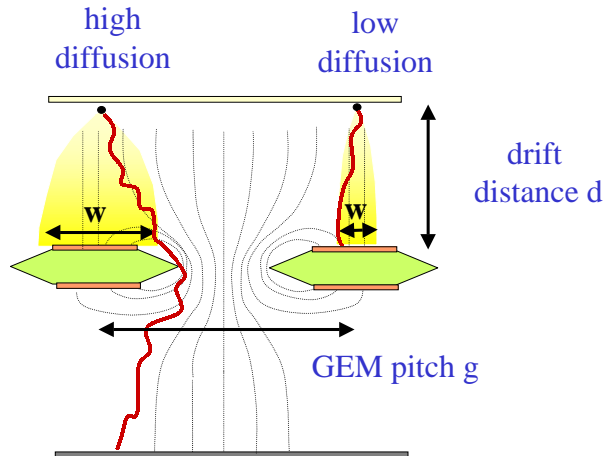
Figure 3.10: The parameter influencing the lateral size of the electron cloud close to the GEM w are the transverse electron diffusion and drift gap d. Criterion for a "large diffusion" is w > g (the GEM pitch).

The validity of the model was tested in different experimental conditions, as described below. Since $\varepsilon_{\text{trans}}$ is not measurable for high drift fields, i. e. above the onset of preamplification, the value measured at the highest drift field prior to amplification (which is the lowest $\varepsilon_{\text{trans}}$ measured) was used and it was assumed to be constant as a function of E_{drift}. As shown in figure 2.14, the effect of field line defocusing is small for high E_{drift}.

A list of all gases used in this study and the corresponding drift parameters are summarized in table 3.1, illustrating the conditions for "large" or "small" transverse diffusion. As shown in figure 3.2, the value for the specific transverse diffusion σ_0 only minimally varies as a function of the applied field for i-butane and Ar/CO_2, thus only the mean value is given here. This is different for Ar/CH_4, thus in this case the minimal and maximal value are shown.

diffusion	gas type	σ_0 [μm/cm drift]	pressure p [mbar]	max. lateral spread w [μm]
high	i-butane	130	3.3 13 50	785 400 200
intermediate	Ar/CH$_4$	300–800	1000	100–280
small	Ar/CO$_2$	250	1000	85

Table 3.1: Table of the lateral electron spread for the three gases of this study. The pitch of the GEMs used in this study was g = 140 μm

3.4.3   Comparison of the experimental results

Conditions of large transverse diffusion

In figure 3.11 the experimental electron collection efficiency for i-butane in all three pressures is presented as function of the preamplification factor (c. f. section 3.3.1). In this plot, the decrease in the collection efficiency at low fields is omitted, since all data points of this region belong to the same x-value "1".
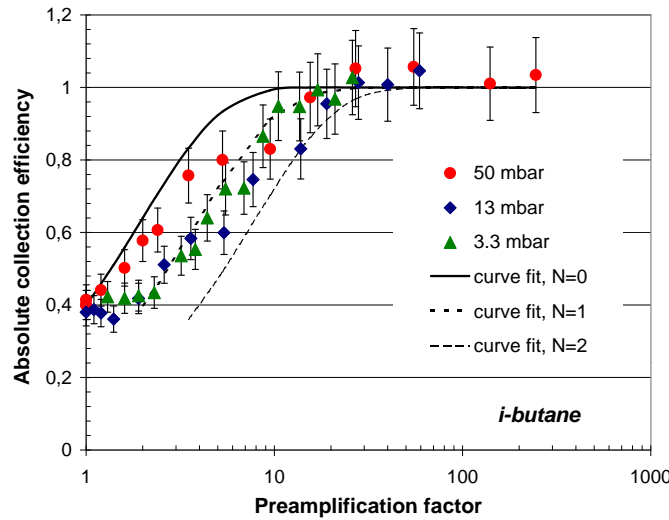
Figure 3.11: Absolute electron collection efficiency vs. preamplification, in 3.3, 13 and 50 mbar i-butane. U_{GEM} = 90 V/ 120 V/ 180 V (GEM gain: 2/ 4/ 20) at 3.3, 13 and 50 mbar, respectively. The solid and dashed lines are the electron collection efficiency functions predicted by the simple statistical model presented in section 3.4.1. Omitting the secondary electrons created in the last multiplication step (fit parameter N = 1) provides a good agreement with the experimental results.

The data almost overlap and full collection efficiency is reached, in all three conditions, approximately at the same preamplification factor of 20, since the electric fields for all data sets were chosen to result in a minimum for $\varepsilon_{\text{trans}}$ at about 40 %.

Although the transverse diffusion is higher by a factor of 4 at a pressure of 3.3 mbar compared to the one at 50 mbar, both data sets are almost overlapping within the error bars. This result suggests that as soon as the size of the electron cloud is larger than the inter-hole-distance, the collection efficiency cannot be increased any further. From the same data we learn that the model fits best when using $PA/2$, namely when the last amplification step is indeed neglected (equation 3.3).

Conditions of intermediate transverse electron diffusion

The conditions in Ar/CH_4 (95:5) at atmospheric are very interesting for testing the model, since the value for w varies in wide range, being larger than the GEM-pitch for low fields, however significantly smaller for high fields.

The collection efficiency data for $U_{\text{GEM}} = 350$ V is shown in figure 3.12 as a function of the preamplification factor. On one hand it was shown (see figure 3.7) that the diffusion in this gas is sufficient to reach a collection efficiency of 100%, even at rather low GEM gains. In this range, equation 3.3 with a small N ($N = 1$) is well reproducing the data, as shown in figure 3.12. On the other hand, as a result of the decreasing transverse diffusion with increasing field, the collection efficiency deteriorates when going to very high fields (data points at $E_{\text{drift}} > 10$ V/cm mbar, in figure 3.7) and thus large preamplification factors ($PA > 100$, last data points in figure 3.12). In this region of poor diffusion ($\sigma_{\text{transverse}} \approx 100\mu\text{m}$), small values for the fit parameter N do not reflect the experimental graph any more.
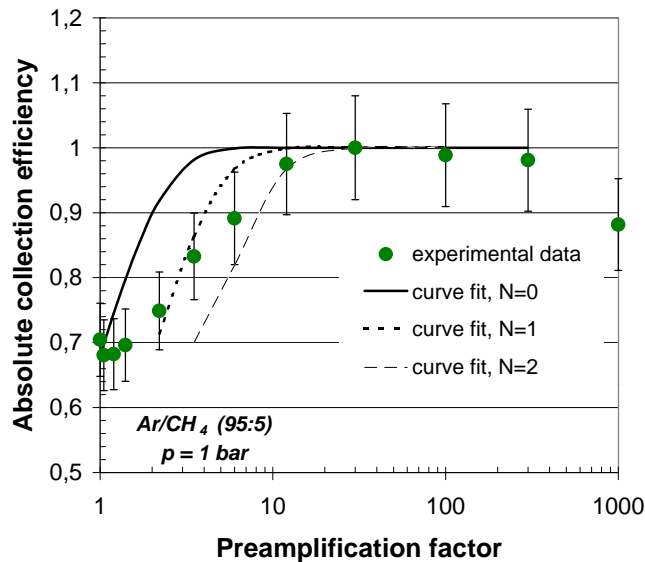
Figure 3.12: Absolute electron collection efficiency vs. preamplification, in Ar/CH_4 at atmospheric pressure. $U_{GEM} = 350$ V, corresponding to GEM gain of 80, $E_{trans} = 1.5$ kV/cm. Omitting the last amplification step ($N = 1$) provides a good agreement with the experimental results.

Conditions of small transverse electron diffusion

The size w of the electron cloud close to the GEM surface in Ar/CO_2 (70:30) is below the GEM pitch g for the entire field range. Therefore, preamplification in this gas is not expected to enhance the collection efficiency, as demonstrated in figure 3.13 and described by the limit $\varepsilon_{\text{collect}} = \varepsilon_{\text{trans}}$.
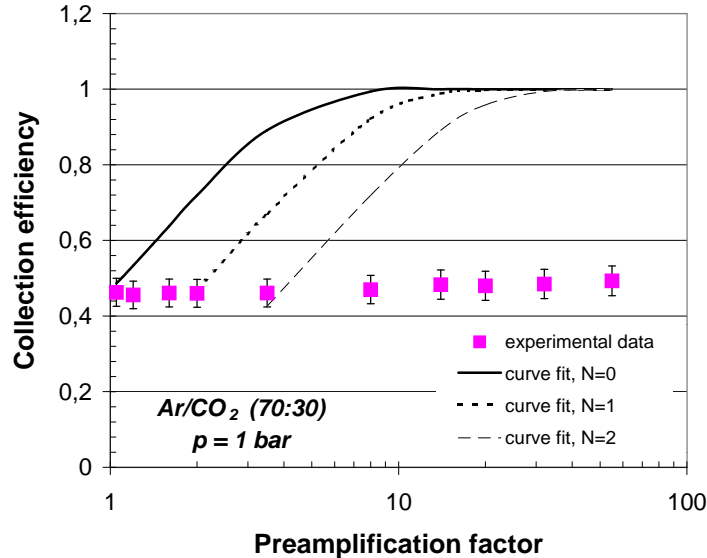
Figure 3.13: Absolute electron collection efficiency vs. preamplification, in Ar/CO_2 at atmospheric pressure. $U_{GEM} = 550$ V, corresponding to a GEM gain of 300, $E_{trans} = 1.5$ kV/cm. Due to the low diffusion of this gas, the best fit is N being very large. In other words, the diffusion is not sufficient to increase the collection efficiency when slightly preamplifying the primary electrons.

3.5   Summary

It was shown in this chapter, that a full collection efficiency for single electrons can be guaranteed also for applications, where large fields are required in the gas volume preceeding the GEM. The results can be summarized as follows:

- The collection efficiency for single electrons can be significantly increased, when E_{drift} is increased to values, where gas multiplication is induced in the drift gap. These secondary electrons, if moving independently in the gas, do significantly increase the probability to have at least one of them entering the GEM aperture. We have shown that this probability invariably reaches 100%, if the electrons transverse diffusion satisfies the condition that the lateral spread of the electron cloud exceeds the GEM-pitch. This spread depends on the transverse diffusion and thus on the gas properties and the drift length. If the condition is not satisfied, it is not possible to improve the efficiency by increasing E_{drift}. This principle is demonstrated in figures 3.11, 3.12 and 3.13.

- A simple statistical model successfully explained the results of collection efficiency under preamplification. It supports our understanding of the role played by the electron transport parameters, and particularly the diffusion.

- Monte Carlo simulations based on MAXWELL, MAGBOLTZ and GARFIELD software packages were found in good agreement with the experimental data.

It has to be emphasized here, that this procedure cannot be applied to GEM-detectors used in high rate hadronic beams. As explained in detail in chapter 5.4, the large number of highly ionizing particles would immediately lead to electric breakdowns between the GEM and the drift electrode. This method is highly efficient for all applications, where single electrons have to be detected very. In these conditions, the parallel-plate mode — even at high amplification factors — is a safe operation mode.

Part II

GEM-MSGC for High-Energy-Experiments

Chapter 4

The Hera-B-Experiment

In modern high energy experiments at hadron accelerators the requirements on tracking detectors are very demanding, especially with respect to the radiation hardness, longterm stability and spatial and temporal resolution attributes. In the following chapter, the development of GEM-MSGC detectors for the inner tracking system of the Hera-B-Experiment at DESY Hamburg is described in detail, elucidating the challenge and the difficulties in developing Micro Pattern Gas Detectors for high energy experiments.

A short survey of the Hera-B experiment, the detector and especially the tracking system is given first. The main issues are the experimental methods and the requirements for the tracking detectors.

4.1 The CP-Violation in the B-Meson-system

The Hera-B-Experiment is designed to measure the CP-violation in the B-meson system, where the CP violating effects are predicted to be large compared to the effects in e. g. the kaon system[1]. In the focus of interest is the so-called "gold-plated-channel", which provides a very clean measurement of the CP-violation:

$$B^0 \overline{B^0} \to J/\psi K_\mathrm{s}^0 \to l^+ l^- \pi^+ \pi^- \tag{4.1}$$

In this reaction, $l^{\pm}$ stands for an electron/positron or a myon pair of the J/ψ decay. This experiment uses the 920 GeV energy proton beam at DESY as a B-factory. With an interaction rate of 40 MHz (corresponding to an average of 4 interactions per bunch crossing), a branching ratio of $\sigma_{b\bar{b}} \approx 10^{-6}$ and roughly 10^7 s of data taking a year, up to 10^9 B-meson pairs can be produced in collisions with an internal wire target per year.

4.2 The Detector

At first sight, the Hera-B detector resembles a conventional forward spectrometer. The proton beam of the HERA electron-proton collider is directed on a fixed nucleus target. The carbon target fibers surround the beam core and are moved inside to scratch protons of the beam halo. Due to the excellent quality of the HERA-beam, also the outermost protons of the main

---

[1]The details concerning the CP violation in the standard model theory and the interplay between $B^0 - \overline{B^0}$ mixing and the CP-violation can be found elsewhere [57].

beam are scratched to provide the required 40 MHz interaction rate. However, this procedure allows Hera-B to operate without affecting or disturbing the other experiments located at the HERA-ring.

A side-view of the detector is shown in figure 4.1.
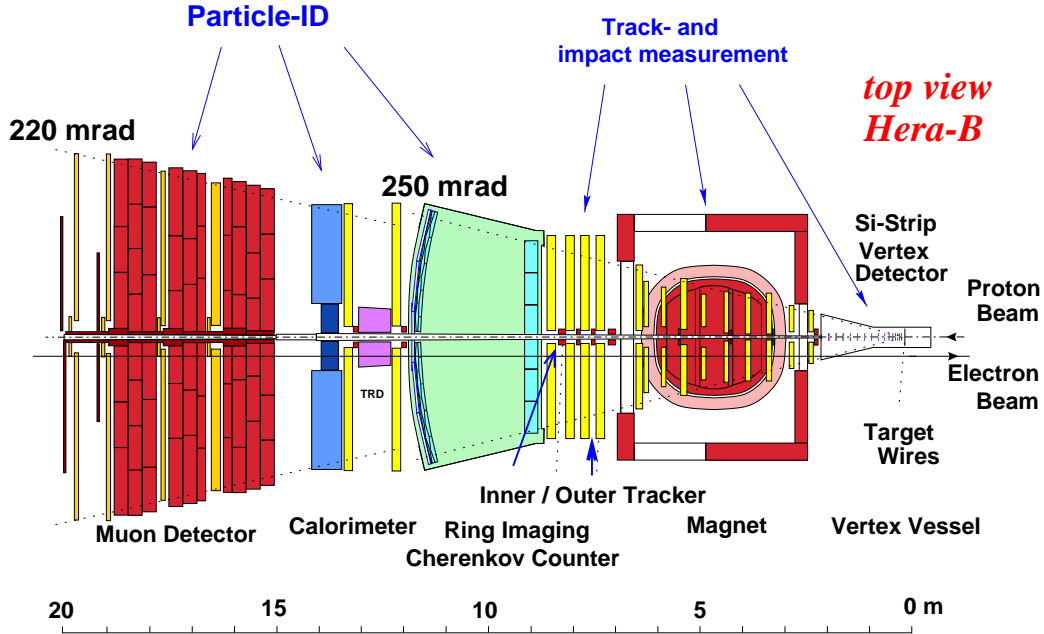
Figure 4.1: A top view of the Hera-B detector.

The precise reconstruction of multiple primary vertices and of a possible secondary vertex relies on the vertex detector system, consisting of seven super-layers of silicon strip detectors at 1 cm radius from the beam line. The 8 target wires and the vertex detector are placed in a vacuum tank, the vertex vessel.

For the momentum measurement, the tracks are bent horizontally by the field of a (warm) magnet of about 0.8 T. The detector acceptance in the bending plane of 250 mrad guarantees a large acceptance for the tracks from the "golden decay". The granularity of the tracking system varies with the distance off the beam, thus implying different techniques for different radial intervals; namely micro pattern detectors for the inner and drift tubes in a honeycomb structure for the outer parts. All trackers are grouped together in super-layers along the beam line and almost half of them are placed inside the magnet.

The particle identification in the Hera-B experiment is done by four different subsystems, the Ring Imaging Cherenkov Counter (RICH), the Transition Radiation Detector (TRD), the Electromagnetic Calorimeter (ECAL) and the Muon System.

The measurement of a significant 3σ effect of the CP-violation ("decay asymmetry") requires about 1000 golden decays. Given the low cross section for $b\bar{b}$ of only 10^{-6} and the very unfavorable branching ratio for the golden decays of 10^{-5} and finally an overall acceptance loss in the detector of 10 we have to dig out about one golden decay from 10^{12} events seen in the detector. This requires a very fast and efficient trigger system.

Furthermore, we expect a charged particle rate of roughly $10^5/R^2$ particles per mm^2 and second, where R is the perpendicular distance to the beam line measured in centimeter. Espe-

cially for the inner detector components this means a very high accumulated irradiation dose, almost exclusively caused by the overwhelming background particle rate in the experiment.

4.3 The Inner Tracking System

Due to the Lorentz boost, about half of all tracks of the golden decay pass through the inner tracking system, although the total covered area is small compared to e. g. the outer tracking system. The inner tracking detectors are installed in 10 different positions along the beam pipe, each of these so-called "super-layers" consists of several single layers and covers an area of 50 cm × 50 cm around the beam pipe. This corresponds to an angle of acceptance between 10 mrad and 100 mrad at maximum.

4.3.1 The requirements

The requirements for the inner tracker system are summarized below:

- The detectors have to withstand a particle flux of up to 2×10^4 particles/mm^{2}s. During the operation time of 3–5 years, the detectors are exposed to an irradiation dose of roughly 1 Mrad/a, which is orders of magnitude higher compared to tracking systems of existing experiments.

- The requirements for the granularity of the inner tracking system are demanding, since the occupancy should not be larger than 6% to ensure good track reconstruction — thus excluding the technique of multi-wire detectors or honeycomb drift tubes, as e. g. used for the outer tracking system. The high granularity is achieved by choosing a pitch of 300 micron. This value is sufficient to guarantee the required resolution of $x \leq 100$ μm in the magnetic bending plane, $y \leq 1$ mm and $z \leq 3$ mm along the beam pipe at the same time.

- Due to a bunch crossing frequency of 10 MHz and the necessity of a fast trigger decision (for details see [57, 58]), the signals and the readout of the detector have to be very fast ($t \approx 100$ ns).

- An efficiency of 96% for one single detector layer is required to provide a first-level-trigger efficiency not lower than 90%.

- Since a fraction of the detectors is operated in a magnetic field of $B = 0.8$ T, the full functionality must be guaranteed also in presence of magnetic fields. Thus, magnetic components cannot be used for the detector and for the support structures.

- In order to reduce multiple scattering, the material for the detector and the support structures has to be reduced to the lowest possible amount, nevertheless providing a sufficient mechanical robustness for assembly and transport.

4.3.2 Detector options

Given the required irradiation hardness and granularity, there are three possible options for a realization of the inner tracker system:

- **Scintillating Fibers**
  A detector consisting of scintillating fibers offers an acceptable spatial and time resolution. The operation is comparatively simple, since no gas or advanced high voltage system is required. However, due to the limited detector volume, the quantum efficiency of the scintillating fibers is mediocre. In addition, due to irradiation damages, the quantum efficiency is known to decrease significantly during operation in Hera-B [33, 59]. Besides the fact that this technology is still expensive, the problem of detector ageing was considered too severe for the Hera-B environment.

- **Silicon Strip detector**
  This type of detector is comparatively radiation hard (and is therefore used as the vertex detector in Hera-B). It provides an excellent spatial and time resolution. However, this technique was extremely expensive by the time of development of the Hera-B detector and since large areas have to be covered by the inner tracking system, this option was excluded because of the enormous costs.

- **Micro Strip Gas chambers (MSGC)**
  By the time of the first development steps of the inner tracking system for Hera-B, very detailed studies had already been performed at CERN in order to test, if this concept could be a reliable option for the high luminosity detector generation, e.g. the tracking system of the CMS and ATLAS experiments. It had already been shown in various tests in the laboratory, that MSGCs combine a very good spatial and time resolution for particle tracking and an excellent high rate capability [7]. When carefully avoiding outgasing material and when assembling them in very clean conditions, the lifetime of this detector can be more than one decade, even in high rate environment (c.f. section 6.1).

Based on these extremely promising results and the fact, that gas detectors are much cheaper compared to silicon detectors and scintillating fibers, the Hera-B collaboration declared the MSGC detectors to be the baseline line solution for the inner tracking system.

4.4   Development of GEM-MSGCs for Hera-B

Since the general operation principles of the MSGC and the GEM principle have already been explained in the introductory part of this thesis, only the characteristics concerning the development for the Hera-B experiment are reported in this section. The research and development of the full system was performed by the inner tracker collaboration of the universities of Heidelberg (D), Siegen (D) and Zürich (CH).

From the MSGC to the GEM-MSGC

Unfortunately, it turned out that MSGCs have many principle problems when operated in intense hadronic beam. Already in 1997 the Hera-B ITR-collaboration discovered that conventional MSGC detectors cannot be used in high-rate hadronic beams. Induced discharges in the vicinity of anodes and cathodes inevitably destroy the thin electrode strips within a few hours of operation. For the forseen Hera-B geometry with its almost 30 cm long strips, discharging turned out to be unavoidable, as described in detail in section 5.3.

After introducing the Gas Electron Multiplier (GEM) in 1997 as a second amplifying element, the probability for induced discharges in hadronic beams was reduced by orders of magnitude, allowing for a safe operation even in high rate beams.

The GEM-MSGCs for the ITR

Four L-shaped GEM-MSGC modules with dimension up to 30 cm × 30 cm constitute one ITR-layer around the beam, as shown in figure 4.2. The second coordinate for the track reconstruction is measured by " stereo layers", rotated with respect to the magnetic field. In order to reduce the combinatorial background, the rotation angles are small (5°). For an efficient trigger, the trigger super-layers consist of double layers for each rotation angle.

irradiation dose:
up to 25 kHz/mm

magnetic field
~0.8 T

resulution:
< 100 μm in x-direction
(in mangetic bending plane)
~ 1 mm y-direction
~ 3 mm z-direction
(along beam axis)

136 detectors in
8 super layers

beam
pipe

GEM-
MSGC

50-60 cm
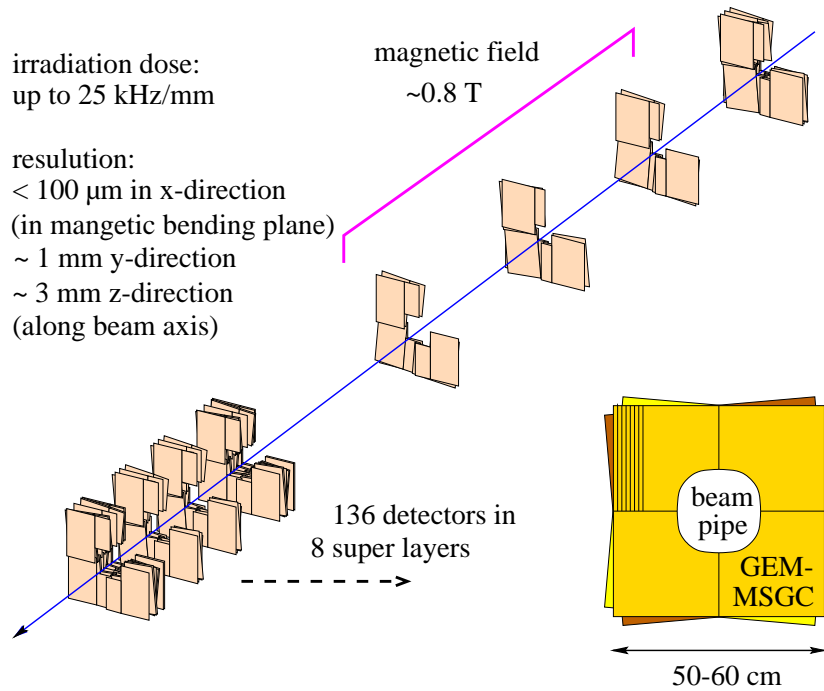
Figure 4.2: The MSGC arrangement around the beam [60]

A GEM-MSGC consists of four fundamental parts: the glass substrate with its micro strip electrodes, the GEM device, the drift lid and the frames for tightening the gas volume. During the research and development phase, all components were improved and optimized with regard to the demanding requirements of the Hera-B experiment. The description of the detector components, which were used for the main series production in 1999, are given below (see figure 4.3):

- **The MSGC**
  The substrate for the MSGC consists of 0.4 mm thick DESAG A54 glass. On top of the glass, a 80 nm thick layer of amorphous carbon ("diamond-like coating") with a surface resistivity of approximately $2 \times 10^{14} \Omega/\square$ is added by a chemical vapor deposition technique (CVD [61]). This extra layer prevents the glass surface from charging-up.
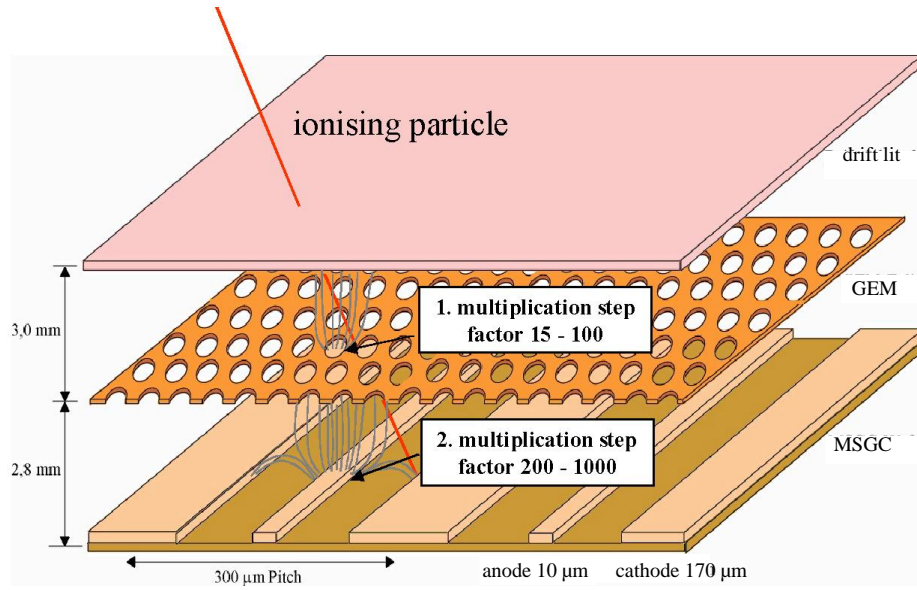
Figure 4.3: Schematic cross section of a GEM-MSGC as used in HERA-B.

In the next step of the production process the electrode structure is generated by a lift-off technique [62]. This micro pattern structure of 0.5 μm thickness consists of alternating 10 μm wide anodes and 170 μm wide cathode strips with a gap of 60 μm in between, as shown in figure 4.4. The resulting pitch is 300 μm. This value is small enough for a sufficiently low occupancy for the 40 MHz interaction rate in the Hera-B experiment.
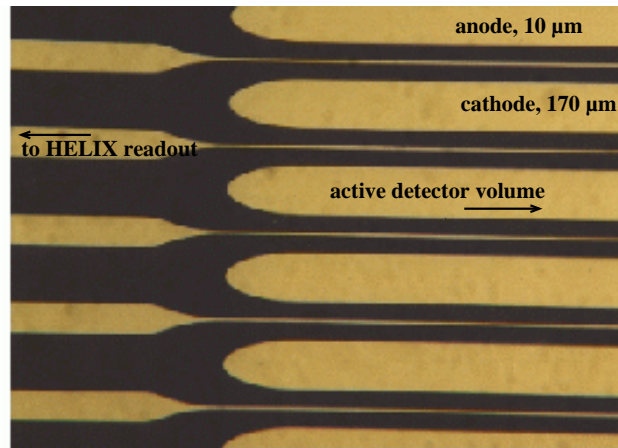
Figure 4.4: Top view on the electrode structure of the Hera-B MSGC at the anode end, showing the alternating 10 μm anode and 170 μm cathode gold strips with a gap of 60 μm in between.

The backside of the wafer is covered by an extra layer of colloidal graphite or thin silver (for the prototypes) or a thin self-glueing aluminum foil (for the main series

detectors). This so-called "backplane" provides a well defined electrical boundary plane for the signal propagation and for the electrostatic field configuration. In addition, it significantly reduces external pick-up noise.

- **The GEM**

  All main series detectors are equipped with an L-shaped "standard GEM" from the CERN workshop [31]. As all double etched GEMs (see section 1.2.5) it consists of a Kapton foil of 50 μm, covered with 7 μm copper layer on each side. Each Kapton aperture has a diameter of about 55 μm and the corresponding diameter for the copper layer is 95 μm. The holes are staggered with a pitch of 140 μm.

- **The drift lid**

  The detector lid consists of a 0.3 mm thick fiber glass epoxy laminate (G10 [63]), glued to a 100 μm single side copper-cladded Kapton foil. It serves as a drift electrode and as a gas-tight upper closing of the gas volume.

- **The frames**

  The distances between the electrodes are defined by the detector frames. In the Hera-B detector, the drift gap (distance between drift electrode and GEM) is 3 mm, the transfer gap (distance between GEM and MSGC) only 2.7 mm. Both, the drift and the transfer field are set to the same value of roughly 3 kV/cm, in order to reduce the electrostatic force on the GEM foil to a minimum value. This concept is necessary, since the Hera-B detectors are extremely large and the GEM foil is kept in position by mechanical tension only. We renounced on using spacers between MSGC, GEM and drift electrode, since the additional insulating material is prone for charging-up or discharging.

The gas amplification in the GEM-MSGC

In a MSGC, the gas gain G for a given geometry is determined by the field in the vicinity of the anodes. This is a superposition of the field between anodes and cathodes (a function of U_{cath}) and the drift field (a function of U_{drift}). As shown in figure 4.5, in the regime of normal operation the gain depends linearly on U_{drift} and exponentially on U_{cath}. For a given operation voltage U_{cath} and pitch, the gain decreases significantly for larger gap distances, as shown in the graph on the right.

In the combined system of MSGC and GEM, the GEM preamplification step has to be taken into consideration. As described in chapter 2, the *real GEM-gain* depends exponetially on the applied GEM voltage. However, for the total gain of a GEM-MSGC only the *effective GEM-gain* is relevant, which is given by the *real gain*, corrected for the transfer efficiency and the extraction efficiency.

For a desired total gain of about 8,000, the required cathode voltage is in the order of U_{cath} = 400–500 V, the GEM voltage is about U_{cath} =400–450 V and typical values for the drift voltage are a few thousand volts. Please note that these numbers correspond to the Hera-B geometry, operated in Ar/DME (50:50) at atmospheric pressure. However, the optimization of the operation voltages turned out to be an extremely difficult task, as described in detail in the following chapters.

With the Hera-B geometry we achieved an energy resolution for 5.9 keV X-ray up to 16 % in Ar/DME (50:50). The position accuracy in MSGC can reach up to 40 micron rms in absence of magnetic fields and for tracks perpendicular to the electrode plane. The Hera-B geometry is designed for an accuracy of 80 micron in the bending plane of the magnet.

.
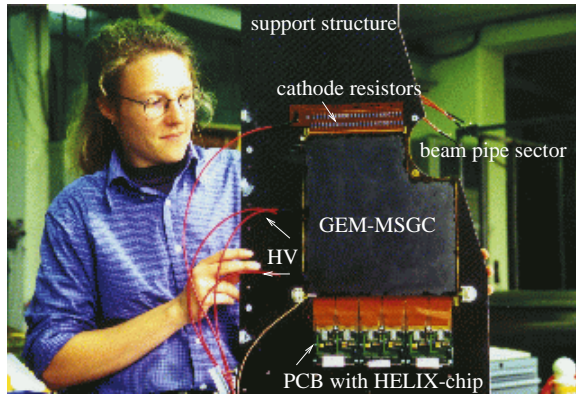
(a) A GEM-MSGC of the main series production, fully equipped (gas, HV and LV) and mounted on the support structure.
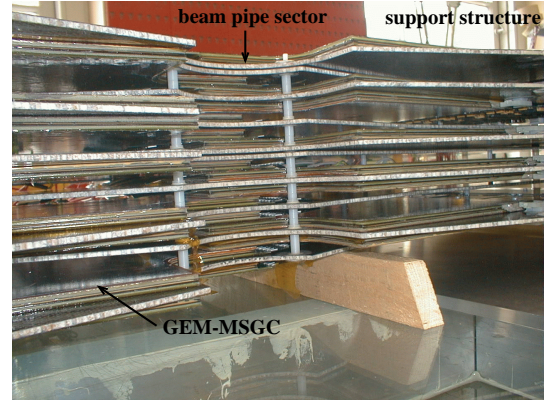
(b) Side-view of one half of a super-layer, consisting of two quadrants of GEM-MSGCs.

Figure 4.6: Pictures of the detector assembly.

an active control by a digital processor. This so-called "GEM-voltage-box" (A344) [67] is a multi-purpose device, as explained in detail in appendix A.

A mounted detector on its support structure is shown in figure 4.6.a. It is fully equipped with the electronics, the gas in- and outlets and all high and low voltage cables as well as the readout cables. A bunch of 8 detectors is depicted in figure 4.6.b., representing one half-station of the inner tracker system in Hera-B.

Chapter 5

Discharge Phenomena in GEM-MSGCs

For any gaseous particle detector, it is of vital importance to provide a sufficiently wide regime of voltages where stable gas amplification is possible. The upper limit of this regime is usually defined by the onset of uncontrolled electrical discharges which can be after pulses, self sustaining dark currents (so called Malter currents), glow discharges or sparks. All of them are accompanied by currents much larger than the currents of normal operation and are of potential danger for the read out electronics and the detector itself. In Micro Strip Gas Chambers, or in other detectors using micro pattern electrodes, these uncontrolled currents are of special danger due to the fragility and delicacy of the electrodes and read out patterns.

5.1   Discharge Criterion

In 1964 Raether [68] formulated a criterion for the transition of a controlled avalanche into a streamer, initiating a breakthrough of the insulating gas gap. The basic argument is that if the electric field created by the avalanche itself reaches a value comparable to the external field (which by definition is sufficient to allow for gas amplification), the avalanche process enters an "autonomous" regime since the field just in front (and behind) the avalanche is enhanced by the growing space charge. For a qualitative estimate Raether assumed (see also introduction) that the electrons in the avalanche can be described as a swarm in equilibrium with the gas and the external field, that means it can be described by the first order transport coefficients drift velocity v_e, diffusion coefficient σ and the 1. Townsend coefficient α. As function of the drift distance d in a homogeneous field, the diffusional width σ of the a Gaussian charge cloud increases according to

$$\sigma^2 = \frac{2d\varepsilon}{E} \tag{5.1}$$

with ϵ being the mean thermal energy of the electrons and E the external electric field. The total number of electrons n_e in the cloud increases as

$$n_e = n_0 \exp(\alpha d) = n_0 g(d) \tag{5.2}$$

with $g(d)$ being the gain after traveling the distance d and n_0 the primary number of electrons. If we approximate this swarm by a sphere of radius σ and require the field at this radius to be

equal to the external field, we arrive at Raether's criterion for streamer formation in general form :

$$n_0 \, g(d) > \frac{8\pi\epsilon\epsilon_0 d}{e} \tag{5.3}$$

Replacing the numerical constants, we end up with

$$n_0 \, g(d) > 1.3 \times 10^{10} d \tag{5.4}$$

for the total number of electrons fulfilling the streamer criterion produced over the distance d given in meters. If we assume 50 μm as typical anode-cathode gap width, it goes down to about 7×10^5 electrons for $n_0 \, g(d)$. An α-particle of 1 MeV produces about 10 electron-ion pairs per μm in the counting gas, resulting in a critical gas gain in homogeneous fields of about 1500 (independent of the gap width) leading to charge densities fulfilling the streamer criterion. But only if the streamer has a chance to reach both electrodes, meaning the amplification gap is not separated by a regime of a sufficiently low electric field from the cathode and/or the anode, a discharge will be initiated. Despite the fact that Raether's criterion is a very rough estimate and absolute numbers should be taken with care, it explains why micro pattern detectors are especially prone to induced discharges: the gas amplification is produced over small distances in almost homogeneous fields and thus even a moderate gain leads to streamer formation for sufficiently high primary ionization.

5.2   Discharges in Hera-B Conditions

In order to avoid discharges during operation in the high rate beam at Hera-B (and thus severe destructions of the fragile electrodes), the discharge phenomena were studied carefully. The problem of uncontrolled discharges, as described in the previous section, occurred twice during our research and development phase.

First, the phenomenon of *anode-cathode discharges* was discovered when testing Micro Strip Gas Chambers in high rate beams. This type of discharge is restricted to the MSGC amplification step only and will be described in detail in section 5.3. The outcome of this study was that these discharges reflect a fundamental problem of the MSGC principle at high gain and have nothing to do with improper choice of operating conditions, materials or counting gases. By combining a MSGC with a GEM as a preamplification structure, the amplification factor for the MSGC step could be significantly reduced. As a result, the discharge probability decreased by orders of magnitude, since the total amplification was separated into two non-critical steps.

However, a second, even more disastrous type of discharge was discovered and investigated for the first time during this work: the propagation of discharges from the GEM towards the MSGC, leading to fatal damages in the MSGC structure. It is presented in section 5.4, that in the combined system discharges can only be completely excluded, if both regions of amplification are decoupled by a region of sufficiently low field.

5.3   Anode-Cathode Discharges[1]

Until spring 1996, the base line solution for the HERA-B Inner Tracker was a conventional Micro Strip Gas Chamber with diamond like surface coating (DLC) and Ar/DME (50:50) as

---

[1]Parts of this section are extracted from our paper [69]

counting gas. In various experiments with X-rays using small test chambers as well as full size prototypes, it was demonstrated that MSGC detectors offer excellent high rate capabilities up to 10^6 mm^{-2}s^{-1} with stable gas gains above 5000.

5.3.1   Induced discharges

A severe set back came in April 1996 when a first set of full size chambers was tested in the high intensity pion and proton beam at the Paul Scherrer Institut in Switzerland (PSI) and the phenomenon of induced discharges was discovered [70, 71]. When operating them at pion rates of some 10^3 mm^{-2}s^{-1} and a gas gain of 3000, the chambers suffered from anode-cathode discharges at a rate of one per few minutes, a phenomenon which was never observed in identical chambers with X-rays even at 100 times higher intensities. After few hours of operation, anodes and cathodes in the irradiated area were scattered with marks, some anodes were even completely disrupted.

Taking into account the Raether law for the discharge process, the presence of heavy ionizing particles in a high intensity pion beam was assumed to initiate the discharge process. The presence of heavy ionizing particles in the hadron beam is not surprising and can be easily explained as nuclear fragments from reactions with the materials of the MSGC itself. Following the discovery at PSI, we installed a set of test chambers at the original place in the HERA-B experiment. At nominal conditions of interaction rate and chamber settings, the detectors showed a discharge rate of several Hz, leading to severe damage of the chambers after a few hours of operation.

In the following, a variety of experiments was carried out to understand the nature of the phenomenon and to find possible remedies by changing constructional details or operating conditions of the chambers [72]. Resulting from these tests it had to be concluded that induced discharges are a general problem of all kinds of micro pattern detectors, reflecting the fact that anodes and cathodes are spatially close together and not separated by a regime of low electric fields. The base of this conclusion are the following observations and measurements.

5.3.2   Experimental Set-up in the Lab

The suspicion that these destructions observed at the PSI beam are a consequence of discharges induced by heavy ionizing particles could be easily verified in the lab using a gaseous source of MeV α-particles. Since the construction of the chambers did not allow penetration of heavy ionizing particles from outside, we introduced a stainless steel box containing natural Thorium oxide to the gas inlet. One of the daughter products of ^{232}Thorium is ^{220}Radon, a noble gas decaying with a life time of 55 s with the emission of 6.3 MeV α-particles. With a few grams of Thorium oxide a counting rate of alpha particles of about $1s^{-1}$ could be achieved. The α- emitting gas immediately initiated anode-cathode discharges with the same fatal consequences previously observed in the pion beam. This offered the opportunity to study the phenomenon in great detail in the lab without being bound to the cumbersome environment of an accelerator facility.

5.3.3   Experimental Results

Influence of the electric potentials

At the normal operating point, the gain typically depends linearly on U_{drift} and roughly exponentially on U_{cath}. If the probability of induced discharges had a much steeper dependence on one or both, or even show a typical threshold behavior, it should be possible to change the operating conditions into a safe regime. As shown in figure 5.1 the discharge rate is completely independent of U_{drift} as long as U_{cath} is kept constant. This statement is valid even in the case

geometry and strength of the electric field between anodes and cathodes. To compare both, a two-dimensional electrostatic calculations with and without conductive surface layers [73] was performed. While the calculations with surface conductivity can be considered as very close to reality, the uncoated case has some intrinsic uncertainties. As an approximation, a homogeneous bulk resistivity of the glass was used, keeping in mind that for a real uncoated glass surface the field distribution is affected by the distribution of ions which can be highly non uniform. In figure 5.7, we show for both cases the strength of the electric field for various heights above the MSGC surface, ranging from 1–100 μm.
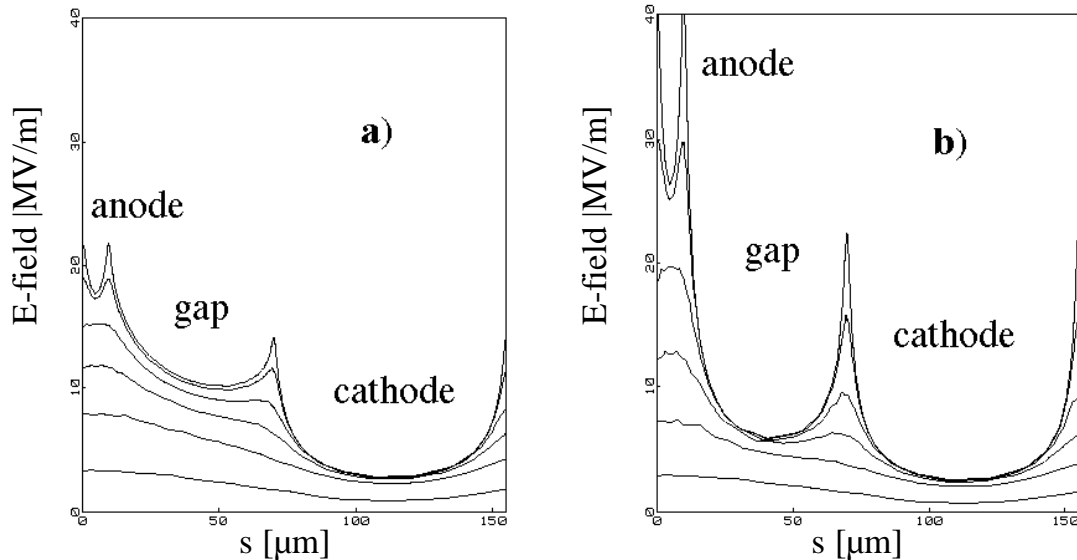
Figure 5.7: Electric field close to MSGC surface, a) coated plate, b) uncoated plate. The curve refer to lines parallel to the MSGC surface in heights of 1, 2, 5, 10, 20 and 50 μm

For the uncoated plate, the field falls off quite rapidly from both the anode and the cathode edges, resulting in a strong field reduction in the anode cathode gap. In contrast to this, the fields on the coated plate are much more homogeneous, the edge fields are reduced (one of the benefits of the surface coating) and the field reduction in the gap is much less pronounced. For distances of more than about 100 μm from the surface, the coated and the uncoated plate have almost identical electric fields. The fact that uncoated plates, despite their much more pronounced edge fields, show smaller spark rates than coated plates for the same gas gain, is evidence that the edge fields can not be of major importance for the proneness of the device to develop this kind of uncontrolled discharge. If we combine the field pattern with the previously demonstrated finding that only strong ionization very close to the surface bear the possibility to induce discharges, we come to the conclusion that the relatively high fields in the anode-cathode gap (which are parallel to the MSGC surface) are the weak point of the MSGC geometry and the mediator of the induced discharges. From this picture it can be understood why the drift field has no influence on the discharge rate and why for gases with similar quenching properties the ratio of gas gain and discharge rate is an invariant: the electric field above the anode (defining the gas gain) and the field in the anode-cathode gap (defining the discharge rate) are strictly correlated by the cathode voltage and only defined by the geometry of the chamber.

Influence of the strip material

The material of the MSGC electrodes (strips) affects the process of induced discharges in various ways. First of all, it might be possible that the discharge is growing by some feedback mechanism from the electrodes, especially by field emission or ion or photon induced secondary emission from the cathodes. In this case the specific nature of the electrodes could be of great influence on the discharge probability. Secondly, the discharge is powered by the electric current through the strips and the finite resistivity of the typically less than one μm thin strips defines the time scale of power input to the discharge. Last but not least, if the discharge process cannot be completely avoided, the strip material should be as robust as possible, since the strips are subject to destruction.

Chromium strips (either sputtered or evaporated) turned out to tolerate orders of magnitude more sparks before suffering from severe damage than for instance the very weak gold strips of our preferred chamber design [74]. It was, however, not clear if this is a consequence of the higher strip resistivity and thus limited current in the discharge or by the much superior mechanical properties of the hard chromium compared to the weak and susceptible gold. Good candidates to disentangle both properties are rhodium and tungsten, materials combining reasonable conductivity with excellent mechanical strength. Unfortunately it turned out to be purely the electrical conductivity that defines the robustness of the strips against discharge erosion. Rhodium and even tungsten show different but not less severe damage patterns than gold. Solely chromium, with its high intrinsic resistivity, proved to be much more robust but in parallel reduces the signal speed in an intolerable way for strips longer than several centimeters. However, in Hera-B up to 30 cm long strips are required.

We finally had to conclude that the strip material is not the appropriate parameter to turn a conventional MSGC into a non-sparking or spark resistant device.

5.3.4 Conclusions

The discharge problem turned out to be an intrinsic problem of the micro pattern detector principle, the actual shape of the amplification gap (groove, well, gap) and its boundaries (material, edge field) should be of minor importance.

The small distance of anodes and cathodes together with the field shaping surface coating neglects one of the fundamental requirements for gaseous detectors, namely that anodes and cathodes should be separated by a region of sufficiently low field, preventing any propagation of streamers between the two electrodes which finally result in a fatal discharge of the electrode system. If the fields in the gap are not below the threshold for gas amplification, it is only a question of the strength of the initial ionization whether a streamer and finally a discharge is triggered. Furthermore any kind of micro pattern detector can and will have similar problems if the rule of low field separation of electrodes is violated.

5.4 Multiple-Electrode-Sparks

Due to the problem of the anode-cathode discharges in conventional MSGCs, a combination of a Gas Electron Multiplier (GEM) as preamplifier with a MSGC plate as detecting element (with a second amplifying step) is now used for the inner tracking system of the Hera-B experiment, as explained in chapter 4. The basic advantage of this approach is to factorize

the total gain into two independent steps of sufficiently small gain in order avoid induced discharges, as shown in figure 5.8
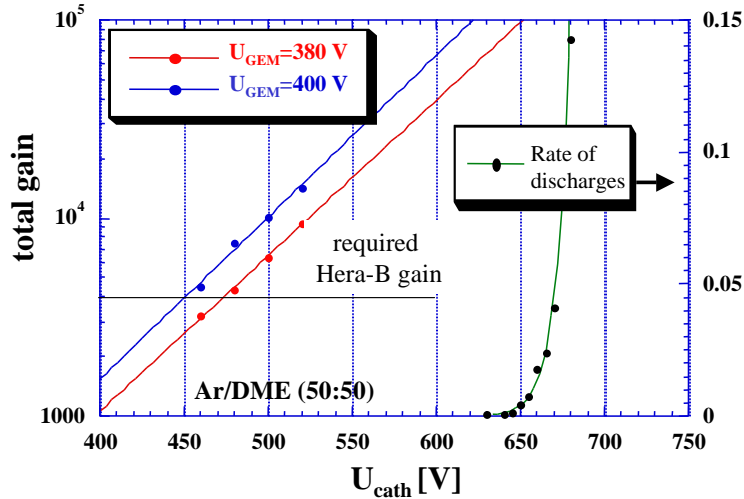
Figure 5.8: The total gain and the spark rate in a GEM-MSGC as a function of the cathode voltage. A gain of roughly 4000 is required for the Hera-B operation. By separating the amplification into two steps of sufficiently low gain, the rate of anode-cathode discharges can be reduced by orders of magnitude.

Nevertheless, within this work another type of discharge process was discovered in the GEM-MSGC combination [75]. The phenomenon of combined discharges, first observed in the pion and proton PSI-beam during a test of Hera-B prototypes, appeared as sudden spikes in the detector currents. Besides, during an optical inspection massive destructions were found on the MSGC-substrate.
These discharges are clearly different from anode-cathode discharges (c. f. section 5.3):

- The damage of a single discharge to the fragile electrode structure is much more destructive. We found spots of destruction of the size of $\approx 100\mu$m. One single discharge can not only completely destroy the anode strip, furthermore the adjacent cathodes show marks of destruction in shape of a half-moon (see also figure 5.9). In some rare cases *several* anodes and cathodes were destroyed simultaneously.

- As a consequence of those discharges, the resistivity between anodes and cathodes was often found to be *reduced* by orders of magnitude, sometimes even resulting in an electric short between anode-cathode shorts. This suggests, that much more energy is released during this kind of discharge, since this effect was never observed in connection with anode-cathode sparks. It entailed, that the whole cathode group (16 strips) could not be used any more after the incident.

- The discharge is not restricted to the anodes and cathodes. We observed simultaneous spikes in the monitored currents in the GEM and the drift electrode as well, clearly showing that all other electrodes are involved.
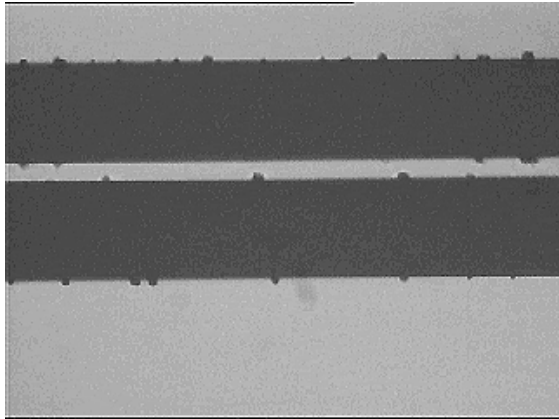
(a) Anode-cathode spark: small "mouse bites"
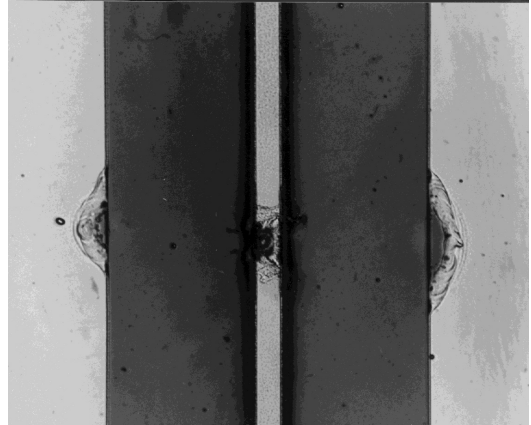
(b) Multiple-Electrode-Spark: large destruction including the adjacent cathode strips

Figure 5.9: Destruction after different discharge types (small light strips: anodes, big light strips: cathodes)

- Different to the process of anode-cathode discharges, the cathode voltage has no influence on the discharge tendency. Moreover, in the operation conditions and voltage regime where the detectors were operated during the PSI-beam test, the probability for the occurrence of anode-cathode discharges is expected to be extremely low. However, several discharges have been observed.

Since all electrodes are involved in the discharge process, this type of discharge was called "multiple-electrode-spark" (MES). First tests proved, that these combined discharges are always induced by GEM-sparks, e. g. discharges between the upper and the lower side of the GEM.

5.4.1   Experimental Set-up

A detailed examination of this new discharge phenomenon was performed in the laboratory, using full-size Hera-B-prototypes. Here, all operation conditions can be chosen freely, giving the opportunity to investigate the relevant parameters.

Spark detection

All electrodes (drift, GEM_{upper}, GEM_{lower} and cathode) were equipped with pick-up electrodes (see electrical circuit diagram in figure 5.10) in order to investigate the process of the discharge; the potential variations during the discharge process were monitored with a time resolution better than 100 ns. In addition, a quantitative analysis of the potential shifts of each electrode was done off-line. For a reduction of the large voltage jumps (dU $\approx$ 1000 V) the pick-up electrodes were designed to reduce the signals by a factor of 100 (= capacitive voltage divider 47 pF : 4,7 nF, see figure).
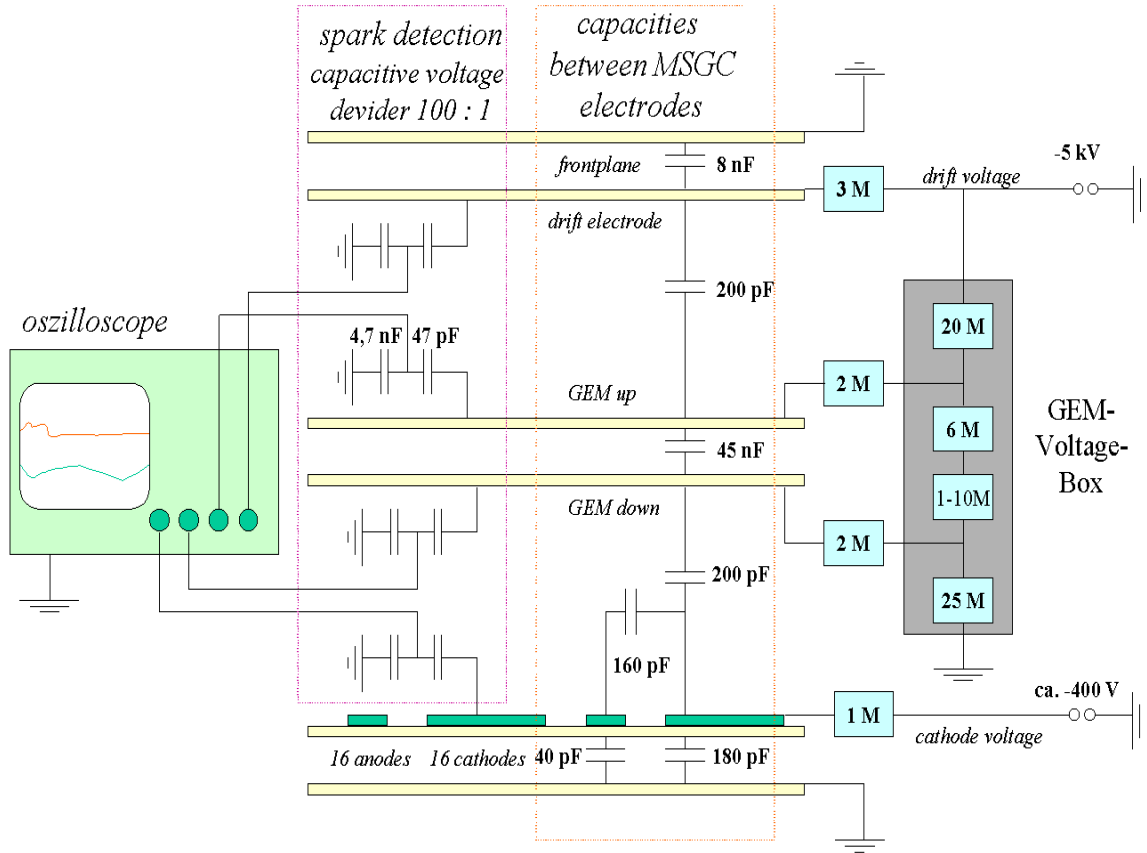
Figure 5.10: Circuit diagram for a Hera-B GEM-MSGC, the pick-up electrodes and for the GEM-Voltage-Box. The pick-up electrode for each detector electrode is represented by a capacitive voltage divider (47 pF : 4,7 nF), connected to a 4 channel digital oscilloscope for the readout.

The GEM-MSGC

The GEM-MSGC used for this study was identical to a main-series chamber, however it was not equipped with the HELIX read-out system. Instead, all anodes were directly connected to ground. Concerning the impedance of the system, this is very close to the real conditions.

The capacities of all electrodes of the original system were measured (given in figure 5.10). The total capacity of the drift and both GEM-electrodes is in the regime of $C_{\text{drift}} = 10$ nF and $C_{\text{GEM}} = 50$ nF respectively, meaning that the additional capacity of the capacitive voltage divider plays a minor role.

The situation for one cathode group is slightly different, as the total capacitance is in the order of the additional capacitance of the pick-up electrodes. Hence, in this set-up we renounced the backplane (which is only relevant for the signal-propagation process) and replaced it by the spark-detection, ending up with a similar total cathode capacitance, compared to the "original" system.

For this study, a detector was used, where the GEM-spark tendency — by chance — was high and where, in addition, the GEM-sparks were restricted to a few GEM-holes in a fixed area. This behavior was extremely helpful for the cathode spark-detection, as we only had to connect those 16 strips of one cathode group to the spark-detection, which were closest to the sparking region. In addition, both adjacent cathode groups were connected to the spark detection, in order to control how many strips are involved in the discharge process and thus to estimate the size of the involved area. In general, the discharge process is restricted to one single cathode group.

All measurements in this chapter were done in Ar/DME (50:50) at atmospheric pressure. Starting from $U_{GEM} \approx 400$ V first single GEM-sparks were observed. Due to the missing backplane layer those discharges were also observed visually.

5.4.2   The MES process

Multiple electrode sparks (MES) are *always* induced by a preceding GEM-spark. After an inclination time of 1 to 10 microseconds, the discharge process expands to all other electrodes, resulting in a complete breakdown of all detector potentials.

In figure 5.11, a typical oscilloscope shot of the discharge process is given. Due to the capacitive coupling all potentials are AC and not DC, thus only potential shifts and jumps can be observed. Please note that the discharge process is not influenced by effects of recharging, since the power supplies are all separated from the detector electrodes by resistors of several MΩ. The corresponding time constant ($\tau = R \cdot C$) is in the order of seconds. The general development in time of the absolute value of the drift, GEM- and cathode potentials is shown in a sketch in figure 5.12.
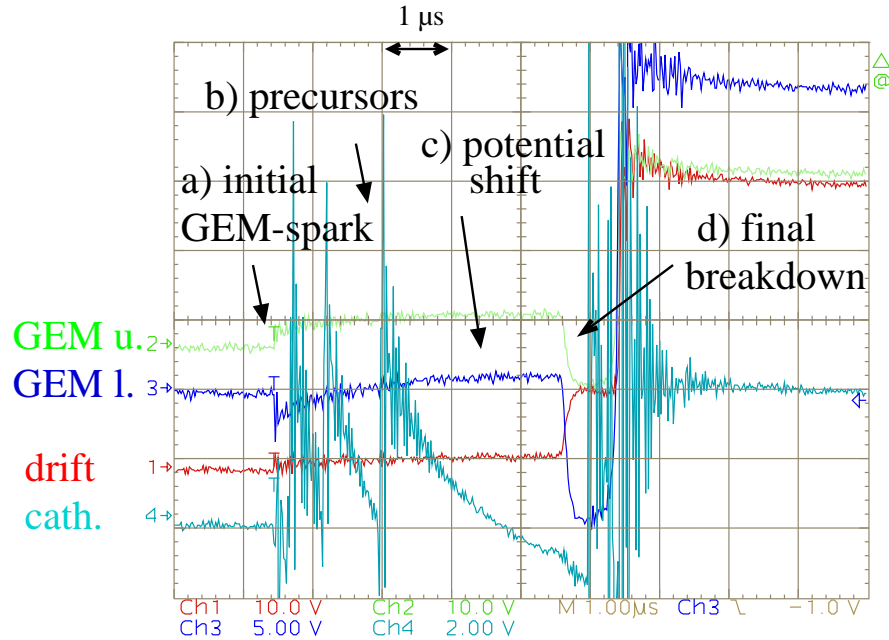
Figure 5.11: Oscilloscope shot of initial GEM-spark, precursors, potential shift and final total breakdown. ($U_{drift} = 5$ kV, $U_{GEMupper} = 2.9$ kV, $U_{GEMlower} = 2.5$ kV and $U_{cath} = 465$ V)
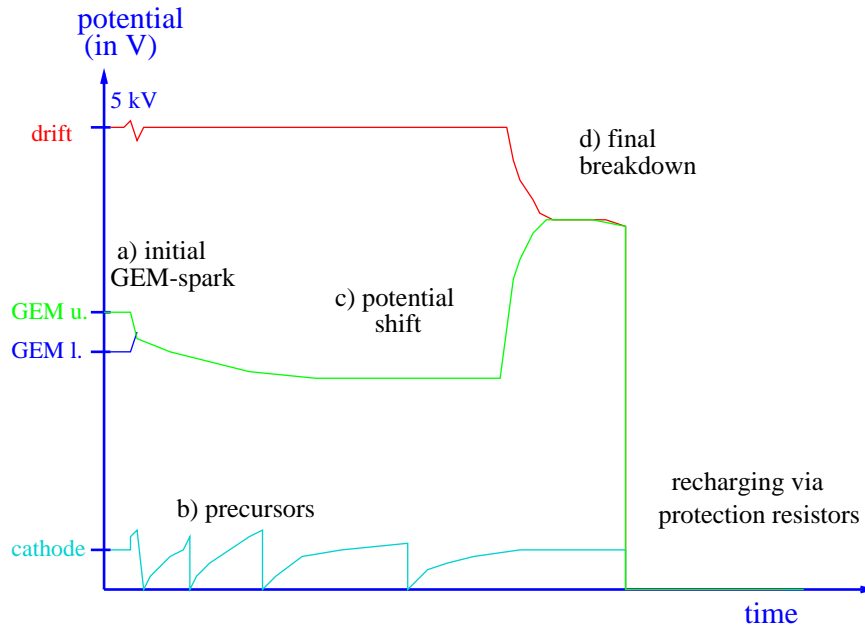
Figure 5.12: Visualization of the development in time for the potentials during a "multiple electrode spark". The discharge process can be divided into 4 parts: a) initial GEM-spark, b) precursors, c) potential shift and d) final total breakdown. The last breakdown is either between drift and GEM-electrode first and then, as a consequence, between GEM and the MSGC potentials (as depicted here) or vice-versa.

The MES-process is a complex series of single steps and can be divided into four main parts:

a) The initial GEM-Spark

The oscilloscope was set to trigger at the instant of the initial GEM-spark. The absolute voltage drop in the GEM_{upper} and the GEM_{lower} potential is almost of identical magnitude and adds up to 400 V, exactly matching the applied GEM voltage. As a consequence of this discharge process, the GEM-capacity is completely discharged ($Q = R \times C = 45\,\text{nF} \times 400\,\text{V} = 18\,\mu C$) and a big amount of charge ($\approx 10^{14}$ electrons) is released. Since the GEM gain drops exponentially with respect to the applied GEM-voltage, the amplification process is quenched rapidly during the discharge process. Due to the altered field conditions close to the GEM ($U_{GEM} = 0\,\text{V}$), the charge can be efficiently extracted from the GEM lower side, and thus, a huge amount of electrons and ions is drifted towards the anodes or the drift electrode respectively.

The drift time of electrons from the GEM towards the anodes in the Hera-B conditions is in the order of 60 ns ($v_{\text{drift}} \approx 5\ \text{cm}/\mu s$). This value is mainly determined by gas type, pressure, detector geometry and field strength. In contrast, the positive ions reach the drift electrode after approximately 20 μs, since their drift velocity is significantly smaller. Taking into account the drift velocities, the spike in the drift potential at $t = 0$ s cannot originate in charge collection from the drifting ions, instead it is caused by the capacitive coupling. It should be noted here that the whole MES-process is electron driven, since the drifting time for the ions is too long to induce the relevant processes, such as e. g. ion feedback.

b) Precursors between Anodes and Cathodes

The number of electrons, drifting towards the anode, is much larger compared to normal signals, and thus the situation in the region of the MSGC electrodes completely changes.

As depicted in figure 5.11, the cathode potential temporarily becomes more negative, than the applied negative voltage. Due to a huge amount of charge, not all electrons drift towards the anode; instead, a fraction is spread on the cathodes as well. In contrast to the anodes, the cathodes are not directly coupled to ground but with 1 MΩ per group. Consequently, this electrode charges up and thus the potential shifts towards even more negative values. This however increases the probability of anode-cathode discharges dramatically (see section 5.3). A very dense ionization in the vicinity of anodes and cathodes (caused by the GEM-electrons on one hand and newly created ions on the other) additionally increases the spark tendency and as a consequence, discharges between anodes and cathodes ("precursors") can be observed very shortly after the initial GEM spark. The typical "mouse bites" on the electrode strips are a consequence. The positive peaks, clearly detectable on the cathode potential, are found to occur several times (up to N $\approx$ 10) after the initial GEM-spark and correspond to typically 450 V, well matching the applied cathode voltage.

The amount of charge spread on the cathode can significantly be influenced by the applied cathode voltage U_{cath}. In figure 5.13 U_{cath} was set to 10 V. As a result, a larger fraction of electrons ends at the cathode, resulting in a pronounced shift of the cathode potential towards very negative voltages. However, the general process of the complete breakdown is unaffected by a variation of the cathode voltage.
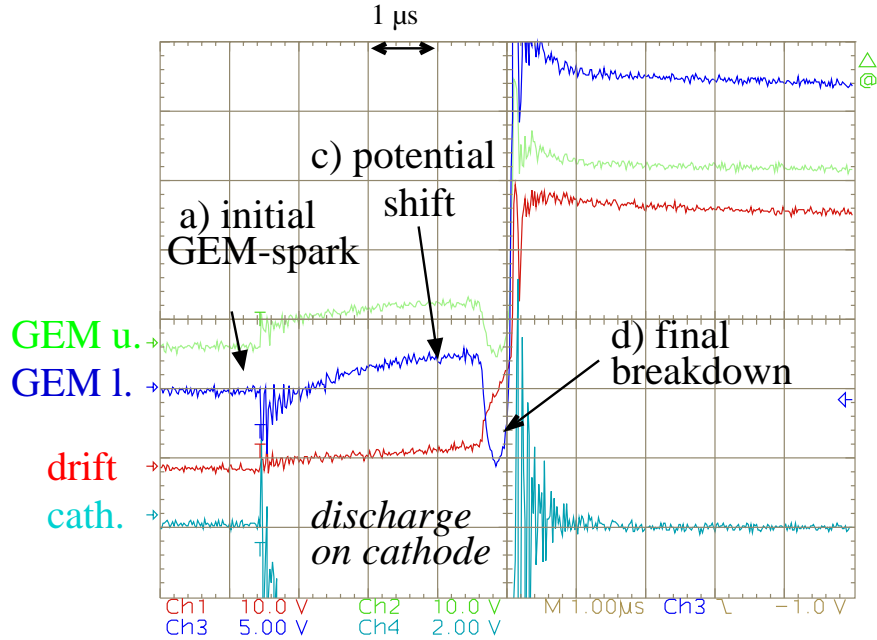
Figure 5.13: MES for U(cath)=10V, discharge ends on cathode, very negative cathode potential

c) Potential Shift between GEM-spark and MES

Precursors were detected not only as a consequence of the initial GEM-spark. The process rather continues for several microseconds. Hence, we may conclude, that electrons are not only extracted from the GEM in the initial GEM-spark but rather continously released, thus permanently feeding the discharge process at the MSGC substrate. This theory is strongly supported by the fact, that both GEM-potentials drift towards more positive values, as it can be observed e.g. in figure 5.13. The physical process can be described by a creation of streamers in the gap between GEM and MSGC. Taking into account, that the potential shifts by several hundred volts within microseconds, a rough estimation demonstrates, that large currents are obtained between the initial GEM-spark and the final breakdown:

$$I = \frac{Q}{t} = \frac{(C \cdot U)}{t} = \frac{(500\,V \cdot 200\,pF)}{5\,\mu s} = 20\,mA \tag{5.5}$$

Since the voltage between the GEM and the MSGC is $U \approx 2000\,V$, the resulting power is of the order of $P = 40\,W$, large enough to feed the streamer and to further heat the gas.

d) Final Total Breakdown

Resulting from the charge release from the GEM, the charge density in the transfer-gap increases significantly during the MES-process; in addition, ions created in the final multiplication step, slowly drift back towards the GEM. As a consequence, in the last stage of the MES-process, a discharge between GEM and MSGC, or — less likely — between GEM and drift-electrode initiates the final breakdown of all detector potentials. In figure 5.11, it is reflected by a sudden potential shift of both GEM-potentials (in parallel) and the drift or respectively the MSGC-potential (opposite direction). The breakdown entails, that the field strength on the non-involved side of the GEM dramatically increases, thus provoking a collapse between the GEM and the other electrode. As a consequence of the total discharge, each detector potential is grounded. After the typical recharging time, the potentials recover and the whole process can start again, when induced by a GEM-spark.

5.4.3   Reduction of Precursors

An effective way to avoid the precursors is to prevent the cathodes from charging up. Therefore, an additional high-voltage diode (see figure 5.14) was connected in parallel to the 1 MΩ-resistor of each cathode group. In case of anode-cathode shorts it has to withstand a voltage difference of approximately 500 V. In addition, this diode was chosen to be extremely fast-switching, which was required because of a very short charging up time. As a result, the charge arriving from the transfer gap can pass the diode and the additional capacitance of the HV-cable prevents the cathode potential from shifting to very negative values.

The effectiveness of this new circuit element was tested in the lab and it was found to be very successful. Figure 5.15 demonstrates, that no precursors occur when diodes are used. The cathode potential after the GEM-spark is extremely stable.

Nevertheless it has to be emphasized, that the streamer propagation from the GEM to the MSGC *cannot* be influenced by the diodes, since the cathode potential as well as the process of anode-cathode discharges is irrelevant for the final breakdown. This effect corroborates that the whole MES-process must be electron driven. The ion-feedback from the secondary discharges between anodes and cathodes is too slow to further heat the process at the GEM-foil.
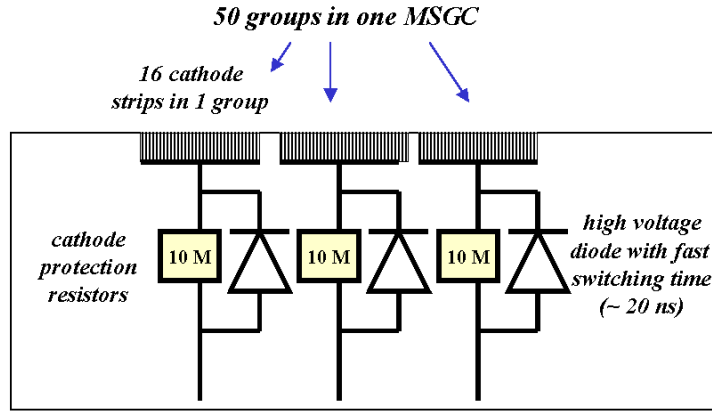
Figure 5.14: Connection diagram for cathode protection against precursors.
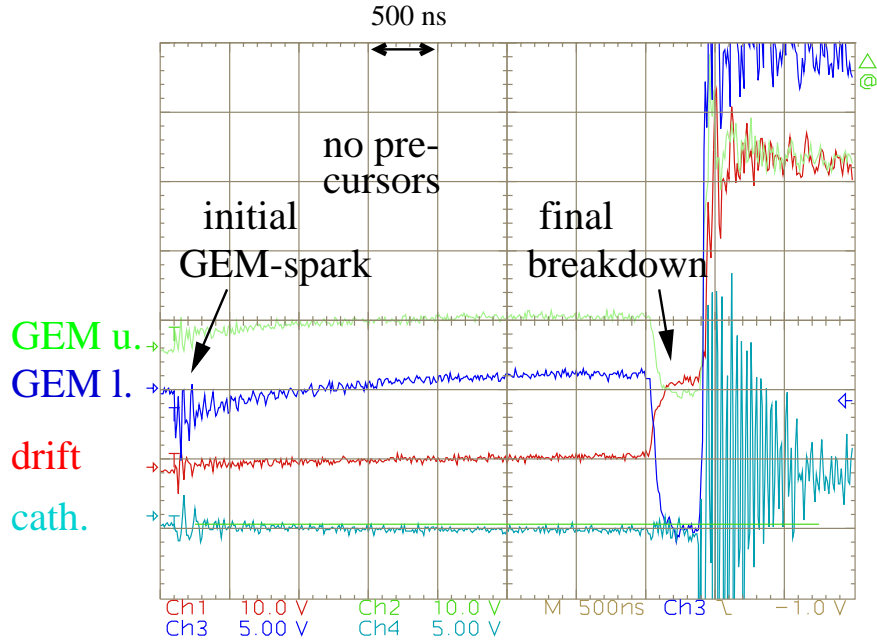
Figure 5.15: Effect with protection diodes: no precursors, but still final discharge.

5.4.4   The MES rate N_{MES}

A GEM-spark is a necessary but not sufficient condition for a combined discharge. The rate of MES (N_{MES}) is therefore given by:

$$N_{\mathrm{MES}} = N_{\mathrm{GEM}} \times P_{\mathrm{MES}} \tag{5.6}$$

with N_{GEM} being the GEM-spark rate and P_{MES} being the probability that the initial GEM-spark turns into a MES. In order to reduce the number of MES, both parameters were carefully studied.

GEM-spark tendency $N_{\mathbf{GEM}}$

GEM-discharges are in general not critical for the detector, as GEMs are very robust devices. From previous beam-tests and from studies with X-ray irradiation we observed, that GEM-sparks can be induced by several reasons:

- **defects in the production process**
  Limitations in the operation mainly originate from the quality of the foils. The shape of the holes may vary due to irregularities in the manufacturing process of GEMs, e. g. defects in the mask, dust during light exposure or other problems during the etching process. The worst case for GEM-sparks are copper etches or tips, looming inside the GEM holes.

- **sudden increase in GEM-voltage**
  While increasing the GEM-voltages, the field inside the holes change dramatically. Very sudden changes in the voltage settings often induce GEM-sparks. The most probable reasons for this effect are charging-up and polarization effects in the Kapton insulator.

- **sudden changes in irradiation rate**
  Especially in beam tests we observed, that GEMs often tend to spark, when the beam rate was changed or the beam was moved out of the active detector area. In this case, the detector currents change very fast and, hence, also the field in the GEM. This effect also leads to an increased spark tendency.

Most of the parameters mentioned above cannot be influenced, as e. g. beam-rate instabilities can not be completely excluded in the Hera-B-beam. In addition, all 200 GEMs required for Hera-B are individuals and defects in the production process can neither be excluded, although all GEMs were carefully tested prior to assembly. We believe that the GEM-spark probability cannot be reduced to zero and therefore the main approach to reduce the MES-tendency of GEM-MSGCs has to be a detailed study of P_{MES}.

Probability for the ignition of MES $P_{\mathbf{MES}}$

The probability P_{MES}, that a GEM-sparks turns into a MES, is not depending on GEM-attributes like production quality or field conditions in the GEM-holes. This probability was found to be given by the field between the GEM and the other electrodes.

The MES discharge is a very complex process and many parameters are known to influence it. A survey of the observations concerning the ignition of MES and the most relevant parameters are given below:

- **Charge density $\rho_{\mathbf{gap}}$**
  As shown in section 5.1 ("Raether's law"), one important ingredient for the discharge ignition is a high charge density ρ_{gap} in the drift gap. The potential shift is a clear indication that the charge density within the gap between GEM and MSGC must be drastically increased as a consequence of the charge transfer. Please note that the charge density of an ordinary MIP-signal in a high rate beam is smaller by orders of magnitude.

- **Potential shift and the transfer field $E_{\mathbf{trans}}$**
  The field E_{trans} was varied in order to study possible effects on the discharge probability. A strong correlation between the GEM-potential shift and E_{trans} was found,
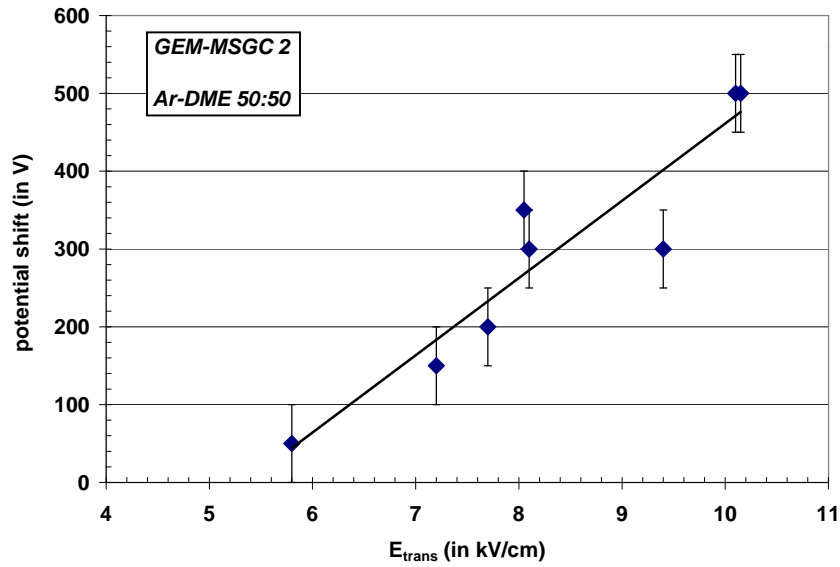
Figure 5.16: Dependence of GEM-potential shift between GEM-spark and final total discharge on transfer field.

as shown in figure 5.16. For transfer fields[2] below $E_{\text{trans}} \approx 5.5$ kV/cm no potential shift of the GEM and thus no current between GEM and MSGC was observed. For 5.5 kV/cm $< E_{\text{trans}} < 8$ kV/cm the potentials are significantly shifted ($\Delta U_{\text{shifted}} \leq 200$ V), but after the initial GEM-spark no multiple electrode spark can be initiated. Only if $E_{\text{trans}} > 8$ kV/cm (and $\Delta U_{\text{shifted}} \geq 200$ V) a MES is initiated.

- **Potential shift and the drift field E_{drift}**
  Similar studies concerning a possible correlation between the potential shift and the drift field E_{drift} were performed, but in contrast to the influence of E_{trans}, no correlation was found here. The tendency that an initial GEM-spark causes a MES is strongly depending on the transfer field, but not on the drift field, since only the very slowly drifting ions enter the drift gap.

- **Time interval between GEM-Spark and MES**
  The time interval between the initial GEM-spark and the complete breakdown varies from 1 to 10 microseconds. No correlation between time and E_{trans} was found. The same result holds for the correlation between time and E_{drift}.

Summarizing the relevant parameters, we find that P_{MES} depends on the field below the GEM E_{trans} and on the charge density ρ_{gap}.

5.4.5 How to effectively reduce MES

From the studies in the lab we may conclude that for a reduction of the MES-tendency there are two possible approaches, (i) the reduction of the transfer field strength and (ii) the

---

[2]all numbers are given for Ar/DME (50:50) at atmospheric pressure

reduction of the charge density in the gap after GEM discharge. In order to investigate their effectiveness in real beam conditions, both possibilities were tested at PSI-beam.

Reduction of Transfer Field

The chambers were operated with a lower E_{trans} (reduction from 8.4 kV/cm to less than 5 kV/cm). Since we wanted to minimize the electric force on the GEM-foil, we also reduced E_{drift}. However, lowering the fields has some non-negligible effects:

- a significantly reduced extraction efficiency of electrons from the GEM lower side (as shown in 2.18). This effect directly influences the total gas gain.

- a lower drift velocity and higher diffusion for electrons (for details c. f. [6])

- a larger Lorentz-angle in magnetic field (for details c. f. [33])

Figure 5.17 shows the quantitative results of the beam test. The number of MES and of conventional GEM-sparks is plotted versus E_{trans}. Also this measurements confirmed that P_{MES} can be reduced by lowering E_{trans}. For a value below 5 kV/cm, no more MES were observed. Please note that a reduction of E_{trans} does not affect N_{GEM} and thus the GEM-spark-rate is not a function of E_{trans}.
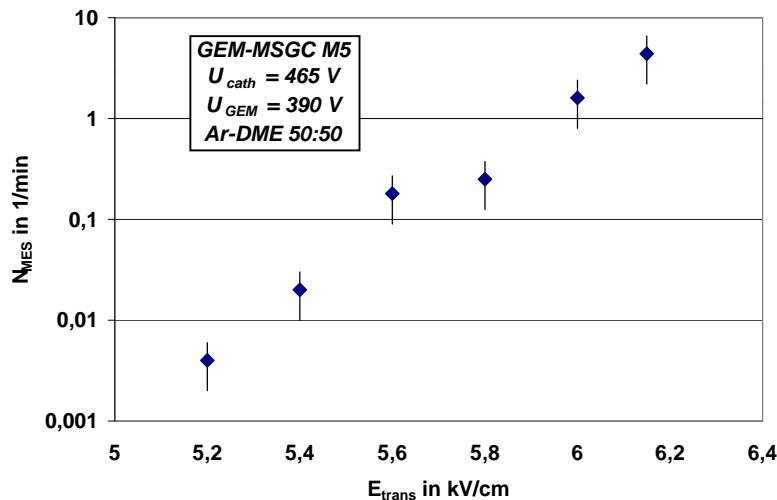
Figure 5.17: Number of MES in PSI-test-beam versus the transfer field. For fields below 5 kV/cm almost no MES were found. This number dramatically increases when going to higher fields.

Lower Charge Density by a segmented GEM

In order to reduce the charge density in the transfer gap, we tried to reduce the amount of charge released by the initial GEM-spark. The only option was a reduction of the GEM

capacitance. A reduction of the GEM-voltage was not possible, as the GEM-voltage is strongly correlated to the total gain.

One of the GEM-MSGCs tested at PSI was equipped with a segmented GEM. By dividing the GEM into 5 — not directly connected — segments the capacitance of originally $C_{GEM} = 45$ nF could be reduced to a value of only 9 nF for each segment. However, the number of MES N_{MES} for the three detectors (1 segmented, 2 not segmented) was found to be similar. Since only a small number of detectors was tested there, the result can hardly be considered statistically significant. Nevertheless, also this result suggests, that not the initial charge spread into the transfer field is the decisive parameter, but rather the continously released electrons *after* the GEM discharge ("potential shift").

5.4.6 Conclusions

The conclusions concerning the MES-phenomenon in GEM-MSGC can be summarized as follows:

- Precursors can effectively be avoided by using fast-switching high-voltage diodes. The cathodes are hindered from charging-up, and hence, the probability for anode-cathode discharges remains very low and destructions can be effectively avoided. Due to the positive results of this study, all main-series GEM-MSGCs for the Hera-B experiment were equipped with diodes.[3]

  Nevertheless, it is important to note that a use of diodes does in no way influences the subsequent MES process. The probability, that an initial GEM-Spark turns into a MES is not influenced by the cathode potential at all.

- The transfer field has to be reduced below 5 kV/cm (in Ar/DME), however disadvantages concerning drift velocity, diffusion and Lorentz angle have to be taken into account. In low transfer fields the number of MES is reduced by orders of magnitude. In the following beam test, combined discharges were very, very rare. A separation of both regions of gas amplification (GEM and MSGC) by low fields is again a very effective way to stop the discharge process.

- The GEM was not segmented for the mass production, since no significant effect on reducing the charge density was found. Nevertheless a segmentation of the GEM capacity has the advantage, that shorts between upper and lower GEM-side do not kill the whole detector, but just one segment. On the other hand, a segmentation means, that more power supplies and cables are needed for beam operation. We therefore renounced on a segmentation for the Hera-B-detectors.

The problem of propagating discharges from a GEM to another electrode is not restricted to GEM-MSGC combinations only. Also in detectors, where a combination of several GEMs is used for gas amplification, discharges between 2 GEM layers or the GEM and the read-out structure have to be expected. In general, a region of low fields between two amplification steps is strongly requested to avoid discharges.

---

[3]Although the diodes have been carefully tested in the lab with regard to overvoltage and irradiation hardness, it turned out that some of these diodes had to be replaced due to shorts after some time of Hera-B operation. This phenomenon is currently under investigation.

Chapter 6

Detector Ageing

For the Hera-B experiment and for most other applications, it is very important that a long lifetime — even in high rate beams — can be guaranteed in advance, since the detectors are expensive and they cannot be replaced during the runtime. Apart from discharge problems, also *ageing processes*, characterized by slow variations of the detector gain, must be excluded during irradiation.

Detector ageing is very difficult to detect in the research and development phase, since the time scales are usually too long for extensive beam tests. Though a high irradiation dose can be accumulated in much shorter time, e.g. by irradiating prototypes in the lab with X-rays, ageing does usually not depend simply linearly on the irradiation rate. Therefore, those tests can only be assumed as an approximation of the real conditions. The measure for the simulated operation time is the accumulated charge per centimeter anode strip. Assuming a gas gain of 4000, an operation period of 10^7 s/a and a particle flux of 10 000 MIPs/mm^{2}s, we end up with an annual charge accumulation of roughly 5 mC/cm for the inner tracking system in Hera-B.

Two different types of ageing were observed during the development phase of the Hera-B detectors. In section 6.1, the Hera-B results concerning the well-known effect of *gas ageing* are summarized, which is characterized by a *loss* in gas gain after some time of operation.

In section 6.2 a completely different type of ageing is presented. It was discovered within this work for the first time and concerns the diamond layer of the MSGC only. In contrast to conventional gas ageing, the gain slowly *increases* during the process of *diamond ageing*. Although this effect is in principle tolerable — since voltages can be adjusted to keep the gain constant — it nevertheless was studied in detail with regard to possible efficiency losses and other side effects.

6.1   Gas Ageing

Concerning ageing problems specific to MSGCs, big efforts [76, 77, 78, 79] have been made to study this phenomenon. In general, these studies are very difficult to perform, since the ageing process depends on a multitude of input parameters, sometimes on a combination of several of them, and often small variations can cause big effects. An extrapolation to different conditions is very difficult and therefore, measurements in an environment as close as possible to the "real conditions" are strongly requested.

6.1.1 Characteristics of gas ageing

Like other gaseous detectors, also MSGCs suffer from sustained irradiation. In general, gas ageing is characterized by a decrease of the detector performance, for example:

- decrease of gas amplification during operation

- significant loss of energy resolution

- currents between anodes and cathodes without irradiation

Especially MSGCs have been found to be particularly prone to fast gas ageing, most likely due to the small distance used for charge multiplication. The avalanching process during operation can be understood as a micro plasma discharge, resulting in a decomposition of the counting gases. These newly created pollutants significantly increase the number of free radicals in the gas. Resulting from the formation of polymers, the electrodes are getting covered by an insulating layer. In an optical inspection of the exposed area in severely damaged MSGCs the ageing process is characterized by a discoloration of the anodes. Using an electron microscope, the structure of the deposits is visible, as e.g. shown in figure 6.1. When those polymers stick to the anodes, the field strength close to the anodes can be significantly reduced. Furthermore, the insulating extra layer is known to perturb the signal propagation and, in addition, the discharge probability increases.
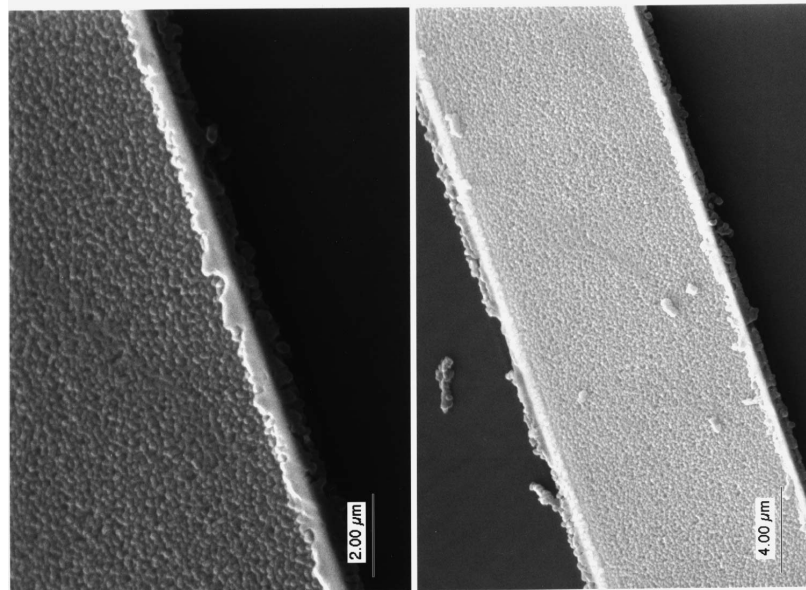
Figure 6.1: Photograph (electron microscope [80]) of the MSGC electrodes after gas ageing. The bare metal anodes (light areas, 10 μm thickness) are covered by pure carbon (strongly irradiated areas) or hydrocarbons (weakly irradiated areas). The biggest effects can be found on the edges of the anodes.

6.1.2 Parameters

First of all, the choice of the operating gas plays an important role. Especially hydrocarbons induce very fast ageing, whereas dimethyl-ether (DME) and tetra fluoride (CF_4) are known to allow for extended life-times, since polymerization is found to be small or even negligible there [78, 76, 77].

Furthermore, outgasing of impurities in the detector materials can strongly influences the gas ageing process. The worst candidates are known to be halogenides, hydrocarbons and silicon, where even impurities in the ppm-range cause significant effects. Therefore, the detector materials have to be chosen extremely carefully, since the glass, the frames, the drift electrode and even the glue and the metal strips may induce gas ageing, as e. g. reported in [79].

Also the materials used in the gas station and the tubing can be a severe source for pollutants. Non-metallic materials may outgas some vapors, which — transported with the gas flow — might be deposited on the electrodes and the insulators of the detector, and favor the polymerization of radicals in the avalanche as well.

6.1.3 Precautionary measures for the Hera-B GEM-MSGCs

Since a lot of information concerning ageing effects was published (cf. literature in the previous section) when first prototypes for the Hera-B experiment were developed, particular care was taken to reduce gas ageing to the lowest possible level (see also [81]).

A mixture (50:50) of Argon and Dimethyl-ether (DME) was chosen as the counting gas which, apart from its resistance against ageing, provides excellent operation conditions. In contrast to e. g. CO_2, a very common non-flammable counting gas, DME is an excellent photon quencher, therefore providing a significantly reduced discharging rate. Nevertheless, DME is known for attacking for example the non-metallic washers material, thus inducing strong outgasing. Therefore all washers in the Hera-B gas systems were replaced by washers made of Kalrez, much less reactive when exposed to DME. For the same reason, the entire gas system is made of stainless steel pipes, carefully cleaned prior to installation. We furthermore strictly refrained from using the widely spread Teflon as a sealing material, because of known interactions when exposed to DME.

All detector materials were carefully selected in order to obtain an "all clean" detector. The electrode strips are made of gold, which is known to behave passively, and the frames are manufactured from G10 [63], a carefully tested material similar to GFK, but free of halogenides. The drift electrode consists of a well-cleaned copper layer and when the GEM-foil was introduced in the detector, also this part was studied carefully. As expected, no effects concerning gas ageing were found, since it consists of Kapton and copper only. Also the glass substrates with the additional diamond layer are minor critical, when carefully cleaned.

Basing on a detailed list of already investigated glues, published in [76], we also performed extensive studies for all glues we intended to use [33],[8]. The results that gas ageing could not be observed after an accumulated dose in the order of 25 mC/cm gave us additional confidence, that neither STYCAST 1266 [82], EPO-TEK H72 [83], Eccobond 285 [84] nor TORRSEAL [85] produce significant outgasing pollutants. All prototypes and main-series detectors were assembled in the clean room only, thus excluding additional pollution e. g. from dust. Furthermore, in all our test-setups particular care was taken to provide an extremely clean gas system.

As a result of this consequent avoidance of any possible pollutant, no effects of gas ageing were observed until autumn 1999, except for one case, were a small amount of water was added to the counting gas, resulting in severe gas ageing [33]. When going back to dry counting gases again, the gas ageing process stopped immediately.

6.1.4   Gas ageing in main series chambers

Once more, a severe setback came after a test of full-size MSGC in "real conditions" at the PSI-beam. Compared to Hera-B conditions the operation in the pion and proton beam was 30 times accelerated, the rate was $\approx 5 \cdot 10^4/\mathrm{mm}^2\mathrm{s}$. Nevertheless, for the illuminated area of about 30 cm^2, the accumulated total dose after the beam test was only 2 mC/cm, corresponding to roughly 0.4 years of Hera-B irradiation.
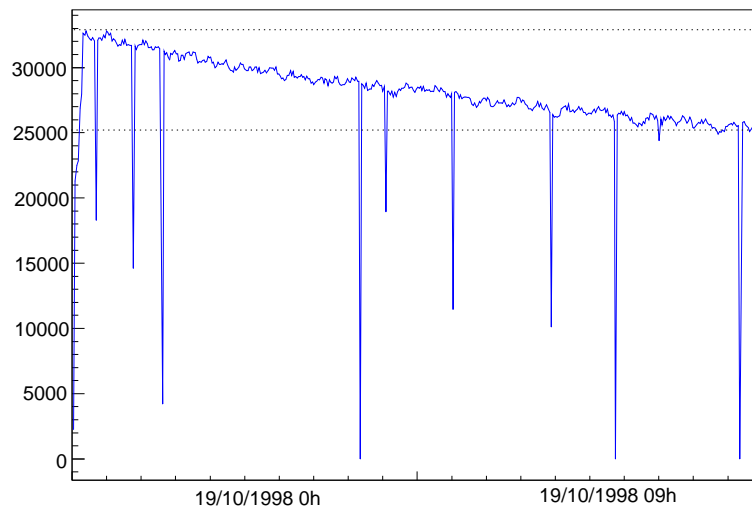
Figure 6.2: Gas ageing after one night at PSI test beam, reflected by a decreasing detector current (for a constant irradiation rate).

Figure 6.2 shows a severe decrease of the detector current (I_{drift}) in a constant irradiation rate during the PSI beam-test. After 2 days of running, the chamber suffered from severe gas ageing and in the end, the gas amplification in some areas was reduced to almost zero. This result is very astonishing, since ageing tests in the lab (with an order of magnitude larger accumulated dose) did not show any effects of gas ageing. Similar to the last detectors in the lab, the GEM-MSGCs for the PSI test originated from the main series batch. The gas system at PSI was installed under the same strict precautions as in the lab and only premixed gas bottles from the usual supplier were used.

Investigation of Gas Ageing

A subsequent scan of one of these detectors exposed to the PSI-beam was performed in the lab, using a collimated X-ray beam. By a comparison of the gas gains with and without GEM amplification, it could be excluded, that the GEM is involved in the ageing process. The detector currents, reflecting the gas amplification, were monitored as a function of the irradiated position (12 mm collimator). The scanning result of a detector, which was exposed to the PSI-beam mainly in the center, is shown in figure 6.3. Surprisingly, the gas gain

is significantly reduced in the outer parts, but almost unaffected in the area of the *highest* accumulated rate.
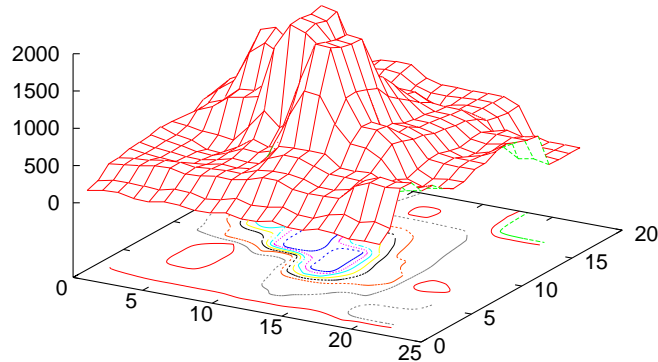
Figure 6.3: Current as a function of the irradiated position with fixed X-ray irradiation rate, showing that gas amplification after the ageing process at the PSI-beam is significantly reduced in the outer parts, but almost normal in the central part, the areas with the highest accumulated irradiation dose.

It was even more surprising, that the gain along some anodes in the outer parts quickly recovered after irradiating restricted areas. In figure 6.4 is depicted, that the gain after 12 h of very intense X-ray irradiation, corresponding to an accumulated dose of ≈ 0.3 Mrad, obviously recovered on each of the three spots.
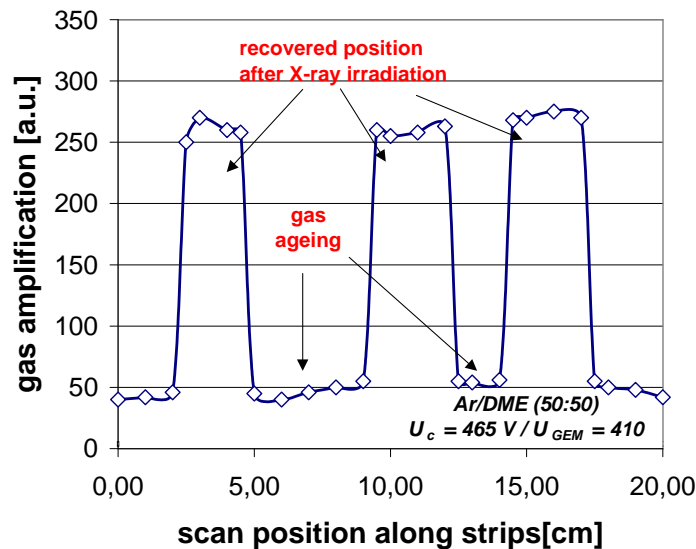
Figure 6.4: Irradiation current in regions, harmed by severe gas ageing (low gain region), and for recovered spots (high gain region). The recovery was induced by high-rate X-ray irradiation, most likely transforming the high resistivity coating layer into pure carbon with increased conductivity.

A surface analysis [61] proved that all anodes — but not the cathodes — were covered by an additional surface layer (see diagram in figure 6.5). An approximately 85 nm thick, conductive layer of carbon (C: 80 at% , H: 8 at%, O: 6 at% and N, Au, Si) was found in the irradiated area. Outside, in the weakly irradiated areas, there was a deposit of typically 30 nm of mainly insulating hydrocarbons (C: 70 at%, H: 20 at% and O, Si, N and Au).
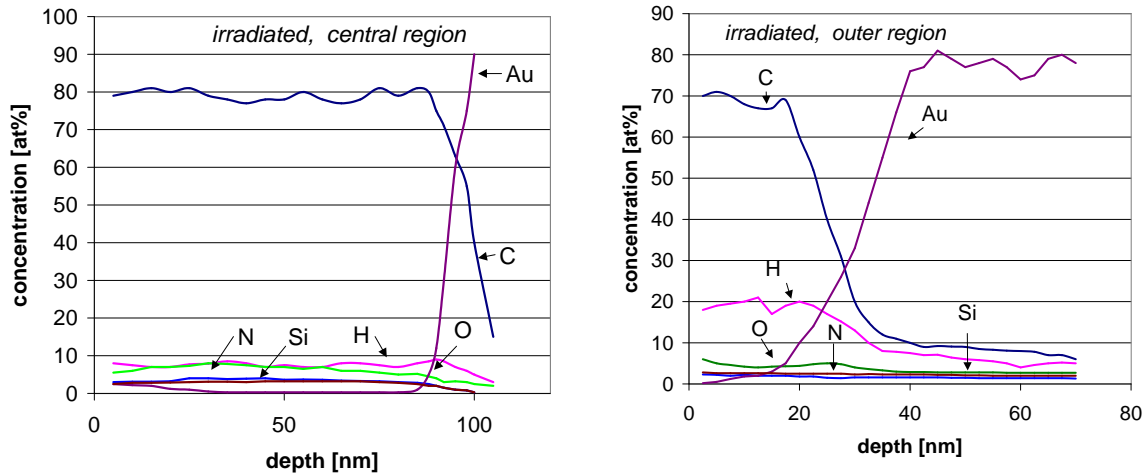
(a) concentration of elements in the inner parts, mainly conductive carbon of 85nm thickness

(b) concentration of elements in the weakly irradiated areas, mainly highly resistive hydrocarbons of 30 nm thickness

Figure 6.5: Results of the surface analysis of the anode strips after gas ageing [61]

The gas ageing process at PSI

This result gives rise to the following explanation for the previous observations:
Due to pollutants, radicals are being created in the process of gas amplification. The amount strongly depends on the irradiation rate, the gas amplification factor and the level of pollution, not necessarily being simple linear functions. After a given chemical reaction time, the formation process of the polymers – typically hydrocarbons of all kinds – is initiated. Those depositions mainly stick to the anodes, since the avalanching process is restricted to the vicinity of the anodes only.

The observation of pure carbon on the anodes in the area of the highest irradiation level strongly supports the assumption, that the (insulating) hydrocarbons can turn into (conductive) carbon, when the energy of the avalanche plasma is sufficient for this reaction; in other words, when the rate and the gas amplification is large, as it was fulfilled in the central regions of the detector. In contrast to the insulating layer, electrons are able to transfer the conductive carbon layer, and the charge can be detected on the anode strip. Also in the lab, when irradiating the MSGC with an high rate X-ray beam, insulating layers were transformed into conductive material ("recovered regions").

Nevertheless, the scenario that the detector will be operational despite massive ageing, is very unlikely in the Hera-B beam, since the charge density there is small compared to the test conditions at the proton and pion beam or X-ray source. Apart from this, an additional

carbon layer on the anodes cannot be tolerated during operation, due to possible side effects, e. g. an increased discharging rate. It was therefore lethal to investigate the source of pollution in the actual system.

Systematic gas ageing tests with X-rays

For a systematic investigation of the gas ageing phenomenon, the conditions at the hadron beam at Hera-B had to be simulated in the laboratory. The highest rate, and therefore the largest acceleration factor, can be obtained in an X-ray beam. However, for an extrapolation of the results to the real conditions, the following considerations have to be taken into account:

- The primary ionization of the Cu-K_α photons is roughly a factor of 10 larger than the ionization of a minimal ionizing particle in the Hera-B environment. This effect can be corrected by either reducing the gas amplification by a factor of 10 or by assuming a factor of 10 larger irradiation rate. In the first case, the operation voltages have to be reduced, thus not reflecting the real operation conditions and leading to a much lower density of radicals. In the second case, the gain corresponds to the real conditions, and thus the density of radicals. Hence, as a rough estimation, the irradiation rate was corrected by a factor of 10 for identical rates.

- Due to the slow chemical reactions, involved in the ageing process, the velocity for a given irradiation rate surely depends on the gas flow in the detector. Although most ions and radicals in the gas avalanche have a rather short lifetime, it was observed, that for very low flows, the ageing process is enhanced, most likely due to pollutants with a long lifetime. These molecules cannot be removed from the active detector regions and they further participate in the polymerization process. We therefore increased our gas flow in all accelerated measurements.

Ageing studies in the lab

In the first step, it was verified, that ageing was neither caused by a dirty gas system nor by simple outgasing. For this purpose, all parts of the detector were separately tested with regard to gas ageing once more. That result was confirmed by gas chromatography tests, showing no indication for any pollutants in the detector material. In order to be on the safe side, the design gas flow for the inner tracking system was increased from 10 ml/min to 18 ml/min to reduce the outgasing concentration of trace pollutants.

For a separation of the influence parameters, the systematic investigation was restricted to three main approaches: (i) the investigation of the influence of the size of the irradiated area in order to find appropriate test conditions (ii) the reduction of outgasing by heating of detector materials and (iii) the study of the influence of the gas type on the ageing process.

- **Influence of the size of the irradiated area**
  In most studies reported about in the literature, the size of the irradiated area is limited to a few square millimeter only to keep the rest of the detector for further measurements. During this ageing test, the irradiated area was increased to values up to 900 mm^2. A comparison of a large area irradiation at low rate and a small area irradiation at high rate is shown in figure 6.6. The irradiated area has a clear influence on the gas ageing process: It is enhanced for a large area irradiation, even in case of a reduced irradiation rate. The conclusion must be that process of formation of polymers is more efficient, if
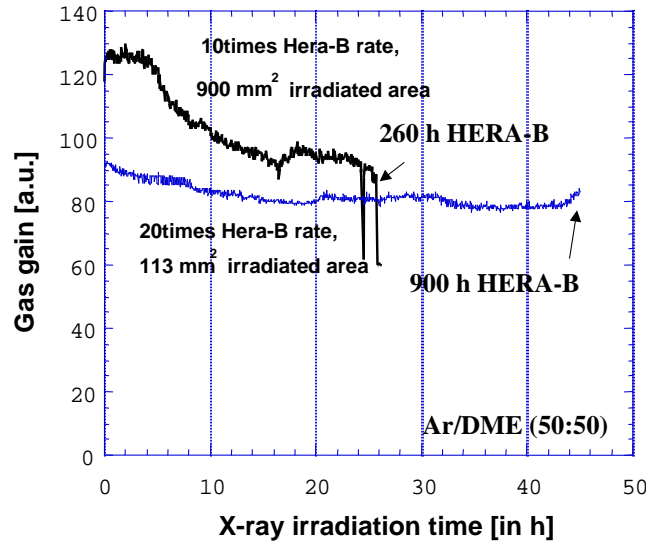
Figure 6.6: Gas gain as a function of the irradiation time. In case of large irradiated area, the ageing process is significantly increased, even in case of smaller irradiation rate (reduction by a factor of 2).

the irradiated detector area is large. In this case, the radicals are not being neutralized by being transfered out of the active region, but they continue to support the ageing process. Unfortunately, a reduction of the irradiated area is of course no option for Hera-B. The results even suggest, that the gas ageing at Hera-B might be even worse, since the chamber is always irradiated in total.

- **Heating of detector components**
  Heating of detector components is a standard technique to reduce the amount of out-gasing vapors in the material. In our case, the drift electrode was heated overnight at 200 °C before being glued to the GFK support frame. Also the G10-frames were heated (at 100 °C under continuous nitrogen flow) before installation.

  In figure 6.7 the development of gas amplification is shown for a heated detector. Compared to the average of non-heated detectors, the decrease in gain is smaller. However, in other chamber individuums this effect was much less significant. This observation lead to the conclusion, that gas ageing is less severe after chamber heating, but it could not be completely excluded.

- **Influence of the type of counting gas**
  As the last option, Ar/DME was replaced by a gas mixture of (i) Ar/CO_2 (70:30) and (ii) by $Ar/CF_4/CO_2$ (65:30:5), in order to study the influence of the gas type on the gas ageing phenomenon.

  In both mixtures, no effects of gas ageing were observed after an integrated dose of more than 20 mC/cm. But as shown in figure 6.8, a new effect was observed: the gain slightly increases with irradiation time. This phenomenon leads directly to the process of diamond ageing, as described in detail in paragraph 6.2.
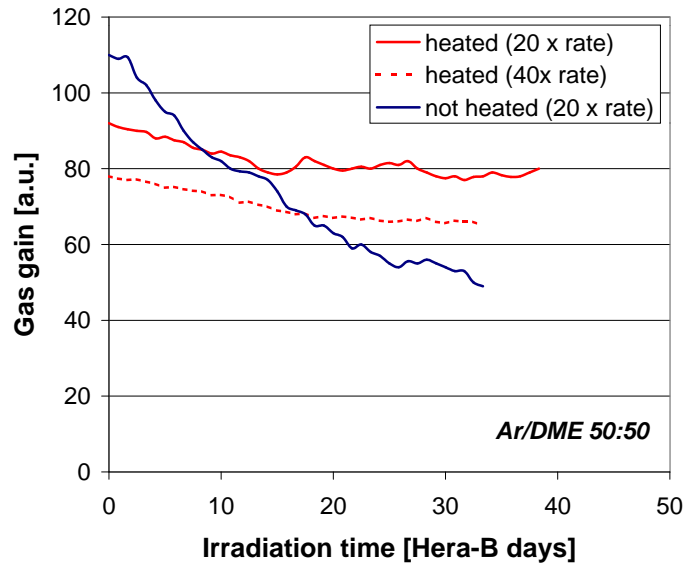
Figure 6.7: Three independent measurements of gas ageing in the heated detector. The gain decrease in the heated chamber was found to be less severe, nevertheless, it was not completely excluded.
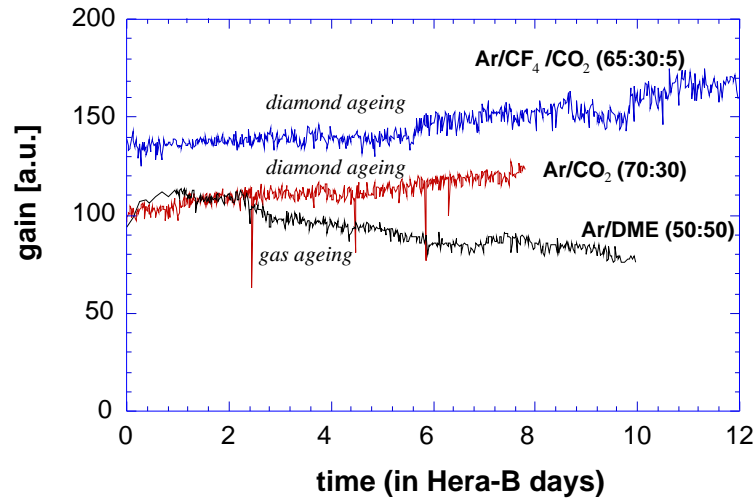
Figure 6.8: Strong gain variations after intense irradiation for three different gas mixtures. The effect of increasing gain (Ar/CO_2, $Ar/CF_4 CO_2$) has nothing to do with gas ageing, it is caused by the phenomenon of "diamond ageing".

6.1.5 Conclusions

Although extended ageing studies have been done in the research phase and peculiar care was taken to built an extremely clean detector and gas system, nevertheless massive gas ageing occurred during a beam test at PSI.

Up to now, it is unclear why only the Ar/DME mixture induced this severe gas ageing. Two possibilities are realistic: Either the purity of the gas itself was poor (but this was denied from the supplier and it seams unlikely after the gas chromatography tests) or the DME caused chemical reactions with the material of the detector or the gas system (but in principle this was tested in extended ageing tests before autumn 1998).

It was shown above, that the ageing process could be slowed down by (i) a reduction of the irradiated area and (ii) by heating of detector components. But the only way to completely avoid ageing, was to refrain from dimethyl-ether as a counting gas. Since it was observed that the GEM looses mechanical tension when operated in DME, a change to another gas mixture was mandatory in any case.

6.2 Diamond Ageing

The phenomenon of *diamond aging* was first discovered during long-term irradiation with X-rays, appearing as a slow but — in the end — significant increase of the detector gain. This effect is provoked by a reduction of the thickness of the diamond coating layer in the gap between anodes and cathodes; it strongly affects the electrical field geometry and, hence, also the electron amplification process.

6.2.1 The Physics of the Diamond Ageing process

Before presenting the details of the experimental results, the physics behind the process of diamond ageing is summarized in this section. This procedure will help to combine the various experimental results into a conclusive picture.

The pulse-height spectra

Diamond ageing gives rise to three changes in the detector performance:

- Increase of the gas gain of the MSGC

- Temporary loss of energy resolution

- Rate dependence of the MSGC-gain in the final stage.

All stages of the diamond ageing process are reflected in the shape of the pulse height spectra of the detector, when irradiated with a monoenergetic source. The process can be divided into three consecutive phases, as illustrated in the cartoons in figure 6.9–6.11.
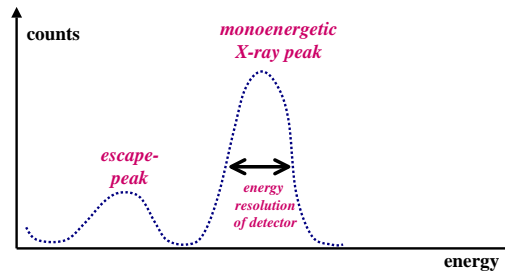
Figure 6.9: Pulse-height spectrum before diamond ageing. Good energy resolution and clear separation of ^{55}Fe-peak and escape peak.

Phase 1:

First changes due to diamond aging appear as a slight increase in gain after a radiation dose of about 5 mC/cm (corresponding to one year of irradiation at Hera-B). In the range of an

equivalent dose of 1 to 4 years of Hera-B year operation, the peaked pulse-height spectrum turns into an almost flat function. Due to a locally varying gain along the strips, resulting from an inhomogeneous radiation damage in the diamond layer, the energy resolution is temporarily very poor.
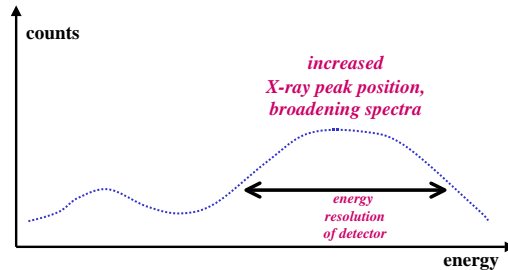
Figure 6.10: Diamond ageing at the end of phase 1, characterized by an increased gas amplification factor and a poor energy resolution.

Phase 2:

After another period of irradiation, the energy resolution begins to recover. A new peak in the pulse-height spectrum at a much higher energy appears. At the same time, the position of this peak (and thus the gas amplification) becomes rate dependent. At the end of this phase, the gain is increased in the entire rate regime; however the biggest effect was observed for very low rates, where up to a factor 5 is between the gain before and after the irradiation. In the high rate regime, a factor of 3 is typical.

Phase 3:
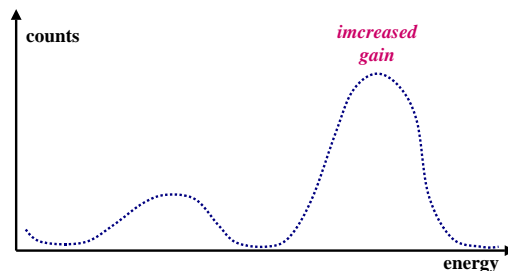
Figure 6.11: Diamond ageing in phase 3. This period is characterized by a recovered energy resolution and an increased — but rate dependent — gas amplification factor.

In this phase, equivalent to more than 5 years of Hera-B operation, the detector performance remains stable, the detector is still fully operational. This phase is characterized by a rate dependency of the gas amplification and by a significantly increased gas amplification.

The evolution of the energy resolution as a function of the irradiation time is depicted in

figure 6.12, illustrating the different phases during the diamond ageing process.
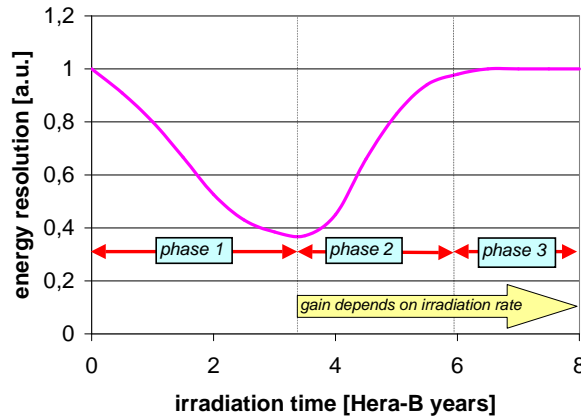
Figure 6.12: The evolution of the energy resolution as a function of the irradiation time. The resolution decreases in phase 1 and starts to recover in phase 2. In phase 3, the nominal value is obtained again.

The Etching Process

Diamond ageing occurs under intense radiation in combination with gas amplification only. This fact strongly suggests, that diamond ageing is caused by the electron avalanches in the region close to the anodes. It can be excluded that irradiation only may change the structure of the diamond coating this efficiently.

From simulations it is known, that a fraction of electrons of the avalanche ends on the diamond coating in the vicinity of the anodes. The amount is depending on the field geometry and on the transport parameters of the gas (i.e. longitudinal and transverse diffusion). This effect is relevant for charging-up and — with the spread electrons continously etching the diamond layer during operation — it is found to be relevant for the diamond ageing process as well.

Effects of the etching process were observed for all gases we tested (see development of gain in figure 6.8 for Ar/CO_2 and $Ar/CF_4/CO_2$), whenever they were not covered by the dominant effect of gas ageing (this case is represented by the Ar/DME-graph in 6.8). However, it could be derived from the slope of the gain curve, that the gas mixture is a decisive parameter for the velocity of the etching process. For example in $Ar/CF_4/CO_2$ (65:30:5), which is known to be a good "etching gas", the process was significantly enhanced.

As a result of the etching process, the thickness of the coating layer decreases in the vicinity of the anodes. After an optical inspection, where the irradiated areas appeared as prominent spots of discoloration (see figure 6.13), an irradiated wafer was analyzed by more advanced techniques[61]. The study of the coating layer thickness (see figure 6.14) clearly demonstrated that after an irradiation dose equivalent to approximately 3 years of Hera-B operations the originally homogeneous thickness is reduced from 80 nm to almost zero in the vicinity of the anodes.
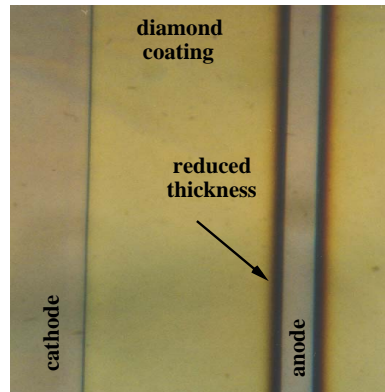
Figure 6.13: Photograph of the MSGC substrate after diamond ageing; view on anode, cathode and gap
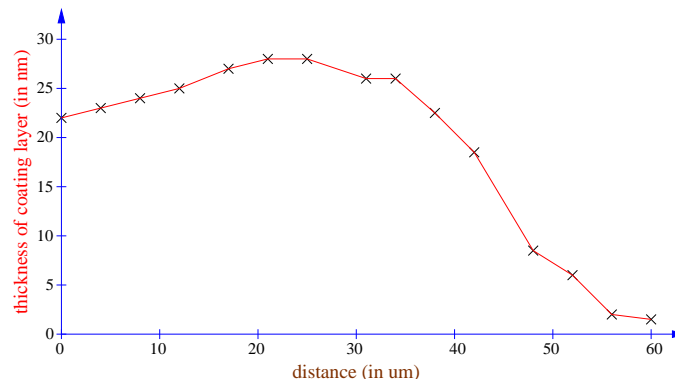
Figure 6.14: Thickness of coating layer after diamond aging, x<0 represents the cathode, 0 < x < 60μm the gap region and x> 60μm the anode region. The thickness of the coating layer in the beginning was in the order of 80 nm

The Field Geometry and Effects on the Gain

The dependence of the gain on the irradiation rate is very surprising for coated MSGCs, however very typical for uncoated MSGCs. A reduced thickness of the coating layer significantly influences the conductivity between anode and cathode and thus the field configurations and thus the electrostatic conditions before and after diamond ageing. The potential and the electric field a few micron above the MSGC plate is depicted in the cartoons in figure 6.15.

As soon as the diamond layer is reduced to a thickness of only a few nanometers, the field geometry drastically changes. The electric field in the vicinity of the anodes increases and — for a given cathode voltage — it is reduced in the region between anodes and cathodes. Since the gas gain depends on the field very close to the anode only, an increased gain is a necessary consequence.

Especially when the thickness d of the coating layer is close to zero, the resistivity R changes rapidly (R $\sim \frac{1}{d}$). This effect may illustrate, why the gas gain along the anode strips process is found to be very inhomogeneous at the end of phase 1, resulting in an almost flat
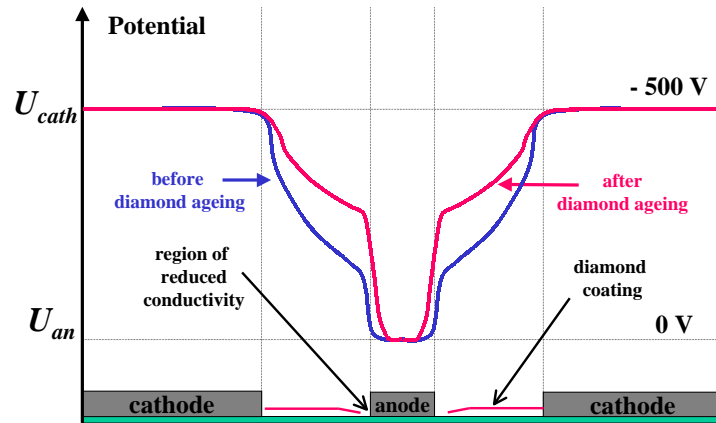
(a) potential before and after diamond aging
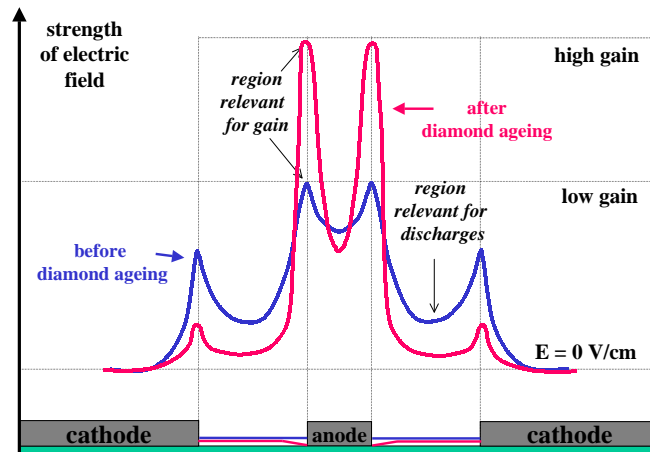
(b) electrical field strength before and after diamond aging

Figure 6.15: Cartoon of the electric potentials and the electric fields a few micron above the anodes and cathodes. Due to changes of the thickness of the diamond layer, dramatic effects especially for the gain were observed.

pulse-height spectrum.

Due to the fact, that the coating is completely etched off next to the anodes in phase 3, a stable operation-point with a homogeneous gain can be obtained. This stage with a clearly improved energy resolution is found to be stable in time.

Please note that the coating layer in the region between anodes and cathodes and close to the cathodes is less affected, as most of the electrons end in the vicinity of anodes. The remaining coating layer guarantees for a sufficient conductivity to avoid charging-up effects. But after very long time scales (> 10 Hera-B years) even the coating layer in the central region

might be etched off, resulting in electric field conditions identical to non-coated MSGC. In this stage, the detectors cannot be operated in high rate beams due unavoidable charging up effects.

6.2.2   The experimental concept

Though first measurements showed, that the average gain significantly increases during operation, it is considered the worst scenario to loose some of the events completely, while others are enhanced. In order to detect possible losses in the detector efficiency, an experimental setup for a detailed study of the diamond ageing process was prepared in the laboratory.

The X-ray irradiation

For an accumulation of a radiation dose equivalent to 6 years of Hera-B operation in a period of roughly one month, a GEM-MSGC was irradiated by a high intensity X-ray source. This procedure can obviously not replace a longterm operation in the Hera-B beam. But since the time scales for the diamond ageing process are in the order of several years of operation in Hera-B conditions, the irradiation time had to be compensated by a more intense beam for technical reasons.

A crucial point in this measurement is the assumption, that the damage on the diamond layer induced by X-rays is comparable to the effects of hadronic beams. Since the process is driven by irradiation in combination with gas amplification only, the effects of the irradiation source are considered minor important. The most relevant parameter is the size of the avalanche, which is assumed to determine the velocity of the etching process. This valuation of the irradiation dose was already applied for the gas ageing measurements (see section 6.1.4.

Nevertheless, a clear answer cannot be given, since longterm tests in "real conditions" cannot be performed because of the large time scales. However, it could be excluded in a high rate proton and pion beam, that the diamond ageing process is significantly enhanced in hadronic beams (see PSI beam test results in section 7.3).

The X-ray test facility

A full-size main-series GEM-MSGC was mounted on a trestle in front of the X-ray source together with a collimator. For adjusting the rate and the beam homogeneity, the distance between the MSGC and the X-ray-source could be varied from several centimeters up to 1 m. In order to allow for an irradiation of any chamber position, the MSGC could be moved in 2 dimensions, controlled by a computer driven step motor.

The X-ray-tube was operated at an acceleration voltage of $U_{\text{X-ray}} = 37$ kV. A circular shaped collimator with a diameter of 12 mm was chosen, large enough to ensure that, on one hand, a representative part of the (full-size) detector was irradiated and small enough, on the other, to provide the required homogeneity of the irradiation rate.

The standard drift electrode consists of 300 μm G10 and 125 μm Kapton, being however too thick to obtain a sufficient rate when irradiated with the ^{55}Fe-source. Thus — as the only difference to the original main series chambers — the drift electrode of this MSGC was milled at four positions along one strip, down to a total thickness of about 150–200 μm as demonstrated in figure 6.17 and 6.16.

A premixed gas of 60 % Argon and 40 % CO_2 was chosen and the chamber was operated at "Hera-B-conditions", i. e. $U_{\text{drift}} = 3200$ V, $U_{\text{GEM}} = 410$–430 V and $U_{\text{cath}} = 410$–470 V. All
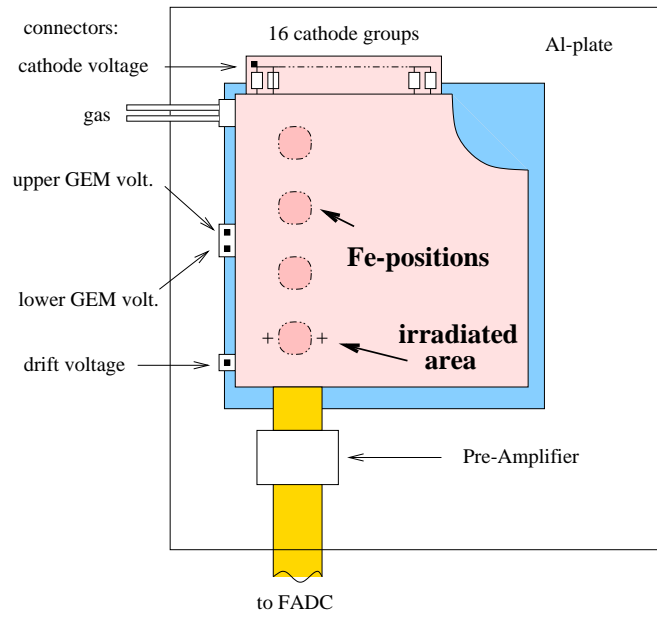
Figure 6.16: The MSGC, prepared for the efficiency measurement.
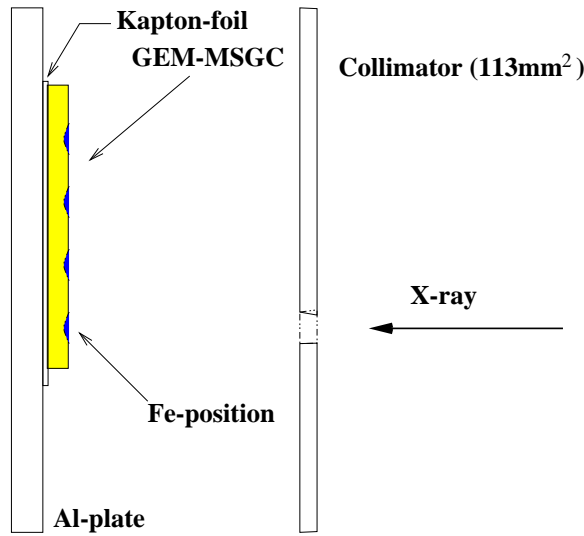
Figure 6.17: The x-ray test facility.

four detector currents (drift, cathode and the two GEM electrodes) were monitored during the measurements, in order to detect instabilities (like discharges) or slow processes (like gas ageing) and to adjust the desired beam rate. To obtain sufficient counting rates for the analysis chain, seven hardwired anodes were connected to a preamplifier (VV50). The differential output signal was connected to an oscilloscope, then transferred to the computer via GPIB. A LabView-program was used to detect the pulse-height of the signals, to create pulse-height spectra and to control the changes of the average gain in time.

The experimental program

The periods of irradiation were stopped for approximately 1 hour a day for control measurements, performed with a monoenergetic ^{55}Fe source, giving a precise determination of actual status of the detector. All three phases of diamond aging, as known from previous measurements, could be observed. The pulse-height spectra, the development in gain, the energy resolution, the rate dependency and the efficiency were studied in detail.

Stable Conditions during the Measurements

Since the total measurement time for this study summed up to more than one month, stable conditions for the rate and pulse-height measurements had to be guaranteed for the whole period.

- The GEM voltage was actively regulated between $U_{GEM} = 408.5V$ and 411.5V. The fluctuations had a small influence on the measured rate, the value was determined to roughly 1%.

- The temperature in the X-ray facility decreased, but neither the threshold nor the pulse-height were influenced. Therefore, it was refrained from correcting the data for temperature and pressure.

- The accuracy of the position of the ^{55}Fe-source after removing and remounting was found to be better than 0.5 mm, resulting in rate variations in the order of only 1 %.

6.2.3   Results

In this section, the experimental results concerning the phenomenon of diamond ageing are presented. In the focus of interest was the question, if the detector efficiency is affected by long term irradiation. The accumulated charge after irradiation was equivalent to 6 years of Hera-B-operation, twice the time the experiment is supposed to run. After these 6 years, the detector was still fully operational, but several changes in the detector performance had occurred. Although the tests were performed with a GEM-MSGC combination, the process of diamond ageing is restricted to the MSGC part only. All effects can be detected when operating the detector in MSGC-mode only.

Spectra

Due to the relatively low rate of the ^{55}Fe-source and the strong rate dependence of the gain in this rate regime, the development of the diamond ageing in time is clearly visible in the ^{55}Fe-spectra.

   A representative spectrum from the beginning with a prominent ^{55}Fe-peak is shown in figure 6.18. After an irradiation time equivalent to 3.5 years and 5 years of Hera-B operation, the spectra (see figure 6.18 (right) and figure 6.18 (left)) are found to be significantly broader, reflecting a severe loss in energy resolution. The gain increased by a factor of 4 and 6 respectively[1].   Finally, after an irradiation dose equivalent to 5 years of operation in

---

[1]It should be added here, that the cathode voltage and thus the gain had to be reduced for technical reasons. Due to the large variation in amplification during the diamond ageing process on one hand, and the limited number of readout channels on the other, the peak position was always adjusted to the channels with best resolution.
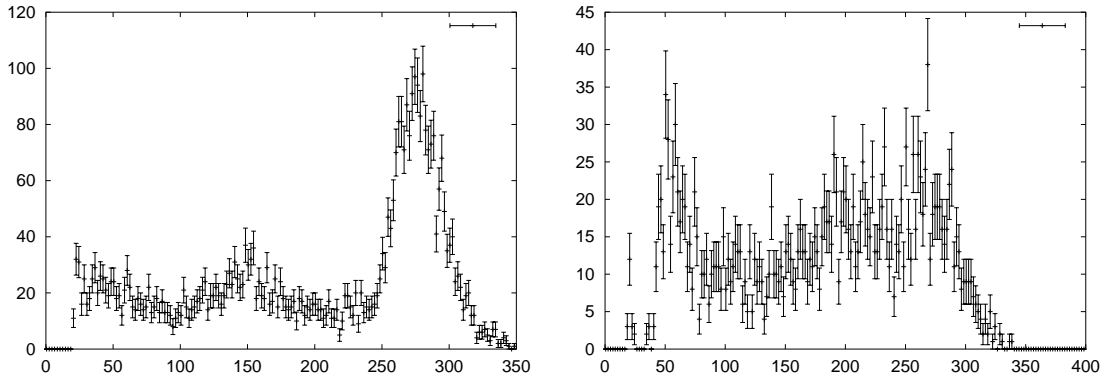
Figure 6.18: The ^{55}Fe-spectrum in the beginning of the irradiation (left graph) shows a clear separation of the ^{55}Fe-peak and the escape-peak (U_{cath} = 470 V, U_{GEM} =430 V and U_{drift} =3200 V). With ongoing irradiation (3.5 Hera-B years), the gain rises and the energy resolution deteriorates (reflected by an increasing width of the ^{55}Fe-peak), as shown in the right graph. (U_{cath} = 410 V, U_{GEM} =430 V and U_{drift} =3200 V)
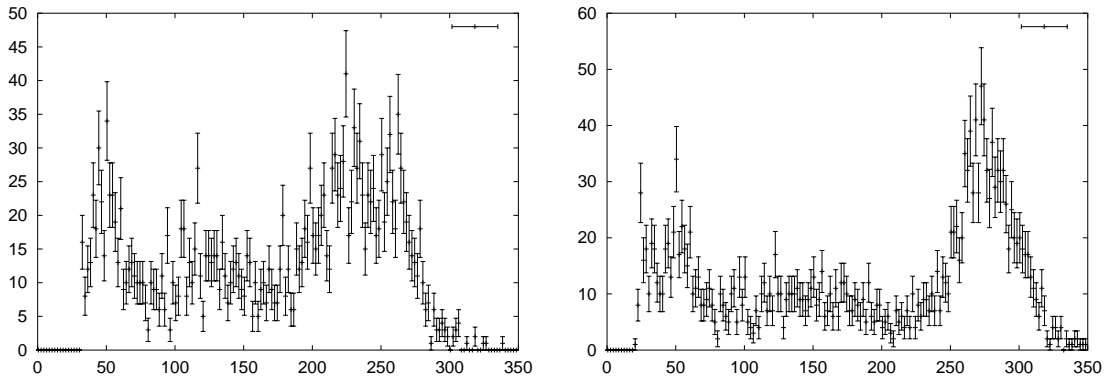
Figure 6.19: ^{55}Fe-spectra in phase 2 (left), after 5 years of Hera-B operation. In phase 3 (right), after about 5.5 years of Hera-B operation, the clear peak in ^{55}Fe-spectra reappears. The cathode voltage was reduced by 40 V and the GEM voltage by 20 V respectively! (U_{cath} = 430 V, U_{GEM} =410 V and U_{drift} =3200 V).

Hera-B conditions, the peaks in the spectra reappeared and the energy resolution improved significantly, compared to the poor resolution in the end of phase 1. This is a clear signal, that the ageing process of the diamond-like coating has reached a stable state. A typical spectrum of phase 3 is shown in figure 6.19 (right).

Evolution of the Energy Resolution

A variation in the energy resolution of the detector is experimentally observable by its inverse, the relative width ($\frac{\Delta E}{E}$) of the ^{55}Fe-peak. This parameter, defined as the full width at $\frac{1}{3}$ maximum, normalized to the maximum position of the peak, was observed during the

irradiation. As shown in figure 6.20, all 3 phases are clearly reflected by the curve shape.
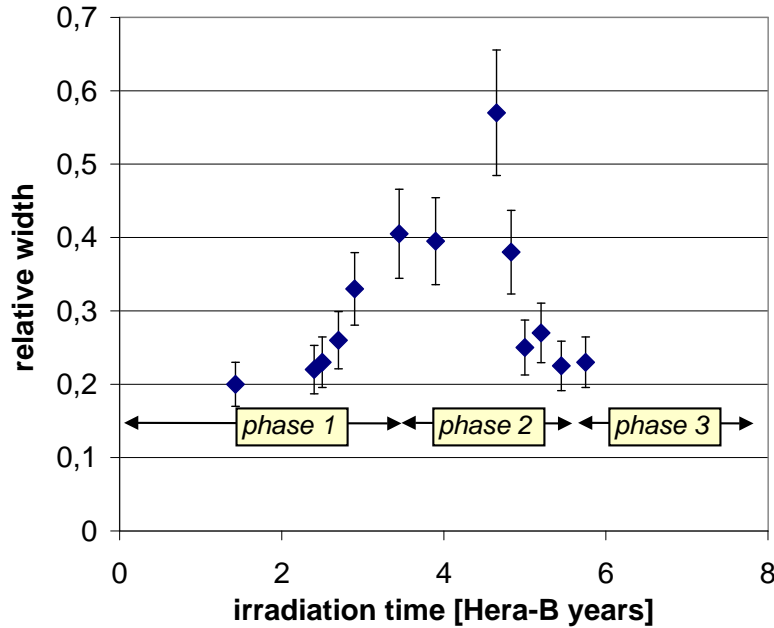
Figure 6.20: Development of the relative width of the ^{55}Fe-spectra. The relative width increases (phase 1) and reaches a maximum after about 4 years (turn over between phase 1 and phase 2). After the coating layer is completely etched off close to the anodes, the energy resolution recovers, leading to a decreasing pulse width (phase 3).

In principle, the same effects, i. e. broadening spectra and a rising gain, were observed in the X-ray spectra as well. But as these irradiation source is not pure monoenergetic (Cu-K$_\alpha$ peak at 8 keV and an additional X-continuum) the effects are less prominent. For this reason, the X-ray spectra were not taken into account for the analysis of diamond ageing.

Rate Dependence

After an irradiation dose equivalent to 3 years of Hera-B operation, the first indication for a rate dependence of the gain was detected. In the beginning, the effect was slight: when changing the load from 20 to 3 times the Hera-B rate, the pulse-height increased by only 7 %. But this effect was enhanced with ongoing irradiation, as shown in figure 6.21. After about 6 years of Hera-B operation no further changes in rate behavior were observed, except for small fluctuations due to variations in the external conditions (pressure, temperature).

At the end of the measurement, a final rate scan covering the relevant range from 0.2 to 5 times the Hera-B load was performed. As depicted in figure 6.22, the slope of the curve at 1× Hera-B load (i. e. 10 kHz/mm^{2}s at 40 MHz target rate) is significantly steeper compared to the one at higher rates. Although small rate variations of the beam at Hera-B cause greater changes in gain, this effect is considered to be tolerable.

Also the result of a rate dependent gain corroborates that thickness and thus the conductivity of the coating layer is significantly affected. In intense beams the charge cannot be removed from the insulating glass substrate and thus field close to the anodes is reduced.
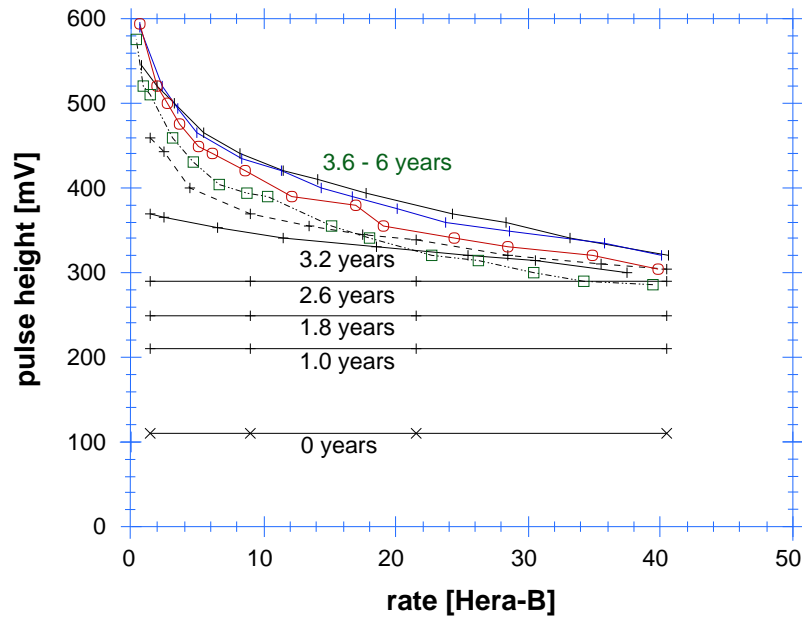
Figure 6.21: Development of the rate dependence as a function of irradiation time. The pulse-height is plotted versus the rate in units of the Hera-B load. After 3 years of operation the rate dependence occurred, reaching a stable state after 6 years
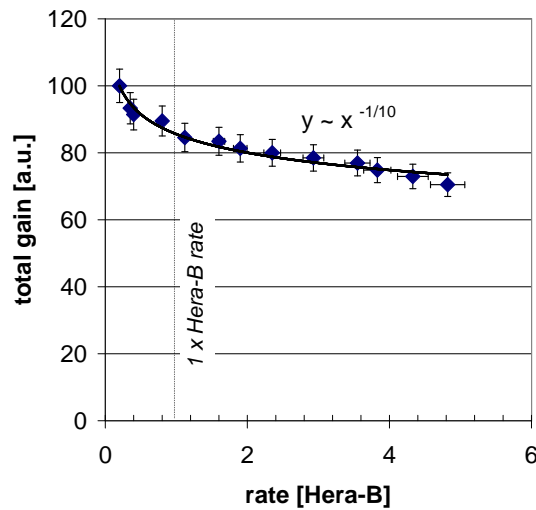
Figure 6.22: Rate dependence in the regime of Hera-B conditions (after equivalent irradiation dose of 6 years of Hera-B operation). The experimental data points are fitted by a potential law with a good correlation ($R^2 = 0.9$)

Evolution of the gas amplification

In figure 6.23 the evolution of the gas amplification factor of both, the ^{55}Fe- and X-ray-pulses are shown, demonstrating that the gain increased rapidly during the first year of irradiation.

Moreover, since the X-ray pulse-height was recorded at a rate equivalent to 20× Hera-B load whereas the ^{55}Fe-source provided only about one forth of the Hera-B rate, the ratio of the X-ray- and the ^{55}Fe-pulse-height changes in time. As soon as the gain becomes rate dependent, the ratio of both quantities, which is supposed to be constant ($r = \frac{E_{\gamma-Cu}}{E_{\gamma-Fe}} = \frac{8keV}{5.9keV} = 1.35$) under normal conditions, starts to decrease. This effect is a consequence of an over proportional gain increase for small rates.
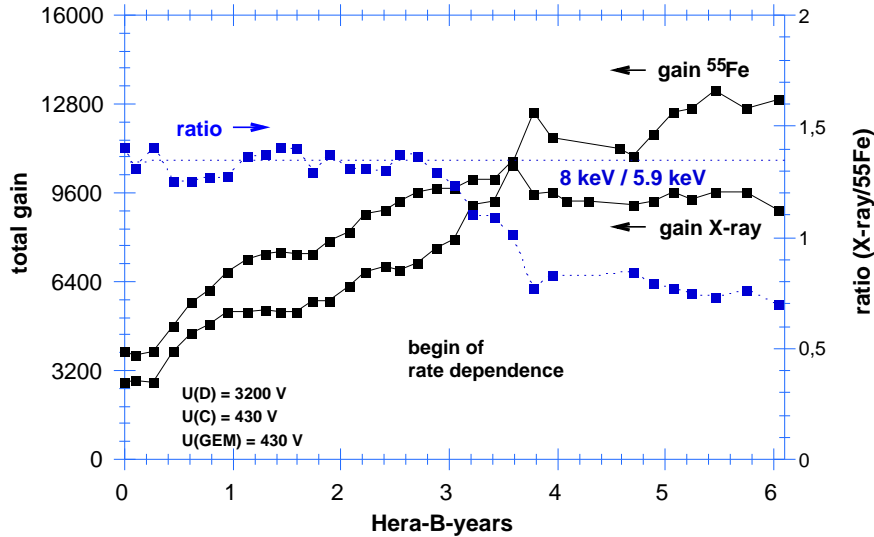
Figure 6.23: Development of the Gain: ^{55}Fe- and X-ray-pulse-height and ratio plotted as a function of irradiation time.

Efficiency

This relative measurement fundamentally relies on a precise detection of the counting rate of a ^{55}Fe-source as a function of time, while keeping all other parameters constant. In this condition, a drop in relative efficiency is reflected by a decrease of the detected ^{55}Fe-rate.

But instead of simply counting "pulses over threshold" — a method very susceptible to external noise — a more reliable way was chosen:
A discriminator threshold was set well-above the noise level, and kept constant during the entire experiment. First, the cathode voltage was reduced down to a value, where the detected counting rate is negligible. Next, the efficiency, represented by the "counts over threshold", was measured as a function of the cathode voltages. Two parameters, the number of counts and the detector gain, were determined for every step and compared to the results from previous days and to the original efficiency.

When the detector is irradiated by monoenergetic source (e.g. ^{55}Fe), the shape of the function "counting rate of versus cathode voltage" is characterized by two prominent steps: the first increase in counting rate appears, when the cathode voltage (and thus the gain) is large enough for the pulses of the ^{55}Fe-peak to exceed the threshold value. The second step appears, when the escape-peak exceeds this value. The experimental findings are depicted in figure 6.24.
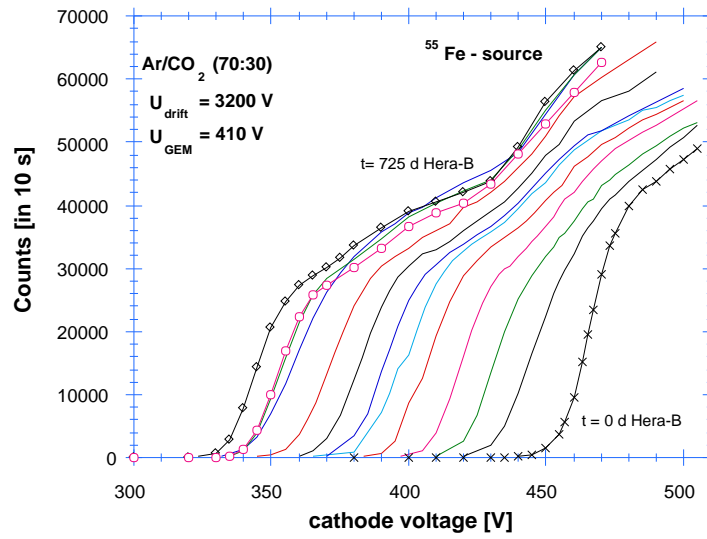
Figure 6.24: The ^{55}Fe count rate as a function of the cathode voltage. For each efficiency measurement, the number of detected pulses over threshold is plotted versus the cathode voltage.

Next, the derivative with respect to the cathode voltage was determined and plotted (see figure 6.25), showing a kind of "reversed pulse-height spectrum". This procedure gives the *additional number* of pulses exceeding the discriminator threshold value, when the cathode voltage is increased. It is "reversed" since the pulses with the largest energy are counted for the lowest cathode voltages and vice versa. For the evaluation of the detector efficiency
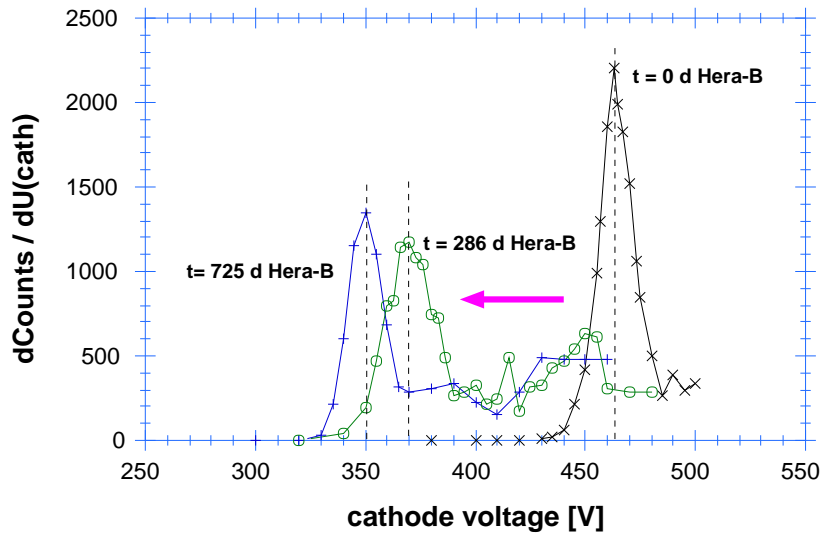
Figure 6.25: Derivative of the plot "counts versus cathode voltage" with respect to the cathode voltage, reflecting a kind of "reversed pulse-height spectra". The peak, clearly correlated to the ^{55}Fe-Peak, moves towards smaller cathode voltages during the ageing process. This is a clear evidence for an increasing gain.

as function of the irradiated dose, the counts in the first peak (^{55}Fe-peak) of the reversed pulse-height spectrum were integrated. Since the peak was not very prominent especially at the end of phase 1, only the first half of the peak was taken into account in order to separate pulses from the escape-peak. The results in figure 6.26 clearly show that the efficiency was constant within the error bars, although the gas amplification changed by a factor of 4.
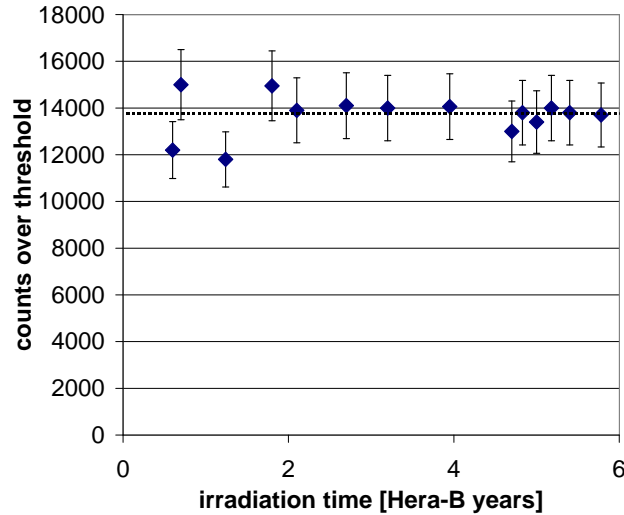
Figure 6.26: For the efficiency of the chamber the number of counts in the first peak are plotted versus time. The efficiency is found to remain constant.

Sparking Probability

As described in section 5.3, one important input parameter for the spark tendency between anodes and cathodes is the electric field. In contrast to the process of gas amplification, where only the field *very close to the anodes* affects the gas gain, the discharge rate is strongly influenced by the field *in the gap between the anodes and cathodes*. In figure 6.15 it is depicted, that this field is reduced as a consequence of the diamond ageing process. However, since anode-cathode discharges are very rare for GEM-MSGCs anyway, it was not possible to experimentally prove a reduced spark tendency within this measurement.

6.2.4   Chemical structure of the diamond coating

Diamond ageing was exclusively observed in MSGCs with a coating layer manufactured by the Fraunhofer Institut [61]. MSGCs, covered by coating made by Surmet [86] were free of effects of diamond ageing, although being irradiated for comparable time scales.

    The chemical composition of both diamond layers is identical (C: 50 at%, N: 22 at%, H: 15 at% and Si: 13 at%); nevertheless, the structure in molecular level can be very different. It was observed in the currents between anodes and cathodes, that the resistivity of the Surmet coating is significantly higher compared to the Fraunhofer layer.

    Unfortunately it was impossible to change the supplier of the coating layer for the mass production of the Hera-B detectors, since all glass substrates have already been coated and

also the electrode strips have already been manufactured, when the phenomenon of diamond ageing first appeared.

However, in order to test the relevance of the internal structure, we changed the resistivity of the Fraunhofer coating by heating the wafer for approximately 10 h at 200 °C. The resistivity after heating was determined to be in the order of $2 \cdot 10^{15} \Omega/\square$, which is equivalent to an increase of roughly one order of magnitude.

When comparing the results after intense X-ray irradiation for the heated and non-heated wafer, the process was found to be slowed down. First effects for a gain increase and a deterioration of the energy resolution were observed after about 2.5 Hera-B years for the low resistivity MSGC, whereas an irradiation dose equivalent to more than 3.5 years of Hera-B operation was required for the high resistivity wafer. In order to prevent or at least to slow down the diamond ageing process, a large fraction of the MSGC wafers for Hera-B were heated before mounting, in order to enlarge the resistivity against etching. Nevertheless, diamond ageing could not be completely excluded. Possibly, an intensified heat treatment could further improve the resistance against diamond ageing.

6.2.5 Conclusions

As it cannot be assumed that (i) the diamond ageing process depends linearly on the irradiation rate and (ii) the damage due to X-ray irradiation is — for a given irradiation dose — equivalent to the one in hadronic beams, the results from this study have to be transfered to the Hera-B conditions with great care. However, since the irradiation rates and the damage to the material were significantly higher during the X-ray tests, the results can be assumed as a conservative approximation of the real conditions.

In general, a loss of energy resolution is not a severe problem for a tracking detector, since only the "signal over threshold" is an important parameter. Therefore, the detector can be operated in all phases, as a long as the detection efficiency is not affected.

Nevertheless, in case that diamond ageing will be observed during Hera-B operation, the gas amplification in phase 2 and 3 cannot be adjusted to the original values by lowering the cathode voltages for two reasons:

- It has to be taken into account, that due to variations of the irradiation rates across the chambers not all parts of the chamber will reach the high-gain-phase (phase 3) at the same time.

- Resulting from the rate dependence of the gain after diamond aging, the rate variations along the chamber causes varying gains along the anode strips.

As a consequence, the detector gain is expected to be locally very inhomogeneous. A *reduced* cathode voltages would decrease the efficiency of the "low-rate-regions" significantly; a *high* voltage in combination with a very inhomogeneous gain may lead to trigger problems. Therefore, the trigger threshold has to be optimized in a way that, on one hand, the efficiency is high and, on the other, events with a large gain are not triggered twice.

Chapter 7

Final beam test

The beam test in April 1999, in the hadronic environment at PSI, was considered as the final test, before the mass production of the inner-tracker system for the HERA-B experiment was restarted. In the focus of interest were especially possible effects due to the change of the counting gas from Ar/DME (50:50) to Ar/CO_2 (70:30). The decision of changing gases was a consequence of severe gas ageing problems (see section 6.1) and the loss of mechanical tension of the GEM when exposed to DME. As often proved in the past years of development, reliable tests could only be performed in conditions close to the real ones.

7.1 The objects of the measurement

Compared to the Hera-B conditions, the PSI proton was suitable to accelerate the operation by a factor of up to 30. In consideration of the results from the extended studies in the lab, the operation parameters were optimized with regard to ageing and discharging (see also scheme in figure 7.1) of any kind:

(i) Anode-cathode Sparks

As described in section 5.3, anode-cathode discharges (sparks) can easily destroy the MSGC structure within hours. From previous beam tests at the PSI and in the Hera beam a reliable operation could be guaranteed, when using a GEM as an additional amplification step. The cathode voltage could be reduced significantly, thus resulting in an effectively reduced discharge rate.

Nevertheless, the regime of safe operation is drastically reduced in Ar/CO_2 compared to Ar-DME; mainly, due to a less effective quenching behavior of CO_2. As shown e. g. in figure 5.4, the spark rate for Ar/CO_2 is significantly higher compared to Ar/DME. In a combined system of MSGC and GEM, a reduced discharge resistivity was expected for Ar/CO_2, hopefully being sufficient for a reliable operation in hadron beams. In order to be on the safe side, the MSGC amplification factor and therefore the cathode voltage was reduced to the lowest possible level.

(ii) GEM and multiple-electrode discharges

Since a *total* gain of at least 4,000 is required for a sufficient efficiency in Hera-B, the GEM amplification had to be adjusted for a compensation of the reduced gain at the MSGC. However, the rate of GEM-discharges induced in hadron beams strongly increases as a function

Parameters: **Consequences:**
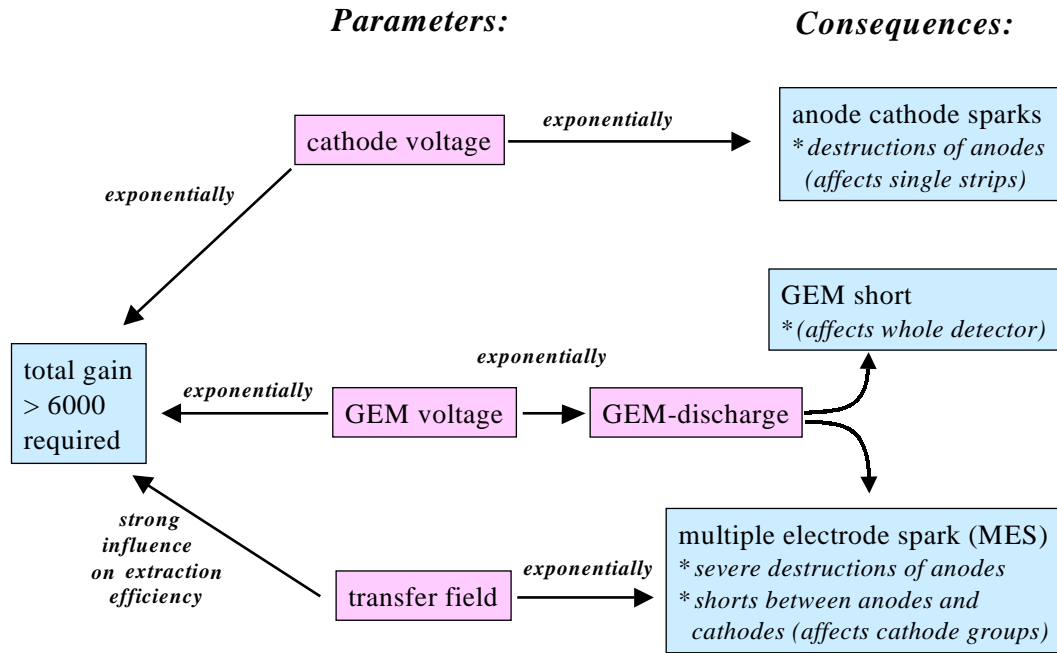
Figure 7.1: Scheme of the parameters influencing the discharge process during operation in hadronic environment: The required total gain of approximately 6000 is influenced by the cathode voltage, the GEM voltage and the transfer field, which all also influence the discharge rate.

of the applied GEM-voltage. From Raether's law it follows that the probability of initiating a streamer depends on the amount of primary ionization, which is significantly increased in hadron beams compared to X-ray beams due to the spallation products.

An increased GEM-spark rate is known to have two negative side effects:

- **GEM shorts**
  Permanent GEM discharges may lead to GEM shorts. If the GEM cannot be "re-animated" by intense current or voltage pulses, the entire detector — and not only a few channels — is completely destroyed. Since the GEM discharge rate in hadronic beams is correlated to the applied GEM voltage, there is a clear upper limit for the maximal tolerable GEM-voltage and — as a consequence — also for the maximal GEM-gain.

- **increased number of MES discharges**
  GEM discharges are known to be a necessary — however not sufficient — condition for the creation of multiple electrode sparks, which result in severe damages in the MSGC-structure and the coating layer. When the number of discharges at the GEM can be kept on a low level, the occurrence of MES is sufficiently low.

However, GEM-discharges cannot be completely excluded for 200 detectors during 3 years of operation at Hera-B, due to the fact that not all of them are of same excellent quality. Therefore, (i) the GEM gain has to be limited to values below 100 to reduce the discharge rate and (ii) the probability for a spark propagation from GEM towards the MSGC structure has to be excluded with a sufficiently large safety margin.

It was stated in chapter 5.4, that this probability is mainly determined by the amount of extracted charge during the GEM discharge, on one hand, and by the field conditions in the region, where the streamer propagates, on the other. A segmentation of the GEM in sufficiently small parts for a charge reduction is not practicable because of the large number of additional HV-channels and the huge amount of extra material; only the number of extra cables in the active detector region would significantly increase the counting rates due to multiple scattering.

As a result of the PSI test in 1998 we found that there are operation conditions with low transfer fields ($E_{\text{trans}} < 5$ kV/cm), where the MES rate is negligible. The optimum between low sparking probability (where low transfer fields are required) and an acceptable electron drift velocity (where high drift- and transfer fields are necessary), was found to be 5 kV/cm in Ar/DME (50:50) (results see figure 5.17). This test had to be repeated for Ar/CO_2 (70:30) and the results are presented here.

(iii) Gas ageing

It was shown in various longterm tests in the lab under high-rate X-ray irradiation, that gas ageing does not occur when replacing Ar/DME by an Ar/CO_2 mixture. It had to be confirmed that this result holds for hadronic beams. But since the time scales of the gas ageing process are usually too long, a beam test in "real conditions" is excluded for principle reasons. Nevertheless, the highest possible dose in the given time was accumulated during this test, resulting in an irradiation dose equivalent to 0.3 years of Hera-B operation.

(iv) Diamond ageing

Resulting from the X-ray studies in the lab, diamond ageing is supposed to appear after irradiation doses equivalent to some years of Hera-B operation. Diamond ageing is an effect of very large time scales, and therefore two weeks of irradiation at the PSI beam with "accelerated irradiation" can only give a lower limit for the minimal timescale without diamond ageing. Nevertheless, since the etching process is induced by the avalanching process, no significant dependencies from the type of irradiation (X-ray compared to MIPs) was expected at all. In subject of diamond ageing, Ar/CO_2 is for sure not the worst choice, as proven in the measurements in the lab.

7.2   Test set-up

The beam was shared between four different LHCb inner tracker groups and the Hera-B inner tracker group (see figure 7.2). Due to the different purposes of measurement, two different beam conditions were chosen:

- Day-time:
  π^+ with low rates (up to 100 Hz/mm^2) for signal and efficiency studies for the LHCb detectors. This rate was orders of magnitude too small for the Hera-B studies, therefore the GEM-MSGCs were switched off during day time.

- Night-time:
  80 % protons and 20 % π^+ with high rates (up to 60 kHz/mm^2) for ageing studies and optimization of chamber parameters for the HERA-B detector.

Starting with the two GEM-MSGCs for the HERA-B experiment, all detectors were in one line (see figure 7.2): the Lausanne Micromegas, the two finger szintillators on a two dimensional step-motor for monitoring the beam profile, the Micro Wire Detector from Santiago and, in the end, the two Triple-GEM-detectors, one from St. Petersburg and the other one from the Heidelberg Institute. Figure 7.3 represents the beam rate scans for both directions. The beam
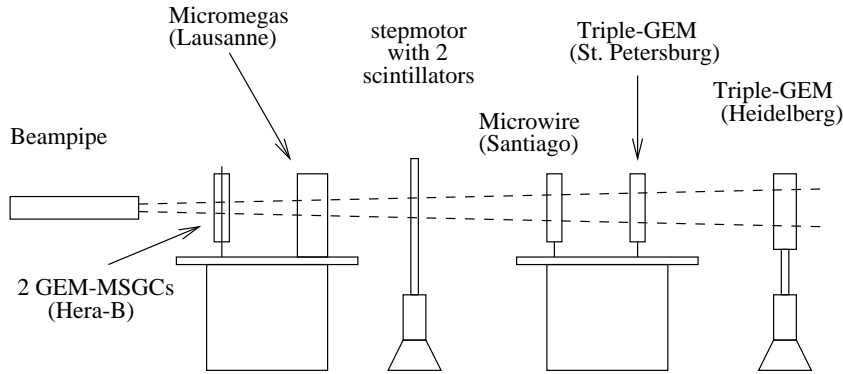
Figure 7.2: The experimental setup in the beam test at PSI.

shape is nearly Gaussian, but the width in y-direction (along the strips) is about 50% larger than in x-direction. Both scans were done with the proton settings (momentum: p = 350 MeV/c) for the night measurements.
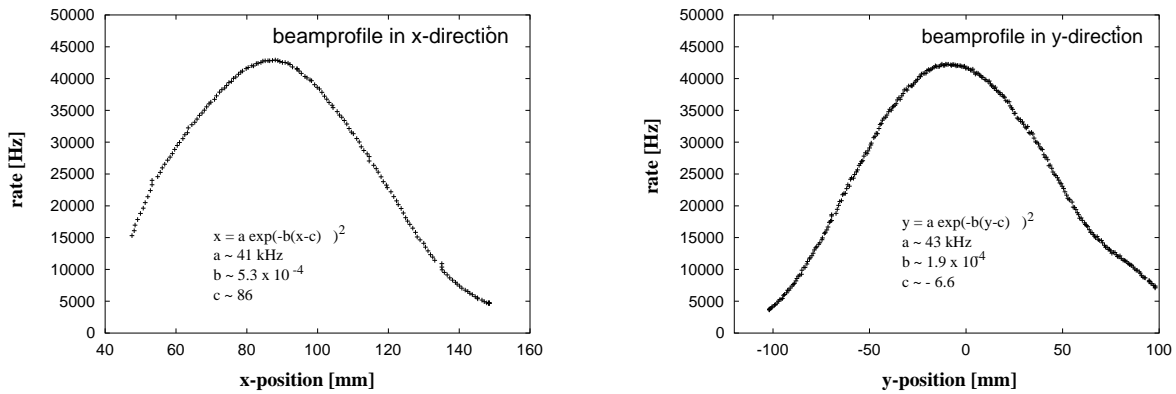
(a) Scan in x-direction at y = −7mm

(b) Scan in y-direction at x = 85mm

Figure 7.3: Rate scan for the proton beam in the $\pi M1$-area at PSI.

Irradiation time

The HERA-B chambers were irradiated on four positions, as visualized in figure 7.4. For calculating the equivalent HERA-B radiation dose, we included the fact that protons in this energy range have a 5 times higher value for the primary ionization compared to MIPs. At position 1, we achieved a charge accumulation equivalent to 1/3 HERA-B year. Position

3 and 3a was chosen in order to investigate possible effects of an irradiation of the outer segments of the detector, including the frames. Here, we accumulated an irradiation dose equivalent to 210 h of Hera-B operation. During some tests for the LHCb detectors at higher rates, the Hera-B detectors were irradiated at position 2 and 4, altogether for 250 h and 90 h respectively. None of these irradiation periods is of course sufficient for an extrapolation of the situation for 3 Hera-B years. However, the operation stability, which is mainly given by the irradiation rate, and very fast ageing processes could be studied in a "real conditions" environment.
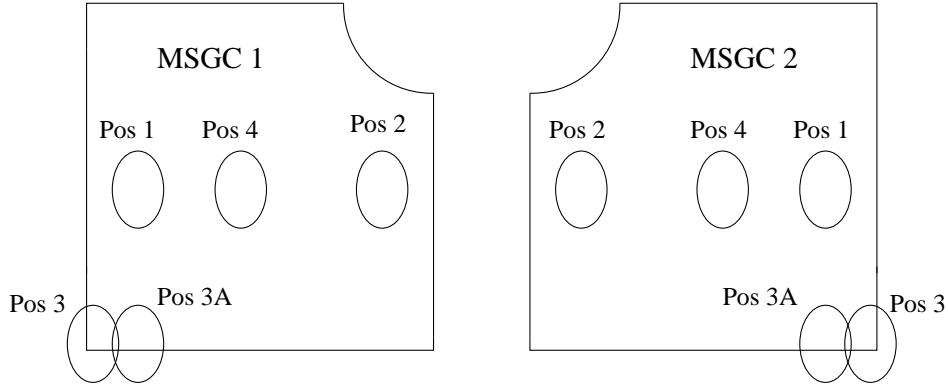
Figure 7.4: The irradiation positions of the two Hera-B GEM-MSGCs.

Monitoring and controlling parameters

The chambers were irradiated with constant high proton rates. The detector currents (cathode, GEM_{upper}, drift) were monitored and electronically stored. From changes in the detector currents — for constant irradiation rates — diamond ageing (increasing currents) and also gas ageing (decreasing currents) can be easily detected. The case of an exact neutralization of both effects is supposed to be rather unlikely.

Diamond ageing can also be detected from the pulse-height spectra, as broadening spectra as well as an increasing gain gives clear evidence for the appearance of diamond ageing. Since the Landau spectrum of the MIPs from the beam is not very revealing, pulse height spectra with a ^{55}Fe γ-source should give a more detailed view on possible changes. The source was placed on the detector after the periods of intense irradiation. For sufficient rates, the drift electrode was replaced by a thin mylar foil in some parts, as depicted in figure 7.5. Anode-cathode sparks are known to occur as peaks in the cathode currents. In principle, the current measurement method does not allow for a quantitative measurement, since spikes in the current may be lost due to the rather low sampling rate of the current meters, which are clearly not designed for this purpose. A more precise technique of a spark detection is usually realized by pick-up electrodes. But due to an excessive number of pick-up signals from other set-ups (especially the Micromegas Detectors), we couldn't make use of our spark detection.

Also MES can be detected as spikes in the detector currents. In this case, also $I_{GEMupper}$ and I_{drift} are affected. In some cases, also shorts between anodes and cathodes are a consequence.
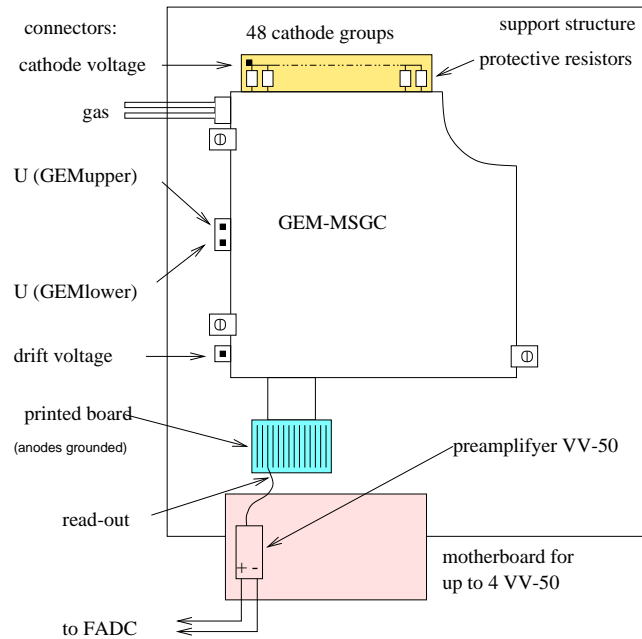
Figure 7.5: The experimental setup for the GEM-MSGCs.

7.3   Beam test results

During the first night of intensive irradiation, the gas gain increased within 90 minutes by almost 30 %, as shown in figure 7.6. This behavior is caused by polarization and charging effects in the kapton layer of the GEM-foil, thus affecting the GEM-gain significantly. After the first hours of operation, the gain stabilizes, and during the following irradiation periods this effect was much less prominent. Only when the GEM voltage is reduced to zero for long periods, the polarization can be neutralized. In general, beam losses are reflected by jumps in the detector currents. The cathode currents go back to the nominal current, given by the resistivity between anodes and cathodes, whereas all other currents go down to zero. The short-term variations in gain of about 5 % are induced by the voltage controlling mechanism of the GVB (c. f. Appendix A).

(i) Anode-cathode sparks

A total gain of approximately 8,000 was chosen for all irradiation periods in order to have a sufficient gain reserve for the longterm operation in Hera-B. Figure 7.6 and 7.7 illustrate, that in case of high cathode voltage and low GEM voltage several anode-cathode sparks (reflected by the spikes in current) were detected. However, in conditions with a lowered cathode voltages and a slightly increased GEM voltage no more discharging was detected, as shown in figure 7.8.

Please note that in figure 7.6 the cathode current in the reference detector ("cathode 2"), operated under the same conditions, was stable. It was often observed that all detectors are individuums and their behavior (gain, discharge rate) is slightly different. Also for this reason, a large gain reserve is strongly requested.

The settings with a reduced cathode voltage were chosen for the rest of the time, and
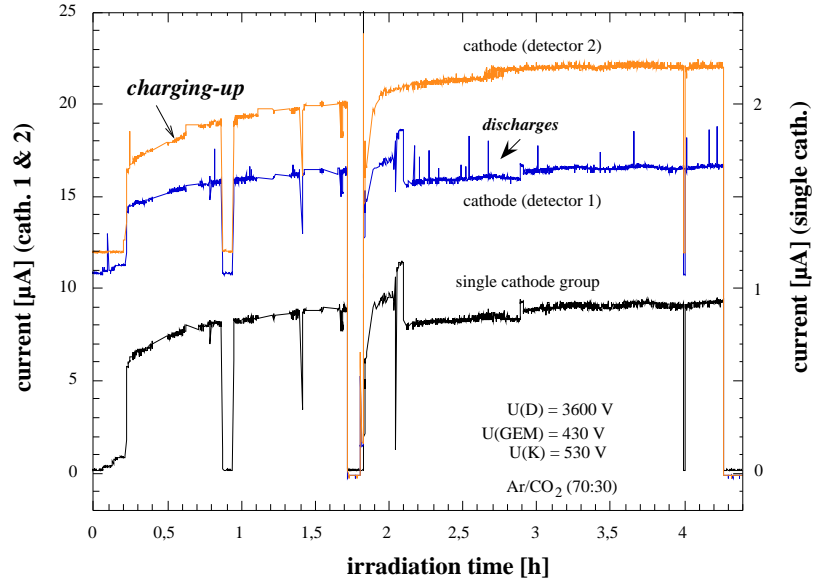
Figure 7.6: *Polarization and charging-up effects during the first hours of operation. Within 90 minutes, the GEM gain increased by about 30 %.*
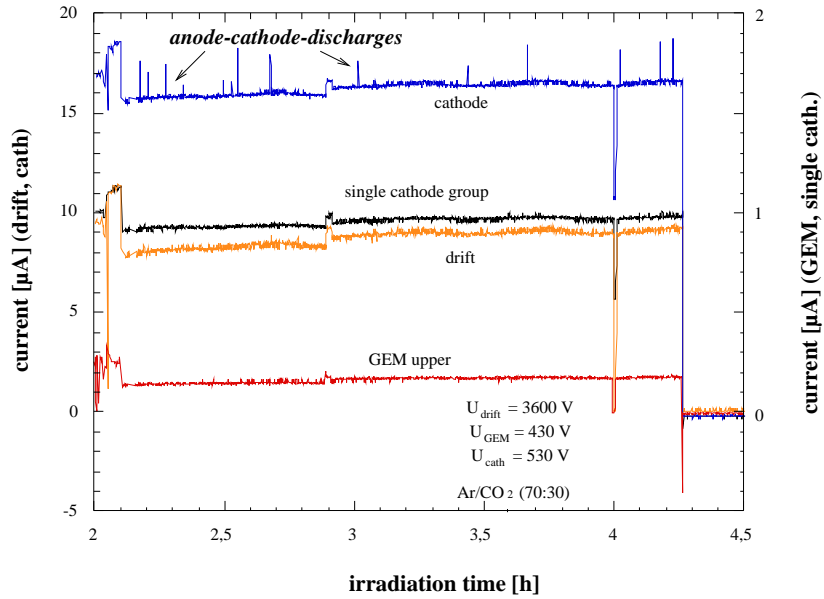
Figure 7.7: *GEM-MSGC operation in Ar/CO_2, voltage settings: $U_{drift} = 3600$ V, $U_{GEM} = 430$ V, $U_{cath} = 530$ V.*

indeed no further anode-cathode discharges were observed. By comparing these results to previous PSI tests with Ar/DME as counting gas, it has to be concluded, that the safety margin in hadronic beams with respect to anode-cathode discharges is significantly reduced in Ar/CO_2. However, stable conditions for high gain operation (8,000) in Ar/CO_2 can be found.
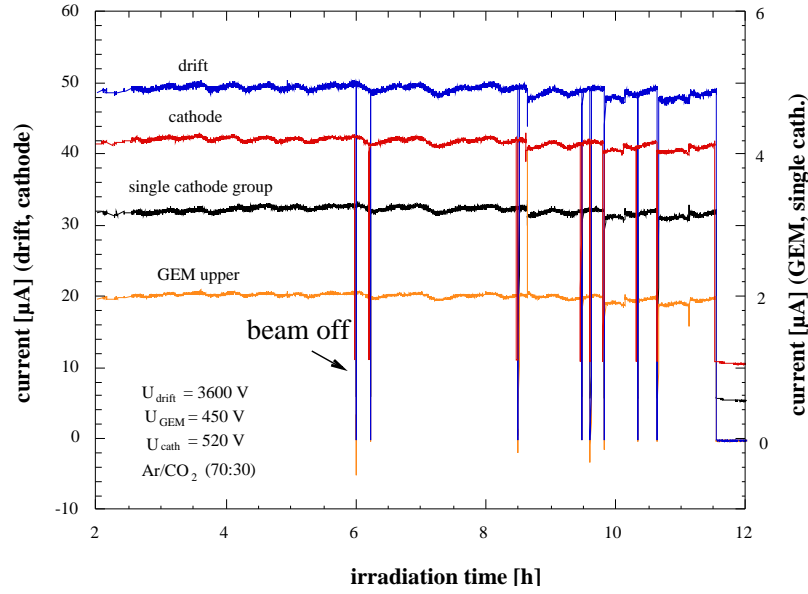
Figure 7.8:   Safe GEM-MSGC operation in Ar/CO_2 at reduced cathode voltages: $U_{drift} = 3600$ V, $U_{GEM} = 450$ V, $U_{cath} = 520$ V

(ii) Multiple-Electrode Sparks

As expected, multiple-electrode-sparks (MES) were exclusively observed, when high transfer fields ($E_{trans} > 5.2$ kV/cm) where applied. One example is given in figure 7.9; a spike is clearly visible in all currents, but without short-circuiting bridge between anodes and cathodes in this case. In the end, two shorts were observed during this beam test. After about half of the total irradiation dose was accumulated, the transfer field was reduced by 10 % to a value of 4.8 kV/cm, leading to stable operation without any sparks. Also in case of MES, the regime of safe operation is reduced compared to Ar/DME. But as the drift velocities in Ar/CO_2 are higher compared to Ar/DME, a lower transfer field can be accepted without increasing the ballistic deficit of the signal. Since the outer segments of the MSGCs are very critical in point of GEM discharges, the operation stability of the GEM-MSGC was investigated by a high-rate irradiation of the area in the vicinity of the frames (position 3, see figure 7.4). For identical detector conditions (namely gain, voltages and rate) the operation safety was found to be equivalent.

(iii) Gas ageing

The effect of gas ageing in Ar/DME was observed during the beam test in October 1998 after one night of irradiation only. In contrast, after an accumulated dose equivalent to 1/3 HERA-B year, there was no sign of gas ageing in Ar/CO_2. In all night measurements, the currents where extremely stable with regard to slow changes. The only exception are the first few hours of operation during first night of high rate irradiation, as shown in figure 7.6, when a slow increase of all currents was observed, caused by the typical polarization effects in the GEM foil.
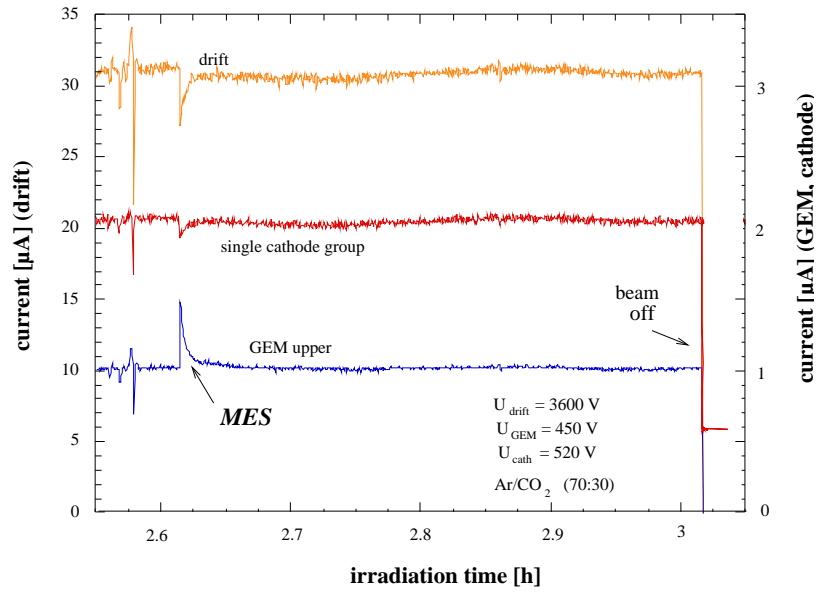
Figure 7.9: Multiple-electrode spark at t=2.65 h, characterized by spikes in all detector currents; no short between anodes and cathodes.

(iv) Diamond ageing

The first hints for diamond ageing are rising gains and a loss of energy resolution. A comparison of spectra in the very beginning to those of the very end of this beam test (1/3 HERA-B year, figure 7.10) demonstrate that shape of the pulse-height spectrum has not changed. Resulting from this observation, it can be concluded that the changes in the diamond coating are not significantly faster in hadron beams compared to X-rays.
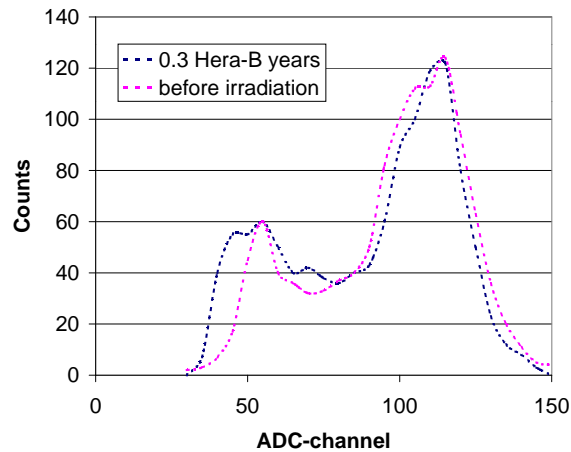
Figure 7.10: Comparison of ^{55}Fe-spectrum before and after irradiation at the PSI-beam.

7.4   Conclusions

By the final operation test it could be corroborated, that the gas ageing problem previously observed in Ar/DME is not existing in the Ar/CO_2 mixture. Although the safety margin with regard to discharges is reduced compared to Ar/DME, it is nevertheless possible to achieve safe and stable operation at high gains (8,000), even in intense hadron beams. It is strongly recommended to use low cathode voltages and transfer fields, but high GEM voltages for a sufficient gain. Of course also the GEM gain is limited due to the coupling of the number of GEM discharges to the GEM voltage.

The irradiation time was too small to check the long time scale of the changes in diamond coating, but it could be proved, that there are still good spectra after 1/3 HERA-B year of operation.

Chapter 8

Summary and Outlook

The new generation of high energy experiments demands for new concepts of tracking detectors in many ways. The readout time, defined by the bunch-crossing rate, is in the order of 100 ns (for the Hera experiments) or even below (20 ns for the LHC experiments). As the acceleration energy increases, more and more decay channels are energetically accessible and thus the number of decay products per collision dramatically increases. The detector size steadily increases and thus the number of readout channels. This whole evolution not only asks for high-tech electronics, efficient trigger software and intelligent analysis tools, it also severely taxes the detector hardware. The detectors have to provide a very high granularity (for a good spatial resolution and for a sufficiently low occupancy), they have to be extremely fast (to reduce the readout time), their radiation length has to be large (in order to avoid multiple scattering) and — last but not least — they have to be extremely radiation hard. One possible approach are the newly developed Micro Pattern Gas Detectors, for example the Micro Strip Gas Chambers (MSGC), for a reliable operation in hadronic beams equipped with a Gas Electron Multiplier (GEM).

These GEMs, originally developed as a preamplification device for MSGCs only, became very common for a wide range of applications, mainly because of two features: First, they can be coupled to any other gaseous detector, thus allowing for a safe operation at high gain. Second, they effectively shield the back-drifting ions.

A good knowledge of the electron transfer in the GEM is of fundamental interest mainly for applications, where single electrons have to be detected; however, also for optimization of the operation in high energy experiments this parameter is important. The principles of the electron transfer through the GEM were studied within this work and the results are presented in chapter 2.

In the focus of interest was the *transfer efficiency*, i.e. the fraction of the electrons deposited in the gap above the GEM which are entering into the GEM holes and experience multiplication. This parameter was studied by a new method, relying on pulse counting. The outcome may be summarized as follows:

- The transfer efficiency is strongly affected by the transverse diffusion of the electrons, drifting under the focusing field towards the GEM aperture. Especially for very low drift fields the transfer efficiency is significantly reduced. In these conditions, dominated by a high electron diffusion, the "ability" for electrons to follow the perfectly focused field lines is poor.

- In the case of a slightly increased drift field, a maximum in the transfer efficiency can

137

be found for any gas pressure and type. In this range, the electrons are well focused into the GEM apertures. The maximum, however, is not necessarily equal to 100%, its value depends on the GEM geometry and gain.

- Further increasing the drift field invariably leads to a loss of efficiency due to loss of field line focusing.

- The transfer efficiency increases roughly exponentially with respect to the GEM-voltage, reflecting a significantly improved field-line focusing.

- The transfer field in the gap following the GEM has a minor influence on the transfer efficiency.

The detection efficiency for single electrons can be significantly increased by moderately amplifying the initially deposited single electrons, prior to their collection and multiplication by the GEM. The probability to have at least one of the secondary electrons entering the GEM aperture invariably reaches 100%, if the electron transverse diffusion satisfies the condition that the lateral spread of the electron cloud exceeds the GEM-pitch. This spread depends on the transverse diffusion and thus on the gas type, the drift field and the drift length. A simple statistical model successfully explains the results. The details are described in chapter 3.

In the second part of this work, the problems encountering during the development of the inner tracking system for the Hera-B experiment are presented.

- The original design was a conventional MSGC. For this concept, it turned out that a safe operation at sufficient gain could not be guaranteed in hadronic beams. *Anode-cathode discharges*, induced by highly ionizing particles, lead to severe destructions of MSGC electrodes. Systematic studies in the lab proved that this problem is intrinsic for the concept of gas amplification by microstructures: for a given detector geometry and counting gas, the gas amplification and the discharge probability are correlated, meaning that for a required gas gain the discharge rate can hardly be influenced. The problem is relevant for most Micro Pattern Gas Detector concepts as the short distances between anodes and cathodes are often not separated by sufficiently low fields in order to effectively quench the propagating streamer.

  The way out came by the introduction of the Gas Electron Multiplier (GEM) in the Hera-B detector design. By splitting the total gas amplification into two spatially separated steps, the discharge probability for anode-cathode discharges could be reduced by several orders of magnitude.

- The operation of GEMs in combination with MSGCs was not free of problems. Although the GEM device turned out to be much more robust compared to MSGCs, in some very rare cases discharges between the upper and lower GEM side led to severe destructions, i. e. shorts.

  In addition, GEM discharges tend to propagate towards other electrodes. In the MSGC this was found to be fatal for the fragile electrode structure. It turned out that similar to the anode-cathode discharge phenomenon, also here a region of low fields is strongly required in order to quench the *propagating streamer*. Conditions have been found allowing for a stable and spark-free operation even in a high-rate hadronic beam. The

details of the discharge study (anode-cathode discharges and propagating GEM-sparks) are given in chapter 5.

- Apart from the operation stability in a high rate environment, also the longterm stability of the GEM-MSGC detector was carefully investigated. *Gas ageing* could be effectively excluded during the research and development phase, due to a careful choice of the gas and the detector and gas system materials. Although nothing was changed in terms of materials and operation conditions, the first main series detectors strongly suffered from gas ageing problems, when operated in a high rate test beam. Only by replacing the counting gas Ar/DME (50:50) by the mixture Ar/CO$_2$ (70:30), a stable longterm operation even in high rate beams could be guaranteed (chapter 6).

- The *diamond ageing*, affecting the MSGC concept only, is characterized by an increasing gain after long-term operation. The diamond coating layer, introduced in order to reduce charging-up effects in the vicinity of the MSGC electrodes, turned out to be damaged by the continuous avalanching process. Although the character of the gas amplification was found to change significantly after several years of operation in Hera-B conditions, no gain or efficiency losses were found. The ageing study (gas ageing and diamond ageing) can be found in chapter 6.

- As one of the most important results of our study it turned out to be extremely important to test the detectors in conditions as close as possible to the "real" conditions, as most of the various problems could not be detected in a simple high rate X-ray beam but only in hadronic beams. In chapter 7 results from the final test of the full-size Hera-B GEM-MSGC in a high rate proton beam (Paul-Scherrer Institut, Switzerland) are presented. It was proven that this detector can be reliably operated at a total gain of 8,000 in a hadronic beam, with a charge deposition one order of magnitude higher compared to Hera-B conditions. However, the gain reserve for the onset of anode-cathode discharges, conventional GEM discharges and propagating GEM-discharges is clearly limited and all operation voltages have to be carefully balanced for a safe operation.

  Gas and diamond ageing could be excluded during this beam test; however, the total irradiation dose was equivalent to 1/3 year of Hera-B operation only. Longterm high rate test with X-rays were performed in the lab, proving that a operation for several years is possible without any gain loss due to gas ageing. Diamond ageing can not be avoided, but the changes are extremely slow and only minimally affecting the required detector performance.

The results of this intense studies led to the conclusion that a reliable operation can be guaranteed for the whole measurement time of the Hera-B experiment, when all operation parameters are carefully optimized. Due to strong limitations for almost all parameters, the "phase space" of stable and reliable operation is however small, not providing much gain reserves.

Nevertheless, the enthusiasm for other applications as tracking detectors in high energy physics experiments ceased after several severe setbacks, mainly discovered during the development of the Hera-B detectors. The trend for tracking detectors dissociates from the basic MSGC principle. Remaining options for gas detectors are either to live with discharges and to built very robust devices (micromegas) or to separate the total amplification into two or even more steps (multiple GEM solutions).

However, Micro-Pattern-Gas-Detectors are very promising devices for many applications in other fields apart from high energy physics experiments. They provide an excellent spacial and temporal resolution for particle detection and can be used to cover large areas, being comparatively cheap and robust at the same time. Especially for medical, biological or astrophysical applications, e. g. in the field of radiation detection, these gas detectors can be the detectors of choice in the near future [38, 87].

Appendix A

Discharge recognition and GEM-voltage-box

A.1 General operation mode

In the inner tracking system of the Hera-B detector roughly 200 GEM-MSGCs have to be operated simultaneously. In order to reduce the number of power supplies, the two GEM voltages of each detector are generated from the drift voltage by a resistive voltage divider with an active internal controlling. This GEM-voltage-box (GVB) [67] can supply 8 GEM-MSGCs with only one input voltage (U_{drift}). The 8×2 output channels (U_{GEMupper} and U_{GEMlower} for 8 GEM-MSGCs) can be individually monitored and adjusted. The strict coupling of the three channels ($U_{\mathrm{drift}}, U_{\mathrm{GEMupper}}, U_{\mathrm{GEMlower}}$) gives the additional security that in case of an accident, all three channels are grounded at the same time. This concept is very important in order to protect the fragile GEM-foil from overvoltage.

The operation mode of the GVB is given in the simplified schematic circuit diagram in figure A.1. The middle potential of the two GEM-voltages (defined by the two series resistors of 20 and 25 MΩ respectively) is chosen in a way, that the GEM-foil experience the lowest possible electrostatic force in the GEM-MSGC. Due to the geometry of the Hera-B detectors, a middle potential of $0.53 \times U_{\mathrm{drift}}$ is required.

An embedded microprocessor ("controller") is regulating all GEM-voltages in one box. For each channel, both output channels are continuously monitored and the resulting GEM-voltage ($U_{\mathrm{GEM}} = U_{\mathrm{GEMupper}} - U_{\mathrm{GEMlower}}$) is evaluated. A transistor-optocopler combination in the resistor chain acts like a variable resistor (in a range of 1–10 MΩ) and therefore influences the output voltages within a certain range. The GEM-voltage can be set from the controller through a DAC. In order to compensate for small deviations from the desired GEM voltage, this DAC value is monitored in a fast software loop. All values are downloaded from external via serial interfaces like R232 or the CAN-bus.

This method of an active voltage controlling provides the opportunity to operate GEM detectors at a stable gas gain even in experiments with strongly varying particle fluxes, since the GEM voltage can be adapted to any external situation. In case of no internal detector currents (no beam or no cathode voltage), the DAC-value can be directly translated into GEM-voltages.
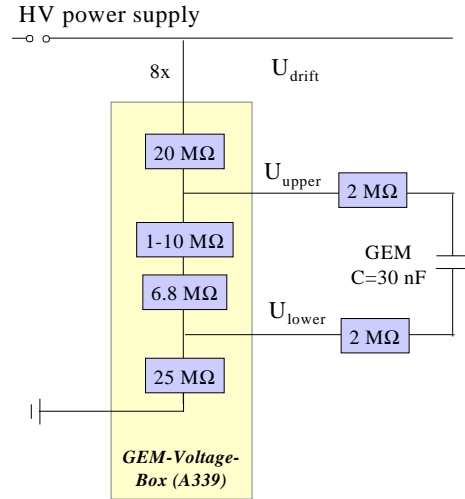
Figure A.1: A simplified schematic circuit diagram of the GVB. From the input voltage U_{drift} the 8×2 other voltages ($U_{GEMupper}$ and $U_{GEMlower}$) are created by an resistive voltage divider. The 6.8 MΩ serial and 1–10 MΩ variable resistor define the GEM voltage. The GEM-MSGC is protected against external noise and discharging by 2 MΩ resistors. The GEM capacitance is 30 nF.

A.2   GEM spark detection

Since GEM discharges — or even worse multiple electrode sparks — may lead to severe destructions in the detector, discharging has to be reliably detected, counted, and in case of very unstable conditions, the detector has to be switched off in a controlled way. The monitoring of the GEM potentials provides a very simple, but powerful tool for a spark recognition during operation.

Since the GEM-capacity of $C \approx 30$ nF is completely discharged as a consequence of the GEM spark, the potentials of the two GEM channels experience a significant voltage drop. Although the GVB and the GEM are separated by protection resistors (2 MΩ), this drop is nevertheless detectable inside the GVB. The recovery time ($\tau = R_{\mathrm{GEM}} \times C_{\mathrm{GEM}}$) is in the order of a second, long enough for a reliable recognition and an adequate reaction.

Response in case of sparks

The schematic proceeding for a detection of GEM discharges by the GVB is given in figure A.2. The GVB is able to distinguish between two different types of discharges:

- **Single GEM spark**
  The event of a "single GEM spark" is assumed as a minor severe event, the reactions are therefore restricted to the affected GEM channel only. In case of a discharge, the GEM-voltage drops significantly in the GVB (end of phase 1). Directly after the discharge, the GEM voltage is only about 100 V. This value is determined by the ratio of the resistors (protection resistors / resistors in the GVB-resistive chain). In case of a voltage drop of more than an given voltage a (default value $a = 100$V), the event is recognized as a GEM discharge and displayed on the front panel of the GVB. A warning message is sent to the
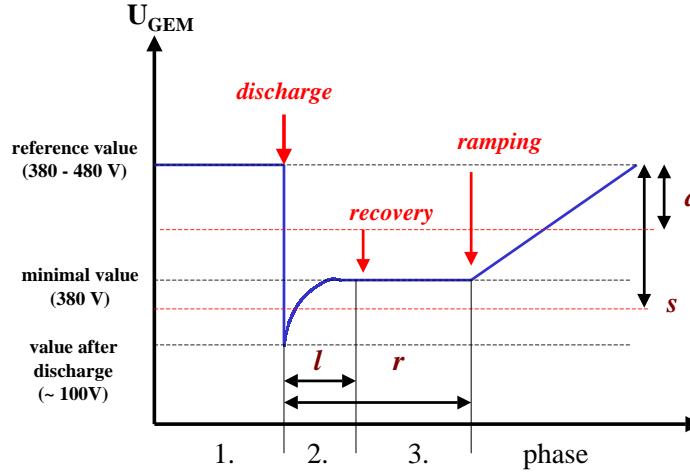
Figure A.2: Sketch of the GEM-spark recognition process. All parameters (a,s,l,r) can be individually adjusted during operation via terminal or CAN-bus.

slow control system via CAN-bus and in the same moment, the programmed reference GEM voltage is reduced to the minimal possible value (phase 2). This value is not zero, since the GEM-voltage is defined by the adjustable resistor in combination with the series resistor of $R = 6.8$ MΩ. In case of a single GEM spark, the real GEM voltage recharges to the minimal GEM voltage very quickly after the GEM-discharge. After a recovery time (phase 3) of r (default value $r = 10$ s), the voltage is slowly ramped up to the initial GEM voltage. Since GEM sparks cannot be completely excluded during operation and their effect is usually non-critical, all other channels (U_{GEM} for the remaining 7 channels as well as U_{drift} and U_{cath}) are kept at the nominal values, in order to provide a stable operation for the other detectors connected to this GVB.

- **Repetitive GEM sparks**
  The reaction to "repetitive sparks" has to be different, in order to prevent the GEM-device from major destructions. It was observed experimentally, that the GEM-spark probability in hadronic beams is significantly increased after a preceding GEM-discharge. The process of repetitive discharges may lead to GEM shorts and can usually only be stopped, if the GEM voltage is reduced to zero.

  The GVB has to reliably separate this event from ordinary single discharges. In contrast to single GEM sparks, the GEM voltage after the primary discharge does not reach the minimal GEM voltage (see phase 2). Due to ongoing discharges the ohmic resistor is bridged, and the GEM voltage remains low. If the GEM voltage — after a time of l seconds (default value $l = 1$s) — is lower than a given value s (default value $s = 300$V), all 8 channels of the affected GVB are immediately lowered to the minimal value and a hardwired alarm signal is sent directly to the current meters. These devices are equipped with high voltage relays. In case of emergency, the drift and the cathode voltage for all 8 detectors of this GVB are separated from the power supply. The operation is stopped and the MSGCs are in a safe state. The normal operation can only be restarted by

cancelling the alarm flag and by manually ramping up the detector voltages.

A.3   Experimental results

The reliability of the discharge recognition was optimized and tested in the lab. The experimental setup consisted of a prototype-GVB and a Hera-B full-size GEM-foil (glued to the frames and the drift electrode, but without MSGC). The most important potentials inside the GVB (GEM upper and lower potential and the DAC-value) were tapped and displayed by a digital oscilloscope. A schematic sketch of the system is given in figure A.3. Since
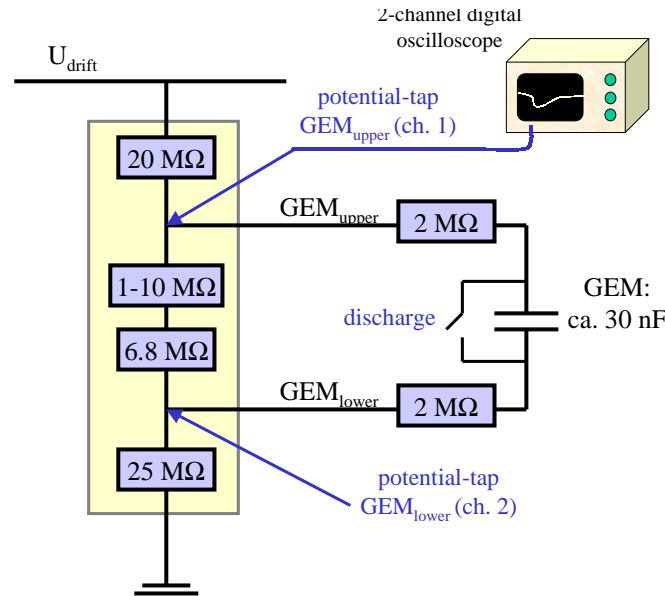
Figure A.3: The experimental setup. In some measurements, the real GEM was replaced by an equivalent capacitance of 30 nF. Here, discharges are simulated by a short-circuit spark. The upper and lower GEM potential and the DAC-value, reflecting the current value of the adjustable resistor, are monitored by a digital oscilloscope.

the GEM was extremely spark resistent, discharging could only be induced for GEM voltages larger than 520 V and in nitrogen with high humidity. A comparison of the discharges process detected by the GVB is given in figure A.4, one with deactivated and the other one with an active spark detection. Due to the resistive network in the GVB, the two potentials behave significantly different. The voltage drop seen for the upper GEM electrode is much smaller (80 V compared to 250 V see figure A.4, but since only the total voltage drop of both potentials is taken into account for the detection, this effect is minor important.

For some of the measurements, the original GEM-foil was replaced by an equivalent capacitance (see also figure A.3) in order to induce discharges at any GEM voltage. This procedure allowed for a test of the sensitiveness of the spark recognition in respect of the applied GEM voltage. In addition it was investigated with this setup, if single discharges can be effectively distinguished from repetitive discharges.
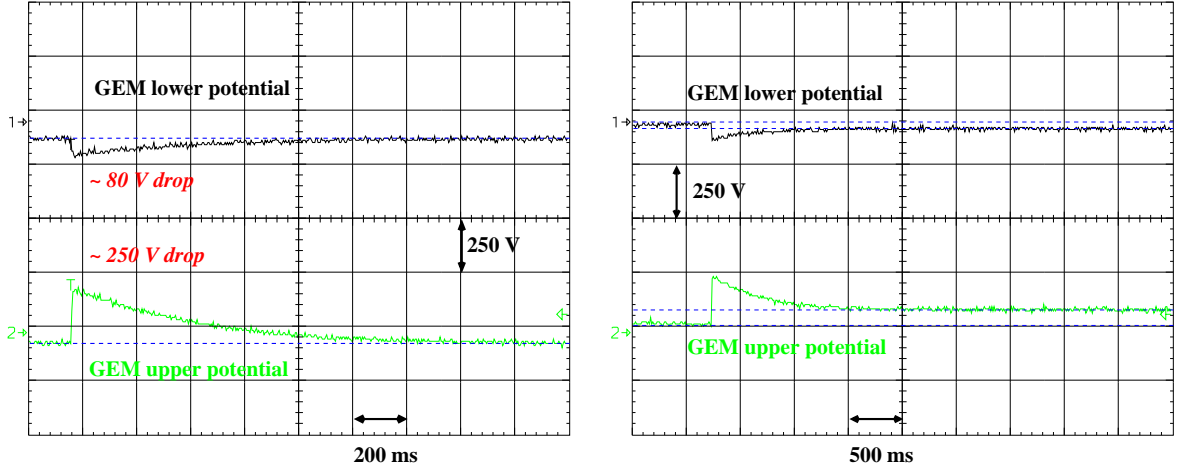
(a) Spark recognition deactivated, no active response, recharging of the GEM potentials to the nominal value

(b) Active response, the discharge process was successfully detected, recharging to the minimal GEM voltage

Figure A.4: Detection of GEM discharges by the controller of the GVB. The offset value from ground was corrected for this and all other oscilloscope shots.

Voltage overshoot

One reason for this extended study was the suspicion, that the real GEM voltage after the discharge might exceed the nominal GEM voltage during the recharging process. As a reaction to the breakdown of the GEM voltage, the DAC-value is set to the maximal possible value in order to reach the desired value. This procedure could result in significantly banked GEM voltage after the recharging.

However, it was demonstrated experimentally — by deactivating the spark detection — that the controlling mechanism is much to slow for this voltage overshoot in case of single discharges. The development in time of the GEM-upper potential and the DAC-value is shown in figure A.5, clearly proving, that the GEM voltage is slowly recharging without any overshoot. This result holds for low and high applied GEM voltages.

However, in case of repetitive sparks, an overshoot was indeed observed (see A.6), appearing as soon as the discharge process is quenched. The time interval is large enough for a significant change of the DAC-value, resulting in overvoltage at the GEM after the discharge process. This effect may induce new discharges. Please note, that the new active spark recognition can reliably detect sparks and prevent this phenomenon.

Sensitiveness

In the following figures, the GEM upper potential and the DAC-value (offset corrected) is depicted. In the graphs in figure A.7 it is demonstrated, that the recognition works reliably for high (490 V) as well as for low (380 V) U_{GEM}. The parameters in this test were set to $(a, r, l, s) = (100, 10, -300, 100)$ for both measurements.

(a) Test for high GEM-gain ($U_{GEM} = 490$ V)   (b) Test for low GEM-gain ($U_{GEM} = 380$ V)
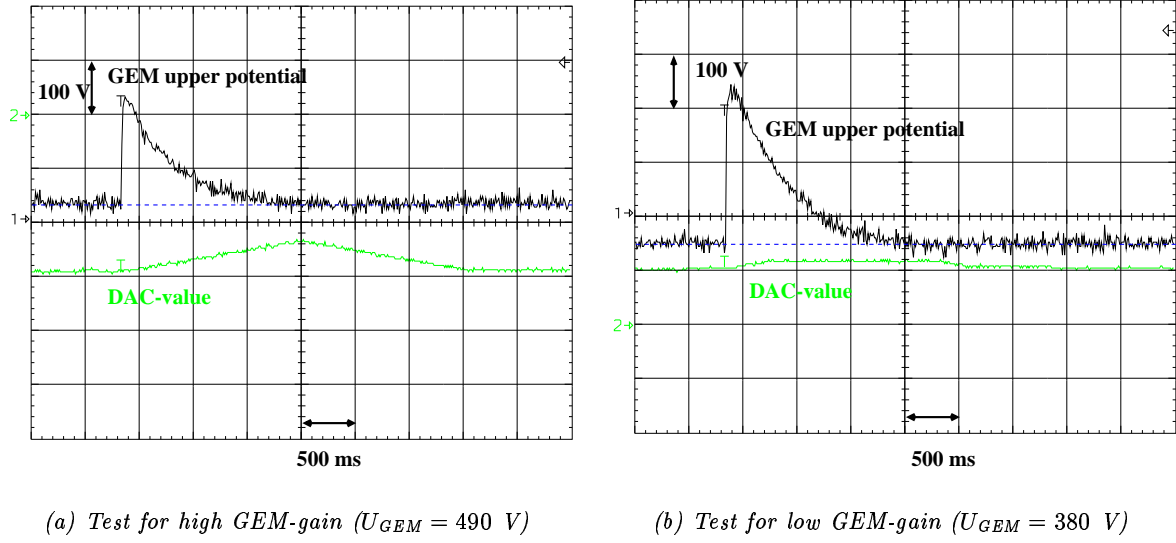
Figure A.5: For a single GEM discharge, no voltage overshoot was observed. After recharging, the GEM upper potentials approaches the nominal value.

(a) Repetitive discharging for 1.2 s, resulting in an overshoot of 10 V for the GEM upper potential   (b) Repetitive discharging for 5 s, resulting in an overshoot of 40 V for the GEM upper potential
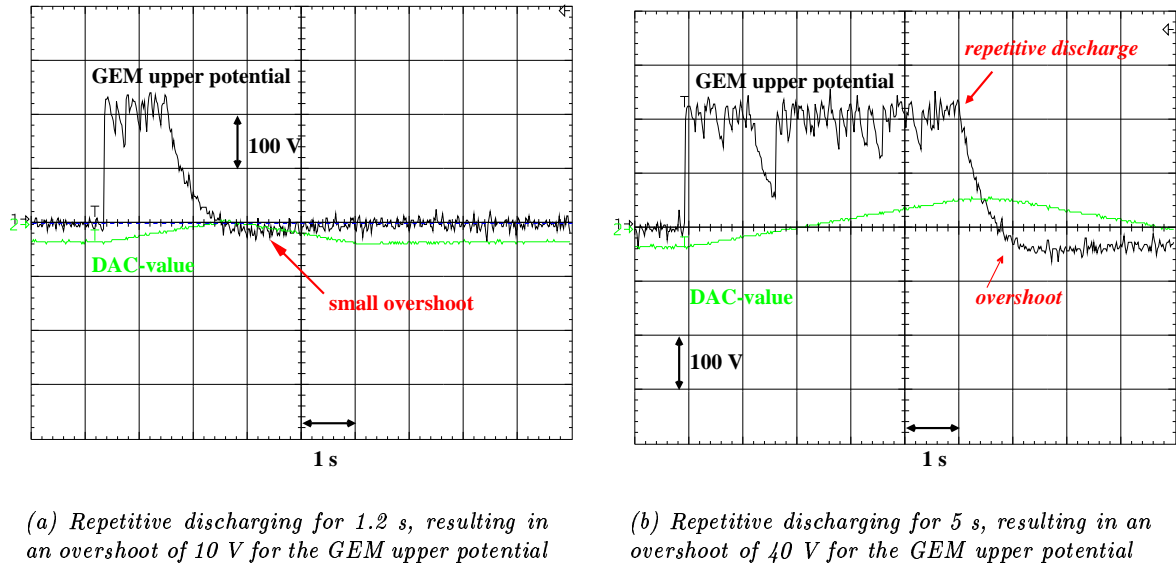
Figure A.6: Voltage overshoot for repetitive discharges. The DAC-value increases and after recharging U_{GEM} is found to be over the nominal value. Please note, that the spark detection was not activated here.

Reaction time

The reaction time of the GVB is given by the processing time for one loop in the discharge recognition program of the internal controller. As depicted in figure A.8, the reaction time was measured to be approximately 130 ms. This value is much faster compared to any control mechanism of the slow control system.

(a) Example for high GEM voltage ($U_{GEM} = 490\,V$)

(b) Example for low GEM voltage ($U_{GEM} = 380\,V$)
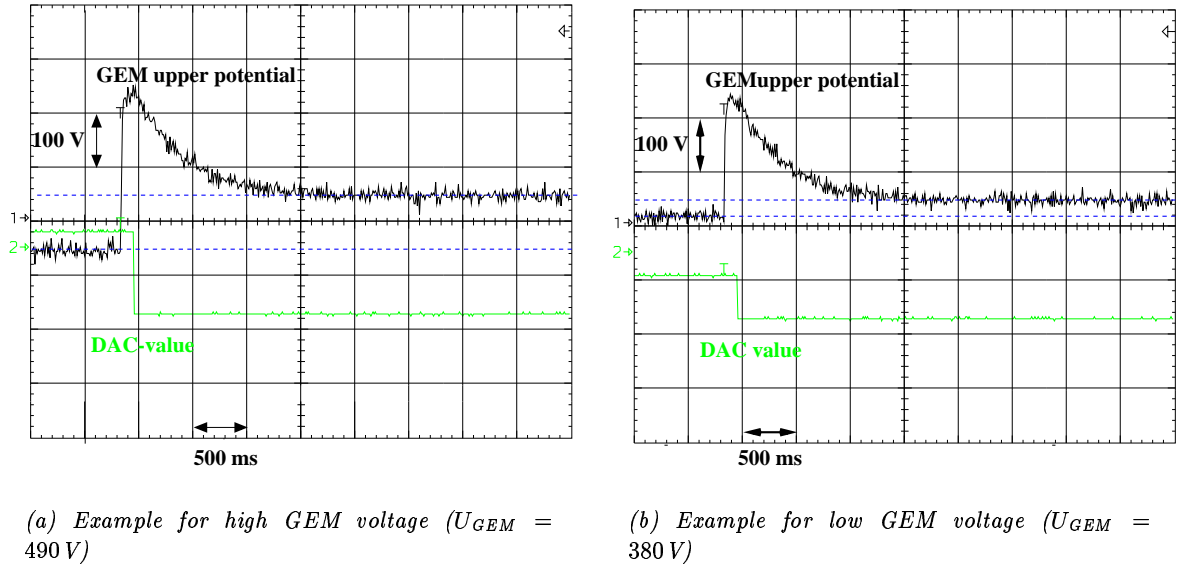
Figure A.7: Reliable detection of single GEM discharges at any applied GEM voltage
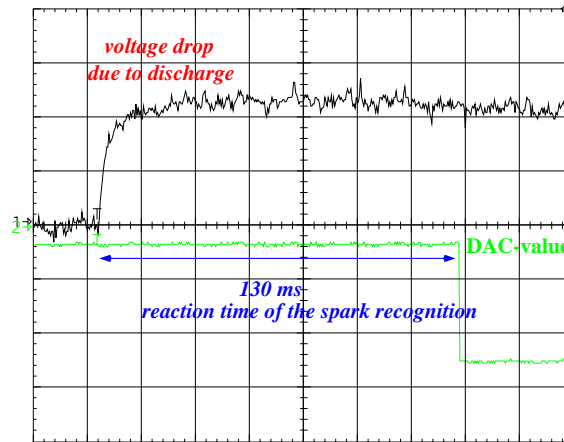
Figure A.8: The typical reaction time of the GVB to detect GEM discharges is roughly 130 ms

Optimization of the parameters for the Hera-B operation

All software parameters of the spark detection were optimized for the operation at the Hera-B beam, as described below:

- a

  The parameter a (="minimal voltage drop for a GEM discharge recognition") was varied between 20 and 300 V, without any detectable effect. All "real" discharges were detected and no "fake trigger" was observed. It is very unlikely, that the variation due to beam intensity fluctuations cause voltage drops of more than a few volts.

- s, l

  The parameter l defines the time interval (after the discharge) after which a discharge will be detected as a "repetitive discharge". The GEM voltage has to be below a given threshold value s for the hole period. A typical time intervall of 1 seconds was derived from the recharging time. For this period and the default threshold value of $s = 300V$, the separation between single and repetitive discharges was fully efficient.

- r

  The recovery time r before re-ramping the GEM voltage must be adjusted during operation at the Hera-B experiment. The default value (10s) is a conservative approximation of the GEM recovery time in hadronic beams.

Bibliography

[1] H. Geiger, W. Müller, Phys. Zeits. 29 (1928) 839.

[2] G. Charpack et al., Nucl. Instr. and Methods 62 (1968) 262.

[3] A.H. Walenta, Dissertation, Univ. of Heidelberg, Germany (1972)

[4] F. Sauli, *Gas detectors: Achievments and Trends*, inv. talk at the 8th Pisa Meeting on Advanced Detectors, Isola d'Elba, Italy, 21-27 May 2000.

[5] Anton Oed, Nucl. Instr. and Meth.A263 (1988) 351.

[6] F. Sauli, Principles of operation of multiwire proportional and drift chambers, CERN 77-09.

[7] F.Sauli et al. Development of MSGC for radiation detection and tracking at high rates - final status report (LDRB Status Report/RD-28) CERN/LHCC 96-18 (1996).

[8] T. Hott, Inaugural-Dissertation, Univ. of Heidelberg, Physics Dep., Germany (1997).

[9] Y. Giomataris et al. Nucl. Inst. and Meth. A376 (1996) 29-35.

[10] Y. Benhammou et al. Proceedings of the Micro-Pattern-Gas-Detector Conference, Paris-Orsay, June 28-30, 1999.

[11] B. Adeva et al., hep-ex/9902017 v3 30-04-99, to be published in NIM.

[12] Kapton, Du Pont Co., Wilmington DE, USA.

[13] R. Bellazzini et al., Nucl. Inst. and Meth. A424 (1998) 444-458.

[14] R. Bellazzini et al., Nucl. Inst. and Meth. A423 (1999) 125-134.

[15] R. Bellazzini et al., Nucl. Inst. and Meth. A425 (1999) 218-227.

[16] M. Walter, diploma thesis, Univ. of Heidelberg, Physics Dep., Germany (2000).

[17] C. Richter, F. Schwab, *Simulationen zu Feldern und Signalentstehung in MSGCs und MGD,* internal note, ITR, Univ. of Heidelberg, Germany.

[18] F. Sauli, Nucl. Instr. and Meth. A386 (1997) 531.

[19] R.Bouclier et al., IEEE Trans. Nucl. Sci.44(3)(1997)464-450.

[20] R.Bouclier et al., Nucl. Instrum. and Meth. A396 (1997) 50.

[21] C. Büttner et al., Nucl. Instr. and Meth. A409 (1998) 79.

[22] J. Bennloch et al., Nucl. Instr. and Meth. A419 (1998) 410.

[23] S. Bachmann et al., *A GEM detector for the COMPASS experiment*, Proc. of the Int. Workshop on Micropattern Gas Detectors, Orsay, France, June 28-30 (1999)

[24] B.Bochin et al., *X-ray tests of double and triple GEM detectors LHCb* 98-068 TRAC.

[25] M. Ziegler et al., LHCb internal note, LHCb 2000-56, June 29, 2000.

[26] M.S.Dixit et al., *TPC Readout using the GEM*, published in the Proc. of the Int. Workshop on Micropattern Gas Detectors, Orsay, France, June 28-30 (1999).

[27] M. Hoch et al., *Gas Electron Multiplier as readout for the Alice TCP*, published in the Proc. of the Int. Workshop on Micropattern Gas Detectors, Orsay, France, June 28-30 (1999).

[28] A.Pansky et al., Nucl. Instr. and Meth. A 323 (1992) 294.

[29] A. Breskin et al., Radiat. Protect. Dosim. 61 (1995) 1272.

[30] U. Werthenbach, Universität-Gesamthochschule Siegen, Germany, *private communications.*

[31] CERN Surface Treatment Workshop, EST/SM/CI, CH-1211 Genf 23.

[32] P. Cwetanski, *Studies on detector prototypes for the inner tracking system of LHCb*, diploma thesis, Univ. of Heidelberg, Physics Dep., Germany (2000) and references therein.

[33] M. Hildebrand, Inaugural-Dissertation, Univ. of Heidelberg, Physics Dep. Germany (1999).

[34] C. Richter et al., *On the efficient electron transfer through GEM* submitted to Nucl. Instr. and Meth. A. (2000).

[35] C. Richter et al., *Absolute Single Electron Transfer through GEM* to be published in the Preceedings of the 8th Pisa Meeting in Nucl. Instr. and Meth. A.

[36] A. Breskin, Nucl. Instr. and Meth. A367 (1995) 326 and references therein.

[37] R. Chechik et al., Advances in single-electron detectors and their applications. Proc. of the IEEE 1999 Nucl. Sci. Symposium; in press, and references therein.

[38] A. Breskin et al., Nucl. Instr. and Meth. A442 (2000) 58 and references therein.

[39] A. Buzulutskov et al., Nucl. Instr. and Meth. A443 (2000) 164.

[40] S. Bachmann et al., Nucl. Instr. and Meth. A439 (1999) 376 and references therein.

[41] A. Dimauro et al., Nucl. Instr. and Meth. A371 (1996) 137 and references therein.

[42] A. Sharma, *Detection of single electrons emitted from a photocathode with the GEM*. CERN-OPEN-99/372, submitted to Nucl. Instr. and Meth. A.

[43] F. Sauli, Ann. Rev. Nucl. Part. Sci 49 (1999) 341.

[44] G. Garty et al., Nucl. Instr. and Meth. A433 (1999) 476.

[45] MAXWELL Commercial Finite Element Computation Package, Ansoft Co. Pittsburg, PA, USA.

[46] A. Sharma, Dept. of Physics, Univ. of Maryland, USA, *private communications*.

[47] A. Sharma, 3D Simulation of the GEM; CERN-OPEN-99/373, to be published in Nucl. Instr. and Meth. A.

[48] S.F. Biagi, Nucl. Instr. and Meth A 283 (1989) 716.

[49] R. Veenhof, GARFIELD, Version 6.33, Nov. 1999., Nucl. Instr. and Meth A 419 (1998) 726.

[50] O. Frisch, Brit. Atom. Energy Report, BR-49 (1944)

[51] D. Mörmann, Rad. Det. Lab., Physics Department, Weizmann Institute of Science, Israel, *private communications*.

[52] S.Bachmann et al., Nucl. Inst. and Meth. A438 (1999) 376.

[53] J.Va'vra, Nucl. Instr. and Meth. A371 (1996) 33 and references therein.

[54] R. Chechik et al., Nucl. Instr. and Meth. A419 (1998) 423.

[55] S.A. Korff, *Electrons and nuclear counter* Van Nostrand, New York 1946.

[56] A.Breskin, R. Chechik and N. Zwang, *Properties of very low pressure multiwire proportional chambers*, IEEE trans Nucl Science Vol NS-27, (1980) 133.

[57] Hera-B Design Report, DESY-PRC 95/01,1995.

[58] D. Ressing, Nucl. Inst. and Meth. A384 (1996) 131.

[59] H.B.Dreis et al., Development of a Scintillating Fibre Detector for Hera-B, DESY 98-049, april 1998.

[60] W. Gradl, Univ. of Heidelberg, Physics Dep., Germany, *private communications*.

[61] Fraunhofer Institut für Schicht und Oberflächentechnik IST, D-38108 Braunschweig, Germany.

[62] IMT Masken und Teilungen AG, CH-8606 Greifensee, Switzerland.

[63] G10, Fibrolux GmbH, D-65719 Hofheim-Wallau, Germany.

[64] W. Fallot-Burghart et al., Helix128-x User Manual, ASIC-Labor, University of Heidelberg
(http://wwwasic.ihep.uni-heidelberg.de/feuersta/projects/Helix/helix/helix.html).

[65] A339, 8-channel high-voltage current meter, designed and manufactured by the electronic workshop of the Physikalisches Institut of the University of Heidelberg, Germany (1998)
(http://www.physi.uni-heidelberg.de/~vwalter/Geraete/A339_Current_Meter)

[66] S. Hausmann, Inaugural-Dissertation, Univ. of Heidelberg, Physics Dep., Germany (1999).

[67] A344, GEM-Voltage-Box, designed and manufactured by the electronic workshop of the Physikalisches Institut of the University of Heidelberg, Germany (1998).
(http://www.physi.uni-heidelberg.de/~vwalter/Geraete/A344_GEM-Verteiler)

[68] H. Raether, *Electron Avalanches and Breakdown in Gases*, Butterworths, London, GB (1964).

[69] C. Richter et al. *Discharges in Micro Strip Gas Chambers Part I: Induced Discharges in Hadronic Beams*, submitted to Nucl. Inst. and Meth. A.

[70] B. Schmidt et al., *MSGC Development for HERA-B*, physics/9804035, Proc. 36th Workshop of the Eloisatron Project of New Detectors, Erice, Italy (1997) 270–287.

[71] S. Visbeck, Diploma Thesis, Univ. of Heidelberg, Physics Dep., Germany (1996).

[72] C. Bresch, Diploma Thesis, Univ. of Heidelberg, Physics Dep., Germany (1997).

[73] Program Package ACE, courtesy of the ABB corporation.

[74] S. Keller et al., Nucl. Inst. and Meth. A419 (1998) 382.

[75] C. Richter et al., *Sparks in Microstrip Gas Chambers Part II: Sparks in GEM - MSGC*, in preparation.

[76] R. Bouclier et al., Nucl. Inst. and Meth. A346 (1994) 114.

[77] R. Bouclier et al. Proc. Int. Conf. on MSGCs (Legarno, 1994).

[78] M. Salomon et al., TRI-PP 94-24 (1994).

[79] R. Bouclier et al., CERN-PPE/95-37 and references therein.

[80] P. Robmann, Institut für Physik, Zürich, Switzerland, *private communications*.

[81] H. B. Dreis, *The Hera-B Inner Tracking Gas System*, Proceedings of the Micro-Pattern-Gas-Detector Conference, Paris-Orsay, June 28-30, 1999

[82] Stycast 1266, Grace Specialty Polymers (D: Emerson & Cuming Specialty Polymers, D-63477 Maintal)

[83] EPO-TEK H72, Polytec GmbH, D-76337 Waldbronn, Germany.

[84] Eccobond 285, Grace Specialty Polymers (D: Emerson & Cuming Specialty Polymers, D-63477 Maintal)

[85] TorrSeal, Varian Vacuum Products, 121 Hartwell, Lexington, MA 02173, USA.

[86] SURMET Corporation, 33 B Street, Burlington, MA 01803, USA.

[87] F. Sauli, *Applications of gas detectors in astrophysics, medicine and biology*, Nucl.
      Inst. and Meth. A323 (1992)1.

List of Figures

Acknowledgments

Ich möchte mich bedanken bei / I wish to thank / Vorrei ringraziare / תודה רבה ...